L

LAND SURFACE EMISSIVITY

Alan Gillespie
Department of Earth and Space Sciences, University of Washington, Seattle, WA, USA

Definitions

Land surface emissivity (LSE). Average emissivity of an element of the surface of the Earth calculated from measured radiance and land surface temperature (LST) (for a complete definition, see Norman and Becker, 1995).

Atmospheric window. A spectral wavelength region in which the atmosphere is nearly transparent, separated by wavelengths at which atmospheric gases absorb radiation. The three pertinent regions are "visible/near-infrared" (∼0.4–2.5 μm), mid-wave infrared (∼3–5 μm) and long-wave infrared (∼8–14 μm).

Blackbody. An ideal material absorbing all incident energy or emitting all thermal energy possible. A cavity with a pinhole aperture approximates a blackbody.

Brightness temperature. The temperature of a blackbody that would give the radiance measured for a surface.

Color temperature. Temperature satisfying Planck's law for spectral radiances measured at two different wavelengths.

Contrast stretch. Mathematical transform that adjusts the way in which acquired radiance data translate to the black/white dynamic range of the display monitor.

Emissivity ε. The efficiency with which a surface radiates its thermal energy.

Irradiance. The power incident on a unit area, integrated over all directions (W m^{-2}).

Graybody. A material having constant but non-unity emissivity.

Long-wave infrared (LWIR). For most terrestrial surfaces (∼340 K to ∼240 K), peak thermal emittance occurs in the LWIR (∼8–14 μm).

Mid-infrared (*MIR*). Forest fires (∼1,000–600 K) have peak thermal emittances in the MIR (∼3–5 μm).

Noise equivalent Δ *temperature (NE*ΔT*)*. Random measurement error in radiance propagated through Planck's law to give the equivalent uncertainty in temperature.

Path radiance $S_{\uparrow}$. The power per unit area incident on a detector and emitted upward from within the atmosphere (W m^{-2} sr^{-1}).

Planck's law. A mathematical expression relating spectral radiance emitted from an ideal surface to its temperature (Equation 1, in the entry *Land Surface Temperature*).

Radiance. The power per unit area from a surface directed toward a sensor, in units of W m^{-2} sr^{-1}.

Reflectivity ρ. The efficiency with which a surface reflects energy incident on it.

Reststrahlen bands. Spectral bands in which there is a broad minimum of emissivity associated in silica minerals with interatomic stretching vibrations of Si and O bound in the crystal lattice.

SEBASS. Spatially Enhanced Broadband Array Spectrograph System, a hyperspectral TIR imager (Hackwell et al., 1996).

Short-wave infrared (SWIR). Erupting basaltic lavas (∼1,400 K) have their maximum thermal emittance at ∼2.1 μm in an atmospheric window at 0.4–2.5 μm. Part of this spectral region (1.4–2.5 μm) is called the SWIR.

Sky irradiance $I_{\downarrow}$. The irradiance on the Earth's surface originating as thermal energy radiated downward by the atmosphere (W m^{-2}) (spectral irradiance: W m^{-2} μm^{-1}).

Spectral radiance L. Radiance per wavelength, in units of W m^{-2} μm^{-1} sr^{-1}.

Thermal infrared (TIR). Thermal energy is radiated from a body at frequencies or wavelengths in proportion to its temperature. The wavelengths for which this radiant energy

E.G. Njoku (ed.), *Encyclopedia of Remote Sensing*, DOI 10.1007/978-0-387-36699-9,

is significant for most terrestrial surfaces (~1.4–14 μm) are longer than the wavelength of visible red light and hence are known as thermal infrared. The TIR is subdivided into three ranges (LWIR, MIR, SWIR) for which the atmosphere is transparent (atmospheric "windows") so that the energy can be measured from space.

Introduction

Thermal emissivity ε is the efficiency with which a surface emits its stored heat as thermal infrared (TIR) radiation. It is useful to know because it indicates the composition of the radiating surface and because it is necessary as a control in atmospheric and energy-balance models, since it must be known along with brightness temperature to establish the heat content of the surface. The first practical demonstration of multispectral TIR imaging for compositional mapping was from a NASA airborne scanner flown over Utah (Kahle and Rowan, 1980).

Emissivity differs from wavelength to wavelength, just as reflectivity ρ does in the spectral region of reflected sunlight (0.4–2.5 μm). Emissivity is defined as

$$\varepsilon(\lambda) = \frac{L(\lambda, T)}{B(\lambda, T)} \quad (1)$$

where L is the measured spectral radiance and B is the theoretical blackbody spectral radiance for a surface with a skin temperature T. B is given by Planck's law which, together with the basic physics of TIR radiative transfer, is discussed in the entry *Land Surface Temperature* (LST).

Unlike T, which is a variable property of a surface controlled by the heating history and not directly by composition, $\varepsilon(\lambda)$ is independent of T and is a function directly of composition. Furthermore, $\varepsilon(\lambda)$ in the TIR wavelengths (3–14 μm) responds to different aspects of composition than reflectivity $\rho(\lambda)$ at 0.4–2.5 μm. In general, ρ at wavelengths 0.4–2.5 μm is controlled by the amounts of iron oxides, chlorophyll, and water on the surface; ε in the TIR is controlled more by the bond length of Si and O in silicate minerals. Examples of emissivity spectra are given in Figure 1.

TIR spectroscopy is especially important because silicate minerals are the building blocks of the geologic surface of Earth, and their presence and amounts can be inferred only indirectly at shorter wavelengths. Thus TIR spectroscopy is complementary to spectroscopy of reflected sunlight. Good summaries of TIR spectroscopy and its significance in terms of surface composition may be found in Lyon (1965), Hunt (1980), and Salisbury and D'Aria (1992). A good introduction to spectral analysis may be found in Clark et al. (2003).

Figure 1 shows daytime and nighttime false-color composite images of spectral radiance from a sparsely vegetated part of Death Valley, California, enhanced using a decorrelation contrast stretch (Soha and Schwartz, 1978; Gillespie et al., 1986). This stretch emphasizes the emissivity component of the signal, shown as color, and de-emphasizes the temperature, shown as dark/light intensity. In addition to composition, the daytime image gives a good sense of topography, because sunlit slopes are warmer than shadowed slopes. In the nighttime image, most temperature effects are subdued, and the image closely resembles the Land Surface Emissivity (LSE) alone.

Exceptions include standing water, which is cooler than the land during the day but warmer at night. Standing water (C) in the floor of Death Valley shows dark green in the daytime image but light pink in the nighttime image. Vegetation (A) appears dark in the daytime image, when it is cooling its canopy by evapotranspiration. The toe of an alluvial fan (B) appears darker at night, when soil moisture rises to the surface and evaporates.

The colors in Figure 1 indicate rock type. For example, the emissivity of quartzite is low (~0.8) at 8.3 and 9.1 μm (blue and green) but high at 10.4 μm (red); therefore, it is displayed as red. Other rock types and display colors can be understood by comparing the images and emissivity spectra in Figure 1.

The discussion below focuses on algorithms designed to recover emissivities from remotely sensed spectral radiance data. Figure 2, of a desert landscape, compares spectral radiance to temperature and emissivity images recovered from it. Also shown are emissivity spectra of vegetation and the geologic substrate. As explained in the entry *Land Surface Temperature*, temperature and emissivity recovery is an underdetermined problem, and dozens of approaches have been proposed and published that break down the indeterminacy. These fall in four classes: deterministic algorithms that solve for *LST* and *LSE* exactly, algorithms that recover the shape of the LSE spectrum only, model approaches that make key assumptions, and algorithms that attempt also to scale or calibrate the normalized spectra to their actual emissivity values.

In evaluating the algorithms, it is useful to ask how accurately it is necessary to recover LSE and LST. For example, many analytic algorithms that seek to identify surface composition rely not so much on actual emissivity values, but on the central wavelengths of emissivity minima (e.g., reststrahlen bands), which can be diagnostic for many rocks and minerals. If this is your goal, it may not be necessary to scale the spectra, relying instead on the simpler algorithms that just recover spectral shape.

Errors in LST may affect some algorithms by warping the spectra over several μm of wavelength. This happens because the shape of the Planck function changes with temperature (*Land Surface Temperature*, Figure 2). A 5 K error at 300 K, for example, will cause a slope in the recovered emissivity spectrum of 0.05 from 8 to 14 μm. However, the sharp mineralogical features (~0.2–0.5 μm wide) are readily distinguished against this distorted continuum.

The TIR is commonly a difficult spectral region in which to measure spectral radiance, and the images are typified by a low signal–noise ratio. This ratio is commonly represented by the "noise equivalent Δ temperature" or

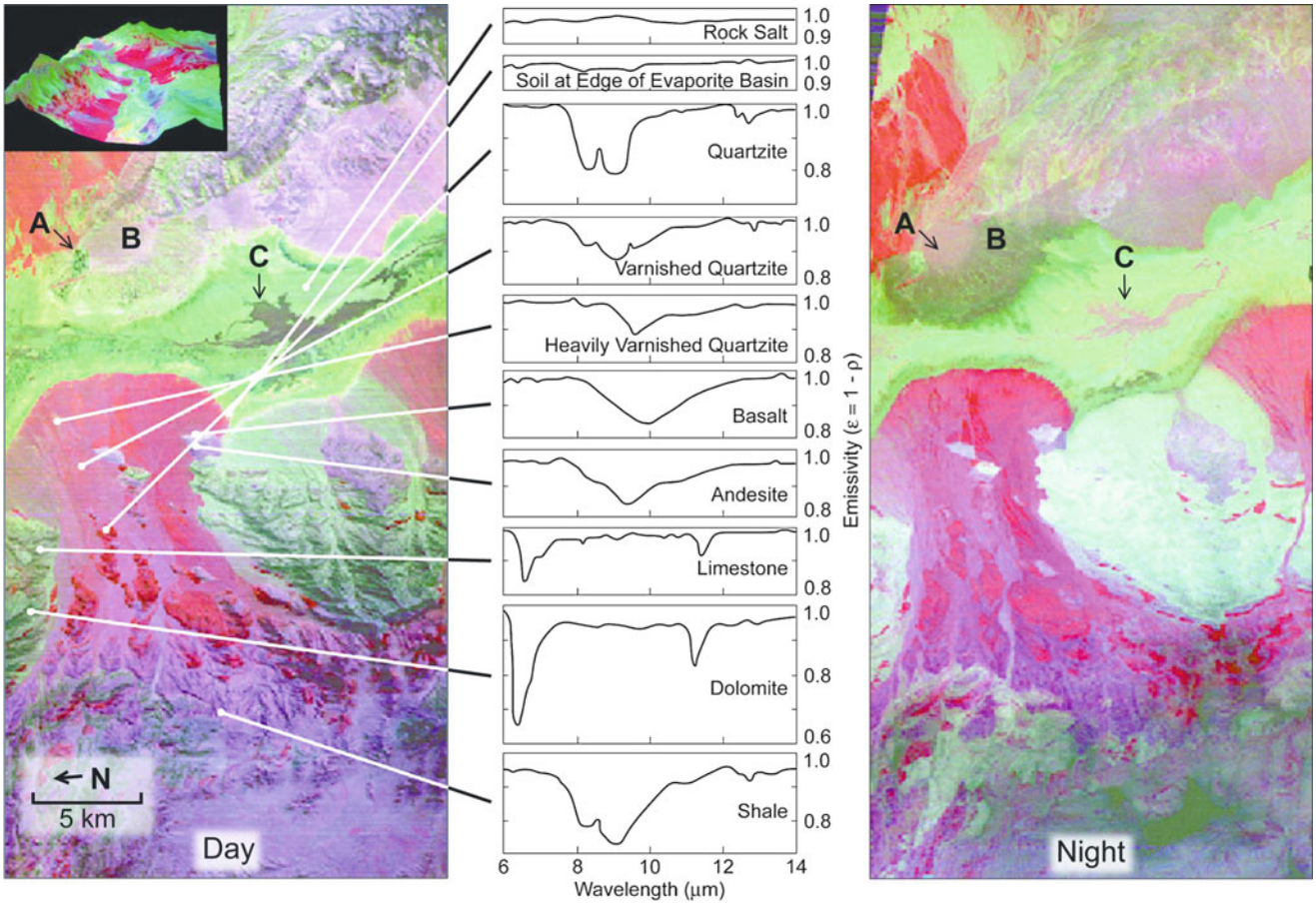

Land Surface Emissivity, Figure 1 Airborne thermal infrared multispectral scanner (TIMS: Palluconi and Meeks, 1985) false-color TIR radiance images of Death Valley, California (RGB = 10.4, 9.1, 8.3 μm). Letters *A*, *B*, and *C* indicate sites discussed in the text. *Central column* shows laboratory spectra for field samples. *Inset* shows similar ASTER image "draped" over topography, looking north up Death Valley. The TIMS images cross the central part of the ASTER footprint (Courtesy Harold Lang and Anne Kahle, JPL).

NEΔT, which is the temperature difference corresponding to the standard deviation of the radiance within a homogeneous, isothermal scene region. For TIR imagers such as ASTER, $NE\Delta T_{300K} \approx 0.25$ K. Also for ASTER, the NEΔT, atmospheric correction, and radiometric calibration all introduce errors of about the same size, leading to a total uncertainty in the recovered LST of about 1.5 K and in the LSE of ~0.015.

Deterministic solutions for emissivity

As discussed in *Land Surface Temperature*, recovering both LST and LSE from a single image is underdetermined. In principle, this problem can be removed by increasing the number of images acquired for the same scene. For each n-channel image, after atmospheric compensation, there are $n + 1$ unknowns, but only n measurements; for two images of the same scene, there are $n + 2$ unknowns, but $2n$ measurements (assuming LST has changed but LSE has remained constant). Therefore, a two-channel image taken at two different times is deterministic. It is additionally necessary that the LST be significantly different between acquisitions.

Two-time, two-channel approach

If well-registered multispectral day–night radiance measurements are available, it is possible to determine T and ε uniquely (Watson, 1992a). Although this approach is esthetic, for most TIR data, the recovered temperatures and emissivities tend to be imprecise. For example, for image channels at 8 and 12 μm, day–night temperatures of 290 and 310 K, and for $NE\Delta T = 0.3$ K, recovered LST would have an uncertainty of ≥20 K. This arises because of the flat shape of the Planck curve in the spectral range around 300 K.

Wan (1999) showed that using an image channel in the 3–5 μm window, where the slope of the Planck function is steep, can improve the precision greatly and used the day–night algorithm to make a standard MODIS LST product. However, for daytime data, reflected sunlight at 3–5 μm must be accounted for (see *Land Surface Temperature*, Figure 3). Furthermore, acquiring data 12 h or more apart

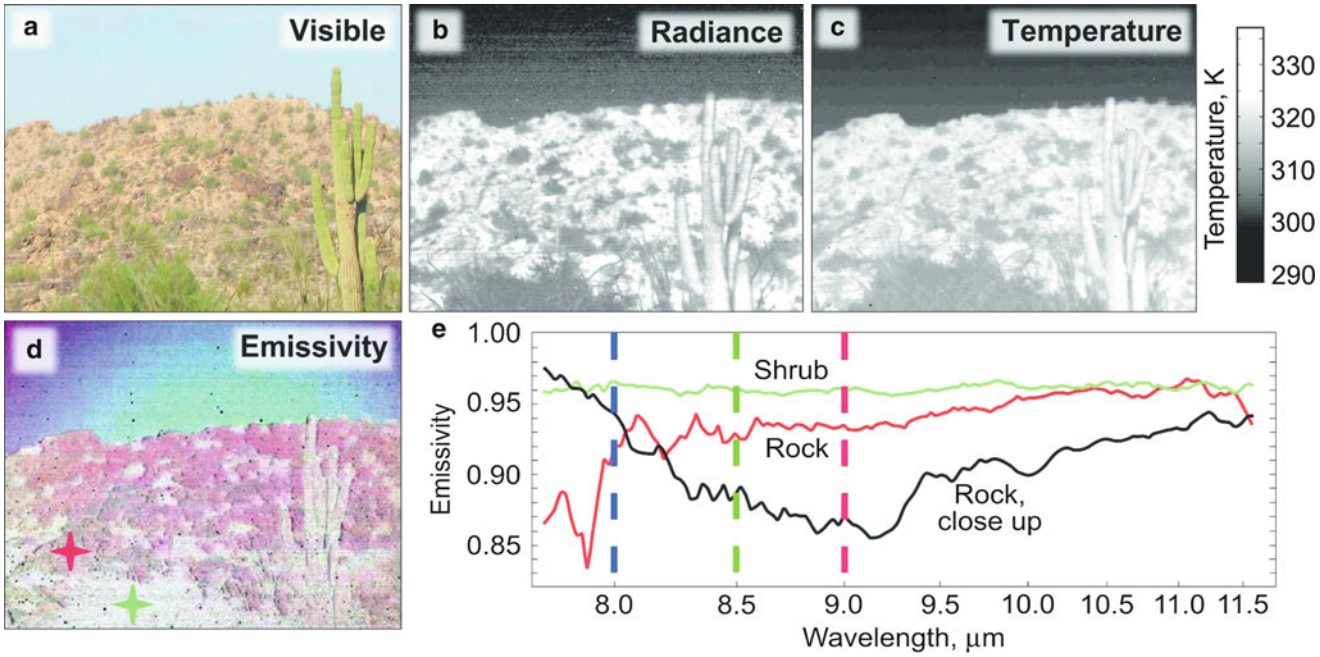

Land Surface Emissivity, Figure 2 TIR images and spectra, South Mountain, Arizona, looking SE. (**a**) Natural color; (**b**) TIR radiance at 9 μm; (**c**) brightness temperature; (**d**) emissivity (RGB = 8, 8.5 and 9 μm, respectively); (**e**) emissivity spectra measured with the TELOPS, Inc., FIRST hyperspectral imaging spectrometer, August 8, 2007. The shrub spectrum was taken from the site in d marked the *green cross*; the rock spectrum from the *red cross*. Differences in the "rock" spectra likely relate to differences in the pixel field of view and exact location, and in the length of the atmospheric path between the sample and sensor.

adds complexity because the scene may have changed between images, for example, because of dew.

It is also advantageous to use more than two channels, in which case the inversion for LST and LSE is overdetermined. This has the advantage of reducing the impact of measurement errors. The exaggeration of measurement error in this otherwise esthetic technique will become less severe as high-precision imagers such as SEBASS ($NE\Delta T_{300K,\ 11\mu m} < 0.05$ K: Hackwell et al., 1996) become widely available.

Emissivity bounds method

Jaggi et al. (1992) observed that for every pixel and every channel i there exists a locus of (T, ε_i) vectors that are possible solutions for the modified Planck equation (Equation 1, *Land Surface Temperature*). Because T must be the same for all image channels, some (T, ε_i) pairs can be ruled out as candidate solutions. The range of solutions is even more limited if ε and/or T can be restricted a priori. For the land surface, it is commonly possible to assume that $0.8 < \varepsilon < 1.0$, for example.

This elegant approach is not truly deterministic, because it requires assumed limits to ε and/or T. However, it requires no empirical assumptions. The technique does not appear to have been widely used, perhaps because it does not identify the most probable values of ε or T, only possible ranges. In practice, performance depends on how well emissivity limits are known a priori, and implementation would probably require some sort of image classification to establish them closely.

Spectral-shape solutions

Although it is not possible to invert the modified Planck equation for both ε and T without external constraints, it is possible to estimate spectral shape for ε, at the expense of T and of the amplitude of the recovered spectrum, that is, the recovered spectra are essentially normalized, so that only relative amplitudes (wavelength to wavelength) are known. This is nevertheless useful, since composition is generally determined from spectral shape, and not the absolute amplitudes.

Ratio methods

Watson (1992b) observed that ratios of spectrally adjacent channels i and j described spectral shape accurately, provided that T could be estimated even roughly:

$$\frac{\varepsilon_j}{\varepsilon_i} = \frac{L_j\lambda_i^5\left(\exp\left(c_2/(\lambda_i T)\right) - 1\right)}{L_i\lambda_j^5\left(\exp\left(c_2/(\lambda_j T)\right) - 1\right)} \tag{2}$$

(c_2 is a constant from Planck's law, Equation 1, *Land Surface Temperature*). To calculate the ε ratios, it is necessary first to approximate the temperature T from the measured radiances L_i and L_j. If ε can be estimated

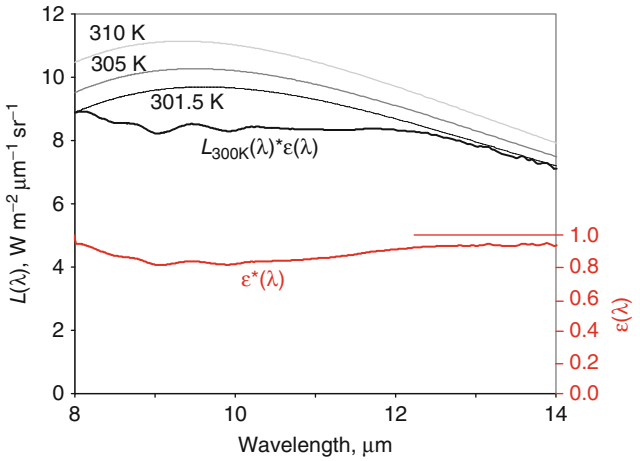

Land Surface Emissivity, Figure 3 Emissivity $\varepsilon(\lambda)$ and spectral radiance spectra $L(\lambda)$ for basalt at 300 K. $L(\lambda)$ was calculated as the product of measured $\varepsilon(\lambda)$ and a 300 K blackbody ($B(\lambda)$) spectrum. In "Planck draping," blackbody spectra are calculated for successively lower temperatures (e.g., 310, 305 and 301.5 K, above) until $\varepsilon_{max}\, B(\lambda) = L(\lambda)$ at some wavelength. The maximum emissivity, ε_{max} must be estimated, usually as a value near 0.95 as in the example shown. $\varepsilon^*(\lambda)$, the recovered $\varepsilon(\lambda)$, is calculated as $L(\lambda)/B(\lambda)$. Both it and the found LST (301.5 K, above) will be inaccurate unless the Planck functions are scaled correctly by ε_{max}. In the example shown, LST is in error by 1.5 K. The error warps $\varepsilon^*(\lambda)$ slightly.

within ±0.075, the uncertainty in T is ±5 K, and the ε ratios can be estimated with an average error of ~0.007 (this estimate does not include the effects of measurement error).

Becker and Li (1990) proposed a similar approach they called the "temperature-independent spectral indices" (TISI) method. TISI begins with the observation (Slater, 1980) that Planck's law may be represented by

$$B_k(T_s) = \alpha_k(T_o)T^{n_k(T_o)} \tag{3}$$

where B is the spectral radiance in image channel k for a blackbody at temperature T_s and T_o is a reference temperature. Constants n_k and α_k are given by

$$\begin{aligned} n_k(T_o) &= \frac{c_2}{\lambda_k T_o}\left(1 + \frac{1}{\exp\left(c_2/\lambda_k T_o\right) - 1}\right); \\ \alpha_k(T_o) &= \frac{B_k(T_o)}{T_o^{n_k(T_o)}} \end{aligned} \tag{4}$$

(Dash, 2005). The land-leaving spectral radiance L_k, corrected for atmospheric absorption and path radiance but not down-welling spectral irradiance $L_k^{\downarrow}$, is thus

$$L_k = \varepsilon_k \alpha_k T_s^{n_k} C_k; \quad C_k = 1 + \frac{(1-\varepsilon_k)L_k^{\downarrow}}{\varepsilon_k B_k(T_s)} \tag{5}$$

where C_k is spatially variable and atmosphere specific. The TISI is found by rationing spectral radiances for image channels i and j:

$$\frac{L_i^{a_i}}{L_j^{a_j}} = \frac{\varepsilon_i^{a_i}\alpha_i^{a_i}T_s^{n_i a_i}C_i^{a_i}}{\varepsilon_j^{a_j}\alpha_j^{a_j}T_s^{n_j a_j}C_j^{a_j}} \tag{6}$$

Here a_i is defined as n_i^{-1} (and $a_j = n_j^{-1}$), chosen to make Equation 6 independent of T. Since for a wide range of temperatures the C ratio is close to unity, TISI is then

$$TISI_{i,j} = \left[\frac{L_i}{\alpha_i}\right]^{1/n_i}\left[\frac{L_j}{\alpha_j}\right]^{-1/n_j} = \frac{\varepsilon_i^{1/n_i}}{\varepsilon_j^{1/n_j}}\frac{C_i^{1/n_i}}{C_j^{1/n_j}} \approx \frac{\varepsilon_i^{1/n_i}}{\varepsilon_j^{1/n_j}} \tag{7}$$

The ratio spectra are insensitive to temperature, for normal terrestrial ranges. The approaches are adaptable for most sensors.

Alpha-residual method

The alpha-residual algorithm produces a relative emissivity spectrum that preserves spectral shape but, like the ratio methods, does not yield actual ε or T values. The alpha residuals are calculated utilizing Wien's approximation of Planck's law, which neglects the "−1" term in the denominator. This makes it possible to linearize the approximation with logarithms, thereby separating λ and T:

$$\begin{aligned} \frac{c_2}{T} \approx\ & \lambda_j \ln(\varepsilon_j) - \lambda_j \ln(L_j) \\ & + \lambda_j \ln(c_1) - 5\lambda_j \ln(\lambda_j) - \lambda_j \ln(\pi). \end{aligned} \tag{8}$$

Here c_1 and c_2 are the constants defined in Planck's law (Equation 1, *Land Surface Temperature*) and j is the image channel. Wien's approximation introduces a systematic error in ε_j of ~1 % at 300 K and 10 μm wavelength.

The next step is to calculate the means for the parameters of the linearized equation, summing over the n image channels:

$$\begin{aligned} \frac{c_2}{T} \approx & \frac{1}{n}\sum_{j=1}^{n}\lambda_j \ln(\varepsilon_j) - \frac{5}{n}\sum_{j=1}^{n}\lambda_j \ln(\lambda_j) - \frac{1}{n}\sum_{j=1}^{n}\lambda_j \ln(L_j) \\ & + (\ln(c_1) - \ln(\pi))\frac{1}{n}\sum_{j=1}^{n}\lambda_j. \end{aligned} \tag{9}$$

The residual is calculated by subtracting the mean from the individual channel values. Collecting terms, a set of n equations is generated relating ε_i to L_i, independent of T:

$$\lambda_j \ln(\varepsilon_j) - \mu_\alpha = \lambda_j \ln(\lambda_j) - \frac{1}{n}\sum_{j=1}^{n}\lambda_j \ln(L_j) + \kappa_i. \tag{10a}$$

$$\kappa_i \approx 5\lambda_i \ln(\lambda_i) - \sum_{j=1}^{n}\lambda_j \ln(\lambda_i) - (\ln(c_1) - \ln(\pi))(\lambda_j - \bar{\lambda}) \tag{10b}$$

$$\mu_\alpha = \frac{1}{n}\sum_{j=1}^{n}\lambda_j \ln(\varepsilon_j); \quad \bar{\lambda} = \frac{1}{n}\sum_{j=1}^{n}\lambda_j \tag{10c}$$

Note that κ_i contains only terms which do not include the measured spectral radiances, L_i, and hence may be calculated from the constants. Although dependency on T has been eliminated, it has been replaced by the unknown μ_α, related to the mean emissivity, such that the total number of unknowns is unchanged. The components of the alpha-residual spectrum vary only with the measured radiances. They are defined as

$$\alpha_i \equiv \lambda_i ln(\varepsilon_i) - \mu_\alpha \tag{11}$$

and are equivalent to the right-hand side of Equation 10a (α is defined differently than in the TISI method).

Model approaches

In this section, three algorithms distinguished by their model assumptions are described. The most specific requires that both a value of ε and the wavelength at which it occurs be known. The next requires only that the value be known. The third does not require the value of the emissivity to be known, only that the emissivity at two known wavelengths be the same.

The model emissivity (or reference channel) method (Kahle et al., 1980) assumes that the value of ε for one of the image channel's *ref* is constant and known a priori, reducing the number of unknowns to the number of measurements. First, the temperature is estimated using

$$T = \frac{c_2}{\lambda_{ref}}\left(\ln\left(\frac{c_1\varepsilon_{ref}}{\pi L_{ref}\lambda_{ref}^5}\right)+1\right)^{-1} \tag{12}$$

Lyon (1965) suggested that, for most rocks, the maximum emissivity (ε_{max}) was commonly ~0.95 and occurred at the long-wavelength end of the 8–14 μm TIR window. This observation has been used to justify the assumption $\varepsilon_{ref} = \varepsilon_{max}$, typically for $10 < \lambda_{ref} < 12$ μm.

Blackbody spectral radiances B_j for the remainder of the channels are next calculated from T and Planck's law. The model emissivities are $\varepsilon_j = L_j/B_j$.

No single value of ε_{ref} is appropriate for all surfaces. For example, for vegetation, $\varepsilon_{max} \approx 0.983$; if the value is assumed to be 0.95, the emissivities will be underestimated, the spectrum warped, and T overestimated by ~2.3 K. Vegetation, snow, and water are all subject to this kind of error. Also, reststrahlen bands for some types of rocks, for example, peridotite, occur near 10 μm, and ε_{max} occurs at shorter wavelengths. For these rock types, the errors may be even greater. Nevertheless, the model emissivity approach is robust and has the virtue of simplicity. It produces reliable results for a wide range of surface materials.

Retaining the assumption $\varepsilon_{ref} = \varepsilon_{max}$ but allowing the reference channel to vary, pixel by pixel, allows the model emissivity approach to be accurate for a wider range of materials. This approach is called the normalized emissivity method (NEM) (Gillespie, 1985; Realmuto, 1990). First, the brightness temperature T_b is found for each image channel, using Planck's law. T_b differs from channel to channel only if ε_j does also, since the actual skin temperature must be the same. The channel j with the maximum T_b is also the channel for which the maximum ε_j occurs and becomes the reference channel. For 81 spectra evaluated by Hook et al. (1992), 58 % of the temperatures found by the NEM algorithm were accurate to within 1 K, compared to only 21 % of temperatures recovered using the model emissivity method.

Finding the maximum T_b has been called the "Planck draping" method (Figure 3). This approach has been used to estimate $\varepsilon(\lambda)$ from high-resolution radiance spectra collected by hyperspectral imagers such as SEBASS or by field spectrometers.

Instead of examining the same scene element at two different times and temperatures, as in the day–night method, the scene element may be measured at different wavelengths λ_i and λ_j, chosen such that $\varepsilon_i = \varepsilon_j$. In such a case, it is necessary to find T (the "color temperature," T_c; see Equations 10 and 11, *Land Surface Temperature*) and only a single ε for the two channels, and the situation is deterministic (two measurements, L_i and L_j, and the two unknowns, T_c and $\varepsilon_i = \varepsilon_j$). As for the reference channel method, T_c can then be used to calculate a blackbody spectrum B, from which $\varepsilon(\lambda)$ can be found. This treatment has been called the "graybody emissivity method" (Barducci and Pippi, 1996).

The strength of the technique lies in its ability to recover emissivities even if the value of ε is unknown. The main weaknesses are that for imagers with only a few TIR channels, the basic requirement, $\varepsilon_i = \varepsilon_j$, is not met for much of the land surface, and it is not always possible to know λ_i and λ_j. If the assumption is valid, the accuracy for T is comparable to NEM, provided λ_i and λ_j are widely separated (e.g., Mushkin et al., 2005), but for most rock spectra, errors are $\geq$5 K. Barducci and Pippi (1996) proposed the graybody emissivity method for hyperspectral scanners, for which the basic requirement is more likely to be met.

Scaling approaches

Once relative spectra have been calculated, they can be calibrated to "absolute" emissivity provided a scaling factor is known. Applied to the ratio approach of Watson (1992b) or the TISI approach of Becker and Li (1990), this is basically the same as one of the model algorithms. However, scaling can also be done from empirical regression relating the shape of the emissivity spectrum to an absolute value at one wavelength. The regression is typically based on laboratory spectra of common scene components. More complex approaches also are possible: the first example given below combines the "two-channel,

two-time," and TISI approaches to convert the relative TISI spectra to emissivities.

The hybrid TISI approaches requires first that daytime and nighttime MIR and LWIR images be acquired and co-registered and that their TISI ratios be calculated. Essentially, there are four measurements ($L_{MIR,day}$, $L_{LWIR,day}$, $L_{MIR,night}$, and $L_{LWIR,night}$), four unknowns (ε_{MIR}, ε_{LWIR}), and one model assumption (the solar irradiance on the target). The MIR reflectivity is the complement of ε_{MIR} by Kirchhoff's law (for the complete mathematical development, see Dash, 2005). Using widely separated image channels improves the precision of T and ε recovery (e.g., Mushkin et al., 2005).

Alpha-derived emissivity (ADE) method

The ADE method (Kealy and Gabell, 1990; Hook et al., 1992; Kealy and Hook, 1993) is based on the alpha-residual approach. To recover ε_i, μ_α may be estimated via an empirical regression to the variance parameter v_α found for laboratory spectra:

$$v_\alpha = \frac{1}{n-1}\sum_{j=1}^{n}\alpha_j^2 \tag{13}$$

where α is defined in Equation 11. The best-fitting curves relating μ_α and v_α are of the form $\mu_\alpha = c v_\alpha^{1/x}$, where c and x are empirically determined coefficients ($c = -0.085$, $v_\alpha = 0.40$, and $r^2 = 0.935$ for ASTER).

Once the emissivities have been estimated, the temperature may be calculated using Planck's law. For 95 % of the library spectra, T was recovered within 1.6 K of the correct value, and Hook et al. (1992) showed that 67 % were accurate to within 1 K, compared to 58 % for the NEM.

The key innovation of the ADE approach is to utilize the empirical relationship between the average ε and a measure of the spectral contrast or complexity in order to restore the amplitude to the alpha-residual spectrum. The regression is based on the observation that, for a blackbody, the mean emissivity is unity and the spectral variance is zero. For minerals with reststrahlen bands or other emissivity features, the variance is greater than zero and, of course, the mean is less than unity. In use, the mean is predicted from the variance, which is calculated from the measured radiances.

Temperature–emissivity separation algorithm (TES)

The TES algorithm (Gillespie et al., 1998) uses a variant of the "minimum–maximum difference" or MMD approach of Matsunaga (1994) to scale relative emissivity spectra. TES is used to generate standard T and ε products from ASTER, but it has been generalized for different scanners. TES can work with as few as three channels provided the channel wavelengths are well chosen to capture the range of emissivities in scene spectra.

The MMD algorithm is related to the ADE algorithm, but is simpler. Whereas ADE utilizes the empirical relationship between the mean emissivity $\bar{\varepsilon}$ and the variance of alpha-residual emissivities, MMD utilizes an assumed linear relationship between $\bar{\varepsilon}$ and the range of the emissivities themselves, represented by the maximum–minimum difference or *MMD*.

The MMD algorithm requires that the ε spectrum be estimated (e.g., using NEM) in order to calculate *MMD*, from which $\bar{\varepsilon}$ is predicted. The apparent spectrum is then rescaled according to this average, T is calculated, and the process is iterated until the change in T is less than the $NE\Delta T$.

TES uses land-leaving spectral radiance and down-welling sky irradiance as input and provides a first guess for T and ε_j using the NEM algorithm. The correction for reflected sky irradiance is

$$L'_j = L_j - \frac{(1-\varepsilon_j)}{\pi} I_\downarrow \tag{14}$$

where L_j is the ground-leaving spectral radiance, compensated for atmospheric absorption and path radiance, $I_\downarrow$ is the down-welling sky irradiance, and $(1-\varepsilon_j)$ is the scene reflectivity (Kirchhoff's law). The NEM emissivities are then recalculated from L'_j and normalized:

$$\beta_j = \frac{\varepsilon_j}{\bar{\varepsilon}} \tag{15}$$

MMD is calculated from the β spectrum and used to predict ε_{min} (instead of $\bar{\varepsilon}$, as in the MMD approach), which is used for scaling:

$$\varepsilon_{min} = 0.994 - 0.687\,MMD^{0.737}; \quad \varepsilon_j = \beta_j\left(\frac{\varepsilon_{min}}{\beta_{min}}\right) \tag{16}$$

After early 2009, a linear regression ($\varepsilon_{min} = 0.8625 MMD + 0.955$) was used for scaling in TES (Gustafson et al., 2006) in order to improve TES precision for low-contrast spectra in standard ASTER data products. The TES algorithm differs from the MMD approach in using a better estimate of the emissivity and in basing the "absolute" measure of emissivity on ε_{min} rather than $\bar{\varepsilon}$, a difference that results in less scatter of the data about the regressed line and, hence, improved performance (± 1.5 K; $\pm$ 0.015 ε).

Classification-based algorithms

Classification approaches exploit the relationship between composition and ε and/or ρ to estimate ε pixel by pixel in at least one-image channel, generally in order to find T. T can then be used to calculate $\varepsilon(\lambda)$ in the other channels. Approaches that use channels in reflected sunlight (0.4–2.5 μm) require imagers with multiple, co-registered telescopes. They also make the assumption that TIR emissivities and visible–SWIR reflectivities are correlated. In some cases, for example, vegetation or water, the TIR emissivities can be predicted accurately; in others, for

example, many rocks, this assumption is less robust. Nevertheless, simply being able to distinguish rock and/or soil from vegetation can improve accuracy by 1–2 K. As an example, the NDVI approach (see Equation 9, *Land Surface Temperature*) makes use of co-registered visible red (~0.65 μm) and near-infrared (NIR: 0.7–1.2 μm) daytime image channels in order to recognize pixels that have a significant fraction of vegetation.

Conclusions

Only a fraction of published temperature–emissivity separation algorithms have been discussed here. (For an alternative summary, see Dash (2005).) Increasingly sophisticated approaches are being devised to improve on old treatments, for example, by using neural net technology to tune algorithms (e.g., Mao et al., 2008; Liang, 1997). However, the basic categories discussed above still apply.

For the most part, calibration inaccuracies, measurement uncertainty, and inaccurate atmospheric characterization all contribute to errors in the recovered LST and LSE. These errors are commonly as large as or larger than those attributable to the algorithms themselves, at least for the high-resolution imagers commonly used for Earth-surface studies. Therefore, algorithms themselves are now not the dominant factor limiting recovery accuracy. However, the next few years may see the introduction of a new generation of sensors, such as SEBASS, with dramatically improved measurement characteristics. In this case, atmospheric compensation may become the biggest source of uncertainty and deserving of attention. Likewise, the performance of some algorithms like the "two-time, two-channel" algorithm that now are strongly limited by measurement precision may improve relative to those algorithms that are limited by different factors, such as TES with its empirical regression of ε_{min} and *MMD*.

Bibliography

Barducci, A., and Pippi, I., 1996. Temperature and emissivity retrieval from remotely sensed images using the "grey body emissivity" method. *IEEE Transactions on Geoscience and Remote Sensing*, **34**(3), 681–695.

Becker, F., and Li, Z. L., 1990. Temperature-independent spectral indices in thermal infrared bands. *Remote Sensing of Environment*, **32**, 17–33.

Clark, R. N., Swayze, G. A., Livo, K. E., Kokaly, R. F., Sutley, S. J., Dalton, J. B., McDougal, R. R., and Gent, C. A., 2003. Imaging spectroscopy: earth and planetary remote sensing with the USGS Tetracorder and expert systems. *Journal of Geophysical Research*, doi:10.1029/2002JE001847.

Dash, P., 2005. *Land Surface Temperature and Emissivity Retrieval from satellite Measurements*. Dissertation, Forshungszentrum Karlsruhe in der Helmholtz-Gemeinschaft, Wissenschaftliche Betichte, FZKA 7095, 99 pp. Available from http://bibliothek.fzk.de/zb/berichte/FZKA7095.pdf. Last Accessed July 7, 2013.

Gillespie, A. R., 1985. Lithologic mapping of silicate rocks using TIMS. In *The TIMS Data Users' Workshop*, June 18–19, Jet Propulsion Laboratory Publication 86–38. Pasadena, CA: Jet Propulsion Lab, pp. 29–44.

Gillespie, A. R., Kahle, A. B., and Walker, R. E., 1986. Color enhancement of highly correlated images I. Decorrelation and HSI contrast stretches. *Remote Sensing of Environment*, **20**, 209–235.

Gillespie, A. R., Matsunaga, T., Rokugawa, S., and Hook, S. J., 1998. Temperature and emissivity separation from advanced spaceborne thermal emission and reflection radiometer (ASTER) images. *IEEE Transactions on Geoscience and Remote Sensing*, **36**, 1113–1126.

Gustafson, W. T., Gillespie, A. R., and Yamada, G., 2006. Revisions to the ASTER temperature/emissivity separation algorithm. In Sobrino, J. A. (ed.), *Second Recent Advances in Quantitative Remote Sensing*. Spain: Publicacions de la Universitat de València, pp. 770–775, ISBN 84-370-6533-X; 978-84-370-6533-5.

Hackwell, J. A., Warren, D. W., Bongiovi, R. P., Hansel, S. J., Hayhurst, T. L., Mabry, D. J., Sivjee, M. G., and Skinner, J. W., 1996. LWIR/MWIR imaging hyperspectral sensor for airborne and ground-based remote sensing. *Proceedings- SPIE The International Society For Optical Engineering*, **2819**, 102–107.

Hook, S. J., Gabell, A. R., Green, A. A., and Kealy, P. S., 1992. A comparison of techniques for extracting emissivity information from thermal infrared data for geologic studies. *Remote Sensing of Environment*, **42**, 123–135.

Hunt, G., 1980. Electromagnetic radiation: the communication link in remote sensing. In Siegal, B. S., and Gillespie, A. R. (eds.), *Remote Sensing in Geology*. New York: Wiley, pp. 5–45.

Jaggi, S., Quattrochi, D., and Baskin, R., 1992. An algorithm for the estimation of bounds on the emissivity and temperatures from thermal multispectral airborne remotely sensed data (Abstract). In Realmuto, V. J. (ed.), *Summary of the Third Annual JPL Airborne Geoscience Workshop*, June 1–5, Jet Propulsion Laboratory Publication 92–14. Pasadena, CA: Jet Propulsion Lab, pp. 22–24.

Kahle, A. B., and Rowan, L. C., 1980. Evaluation of multispectral middle infrared aircraft images for lithological mapping in the east Tintic Mountains, Utah. *Geology*, **8**, 234–239.

Kahle, A. B., Madura, D. P., and Soha, J. M., 1980. Middle infrared multispectral aircraft scanner data: analysis for geological applications. *Applied Optics*, **19**, 2279–2290.

Kealy, P. S., and Gabell, A. R., 1990. Estimation of emissivity and temperature using alpha coefficients. In *Proceedings of the 2nd TIMS Workshop*, Jet Propulsion Laboratory Publication 90–55. Pasadena, CA: Jet Propulsion Lab, pp. 11–15.

Kealy, P. S., and Hook, S. J., 1993. Separating temperature and emissivity in thermal infrared multispectral scanner data: implication for recovering land surface temperatures. *IEEE Transactions on Geoscience and Remote Sensing*, **31**(6), 1155–1164.

Liang, S. L., 1997. Retrieval of land surface temperature and water vapor content from AVHRR thermal imagery using artificial neural network. *International Geoscience and Remote Sensing Symposium Proceedings*, **3**, 1959–1961.

Lyon, R. J. P., 1965. Analysis of rocks by spectral infrared emission (8 to 25 microns). *Economic Geology*, **60**, 715–736.

Mao, K., Shi, J., Tang, H., Li, Z.-L., Wang, X., and Chen, K.-S., 2008. A neural network technique for separating land surface emissivity and temperature from ASTER imagery. *IEEE Transactions on Geoscience and Remote Sensing*, **46**(1), 200–208.

Matsunaga, T., 1994. A temperature-emissivity separation method using an empirical relationship between the mean, the maximum, and the minimum of the thermal infrared emissivity spectrum. *Journal of the Remote Sensing Society of Japan*, **14**(2), 230–241 (in Japanese with English abstract).

Mushkin, A., Balick, L. K., and Gillespie, A. R., 2005. Extending surface temperature and emissivity retrieval to the mid-infrared (3–5 μm) using the Multispectral Thermal Imager (MTI). *Remote Sensing of Environment*, **98**, 141–151.

Norman, J. M., and Becker, F., 1995. Terminology in thermal infrared remote sensing of natural surfaces. *Remote Sensing Reviews*, **12**, 159–173.
Palluconi, F. D., and Meeks, G. R., 1985. *Thermal Infrared Multispectral Scanner (TIMS): An Investigator's Guide to TIMS Data.* Jet Propulsion Laboratory Publication 85–32. Pasadena, CA: Jet Propulsion Lab, 14 pp.
Realmuto, V. J., 1990. Separating the effects of temperature and emissivity: emissivity spectrum normalization. In *Proceedings of the 2nd TIMS Workshop*, Jet Propulsion Laboratory Publication 90–55. Pasadena, CA: Jet Propulsion Lab, pp. 31–36.
Salisbury, J. W., and D'Aria, D., 1992. Emissivity of terrestrial materials in the 8–14 μm atmospheric window. *Remote Sensing of Environment*, **42**, 83–106.
Slater, P. N., 1980. *Remote Sensing, Optics and Optical Systems*. Reading, MA: Addison–Wesley, p. 575.
Soha, J. M., and Schwartz, A. A., 1978. Multispectral histogram normalization contrast enhancement. In *Proceedings of the 5th Canadian Symposium on Remote Sensing*, Victoria, British Columbia, Canada, pp. 86–93.
Wan, Z., 1999. MODIS land-surface temperature algorithm theoretical basis document (LST ATBD), Version 3.3. *NASA Contract NAS5-31370*, 37 pp.
Watson, K., 1992a. Two-temperature method for measuring emissivity. *Remote Sensing of Environment*, **42**, 117–121.
Watson, K., 1992b. Spectral ratio method for measuring emissivity. *Remote Sensing of Environment*, **42**, 113–116.

Cross-references

Crop Stress
Fields and Radiation
Land Surface Temperature
Optical/Infrared, Radiative Transfer
Volcanism

LAND SURFACE ROUGHNESS

Thomas Farr
Jet Propulsion Laboratory, California Institute of Technology, Pasadena, CA, USA

Synonyms

Microrelief; Microtopography

Definition

Surface roughness is usually defined at the human scales of centimeter to a few meter; larger scales are usually considered as topography. Relief at these scales is familiar to field geologists working at the outcrop scale and those interested in interpretation of landforms and earth-surface processes that form and modify them.

Scientific usefulness

One important surficial geologic process is aeolian erosion, transport, and deposition of sediments. The shear stress wind produces at the earth's surface is strongly affected by the surface roughness. The aerodynamic roughness parameter, z_0, depends on the wind speed profile as a function of height about the ground (Greeley et al., 1997). This parameter is used by geologists interested in aeolian processes as well as climatologists seeking to quantify atmospheric coupling with the solid earth.

Windblown dust and sand can also modify surface roughness by mantling and attenuating surface roughness (Farr, 1992; Arvidson et al., 1993). This can lead to estimates of relative age for surfaces such as lava flows or alluvial fans exposed to the same rate of aeolian deposition (Farr, 1992; Farr and Chadwick, 1996).

Streambed and ocean-bottom roughness also affect the flow and transport capabilities of water in those environments (e.g., Butler et al., 2001).

Other geologic processes produce or modify surface roughness, in particular volcanic eruptions which may mantle surfaces with ash or produce new roughness elements through extrusion of lava flows which can be relatively smooth pahoehoe or extremely rough aa. Roughness of lava flows can provide information on their eruption characteristics, such as rate and temperature (e.g., Lescinsky et al., 2007).

Land surface roughness strongly affects many remote sensing techniques. Observations of reflected visible-near-infrared wavelengths are affected by sub-resolution self-shadowing of roughness elements. Thus, rougher surfaces are darker, and the shadows are illuminated by sky light or reflections from adjacent land, shifting the spectral signature of the surface (Adams and Gillespie, 2006). At thermal infrared and microwave wavelengths, which are dominated by emission from solar-heated surfaces, roughness as well as larger-scale topography affects the initial heating of the surface while roughness also affects the efficiency of emission (Ulaby et al., 1982). Active microwave (radar) systems image surfaces through scattering of a transmitted wave from the surface. Smooth surfaces at the scale of the wavelengths, which are typically centimeter-meter, reflect energy away from the receiving antenna and are imaged as dark surfaces, while rough surfaces scatter the incident energy in all directions and show up in bright tones on radar images (Henderson and Lewis, 1998).

Much work has gone into quantitative models which seek to remove the effects of roughness on sub-resolution shadowing and thermal heating and emission (Tsang et al., 2000; Adams and Gillespie, 2006). In the radar area, inversion models have been developed which estimate the surface roughness from radar observations at different angles, polarizations, and wavelengths (Ulaby et al., 1982; Van Zyl et al., 1991; Evans et al., 1992; Dubois et al., 1995; Tsang et al., 2000).

Quantifying surface roughness

Good reviews of techniques for describing quantitatively surface roughness can be found in Dierking (1999), Thomas (1999), Shepard et al. (2001), and Campbell (2002), Chap. 3. The simplest description of surface

roughness is an estimate of the standard deviation (or root-mean square: RMS) of the surface heights (Table 1).

Describing the roughness of a surface by its RMS height leaves out any description of the scales of the roughness. One way to describe the scale of the roughness is to calculate the correlation length of profiles. Correlation length is a measure of how quickly heights change when moving along a profile. The autocorrelation function for a surface profile is calculated by sequentially stepping the profile across a stationary copy, multiplying, and normalizing. The autocorrelation is unity for 0 steps, or lags, and then drops as the number of lags increases (Figure 1). The rate of the drop-off, measured by the lag at which the autocorrelation value drops to 1/e, is called the correlation length, l. Smoother surfaces tend to have larger correlation lengths (Ulaby et al., 1982; p. 822).

Another way to describe quantitatively both the amplitude and scale of surface roughness is through the power spectrum, or power spectral density, usually of profiles. The power spectrum is basically the Fourier

Land Surface Roughness, Table 1 Measures of surface roughness for two natural surfaces. aa is a rough lava flow surface at Pisgah lava field in the Mojave Desert. Playa is a smooth dry lake surface at Lunar Crater volcanic field in central Nevada. Profiles were measured at 1 cm spacing

		aa	Playa
RMS height (cm)		9.8	1.9
Correlation length (cm)		26	46
Power spectrum	Slope	−2.19	−2.24
	Offset	−1.69	−3.45

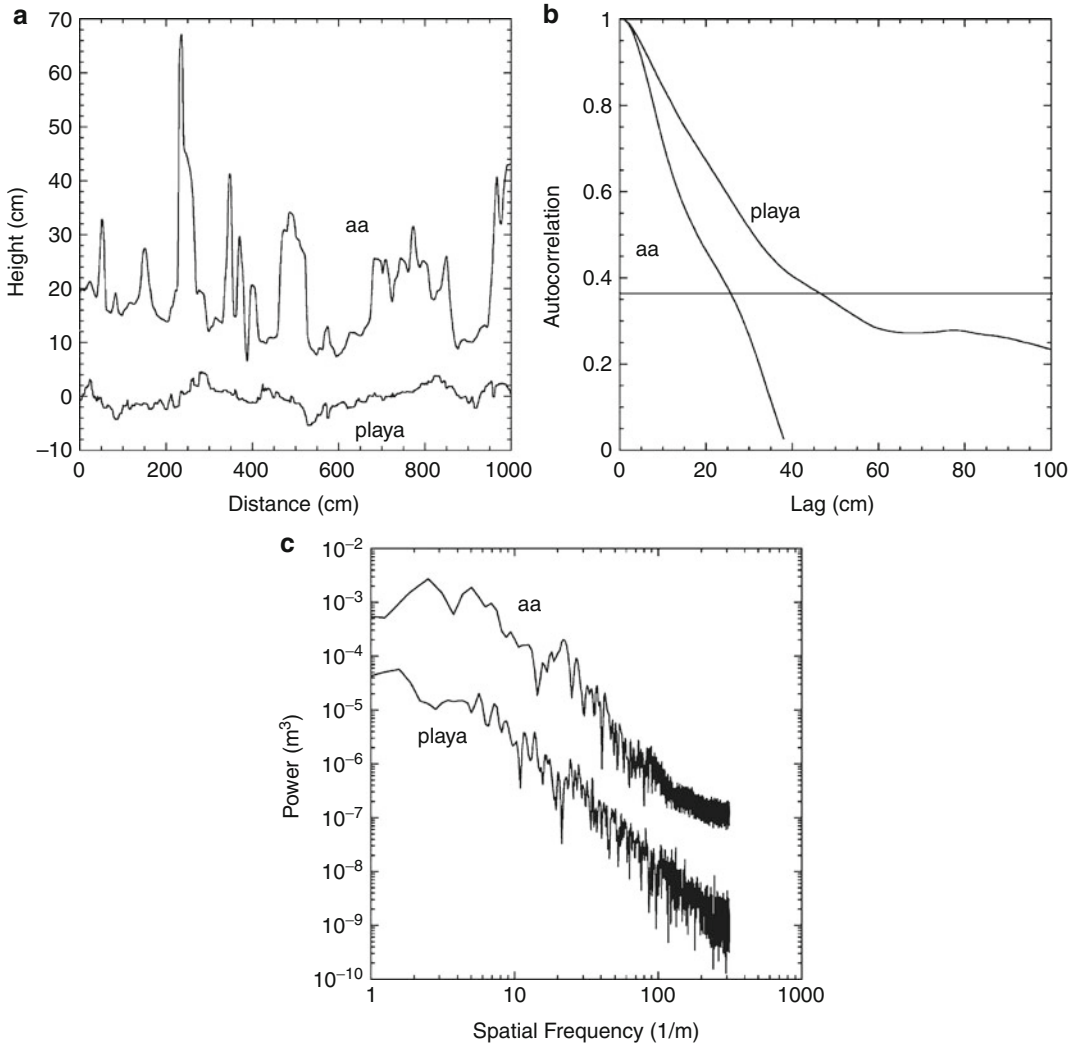

Land Surface Roughness, Figure 1 Profiles and surface roughness measures of two natural surfaces: an aa lava surface (*rough*) and a playa surface (*smooth*). (**a**) Profiles: aa profile has been offset 20 cm for clarity. (**b**) Autocorrelation functions for the two profiles. Note rapid drop-off of aa autocorrelation. *Horizontal line* is at 1/e. (**c**) Power spectra of the two profiles. Note they are nearly linear (in log-log plot) and parallel. Playa has much less power at all spatial frequencies.

transform of the profile (or two-dimensional microtopography) (e.g., Bendat and Piersol, 1986; Brown and Scholz, 1985; Austin et al., 1994). This produces a plot showing power, or variance, as a function of spatial frequency or scale (Figure 1). When plotted in log-log coordinates, the functions are found to be approximately linear (e.g., Berry and Hannay, 1978; Farr, 1992; Shepard et al., 2001), indicating a power-law relationship between roughness and scale. This relationship simplifies the quantitative description of the power spectrum of a profile to two numbers: the slope and offset (Table 1). Power spectrum slope is a measure of self-similarity and is related to fractal dimension of a profile, D, by (Brown, 1985):

$$D = \frac{5 + \text{slope}}{2}$$

Power spectrum offset is a measure of overall roughness, sometimes called "roughness amplitude" (Huang and Turcotte, 1989, 1990; Goff, 1990).

Measurement of surface roughness

Measurement of surface roughness at scales of centimeter to several meters is difficult, especially as the area covered must be large enough to make statistically significant calculations of quantities described above for natural surfaces. This usually means measuring an area or profiles 10–20 m or more in size. Techniques used to date include templates (Shepard et al., 2001); stereophotogrammetry from handheld and balloon-borne cameras and from a helicopter (Wall et al., 1991; Farr, 1992); and more recently ground-based lidar systems (Morris et al., 2008). All of these techniques have provided cm or better resolution, but helicopter stereophotogrammetry and ground-based lidar have provided the best coverage.

Summary

Land surface roughness at scales of centimeter to several meters is important in several areas of earth science as well as in the interpretation of remote sensing data. Roughness can be quantified in a variety of ways, but power spectral analysis is best at describing roughness and its scaling properties.

Acknowledgment

This research was carried out at the Jet Propulsion Laboratory, California Institute of Technology, under a contract with the NASA.

Bibliography

Adams, J. B., and Gillespie, A. R., 2006. *Remote Sensing of Landscapes with Spectral Images: a Physical Modeling Approach*. Cambridge, UK: Cambridge University Press, p. 362.

Arvidson, R. E., Shepard, M. K., Guinness, E. A., Petroy, S. B., Plaut, J. J., Evans, D. L., Farr, T. G., Greeley, R., Lancaster, N., and Gaddis, L. R., 1993. Characterization of lava-flow degradation in the Pisgah and Cima volcanic fields, California, using Landsat Thematic Mapper and AIRSAR data. *Geological Society of America Bulletin*, **105**, 175–188.

Austin, R. T., England, A. W., and Wakefield, G. H., 1994. Special problems in the estimation of power-law spectra as applied to topographical modeling. *IEEE Transactions on Geoscience and Remote Sensing*, **32**, 928–939.

Bendat, J. S., and Piersol, A. G., 1986. *Random Data, Analysis and Measurement Procedures*, 2nd edn. New York: Wiley, p. 566.

Berry, M. V., and Hannay, J. H., 1978. Topography of random surfaces, comment and reply. *Nature*, **273**, 573.

Brown, S. R., 1985. A note on the description of surface roughness using fractal dimension. *Geophysical Research Letters*, **14**, 1095–1098.

Brown, S. R., and Scholz, C. H., 1985. Broad bandwidth study of the topography of natural rock surfaces. *Journal of Geophysical Research*, **90**, 12575–12582.

Butler, J. B., Lane, S. N., and Chandler, J. H., 2001. Characterization of the structure of river-bed gravels using two-dimensional fractal analysis. *Mathematical Geology*, **33**, 301–330.

Campbell, B. A., 2002. *Radar Remote Sensing of Planetary Surfaces*. Cambridge, UK: Cambridge University Press, p. 331.

Dierking, W., 1999. Quantitative roughness characterization of geological surfaces and implications for radar signature analysis. *IEEE Transactions on Geoscience and Remote Sensing*, **37**, 2397–2412.

Dubois, P. C., vanZyl, J., and Engman, T., 1995. Measuring soil moisture with imaging radar. *IEEE Transactions on Geoscience and Remote Sensing*, **33**, 915–926.

Evans, D. L., Farr, T. G., and van Zyl, J. J., 1992. Estimates of surface roughness derived from synthetic aperture radar (SAR) data. *IEEE Transactions on Geoscience and Remote Sensing*, **30**, 382–389.

Farr, T. G., 1992. Microtopographic evolution of lava flows at Cima volcanic field, Mojave Desert, California. *Journal of Geophysical Research*, **97**, 15171–15179.

Farr, T. G., and Chadwick, O. A., 1996. Geomorphic processes and remote sensing signatures of alluvial fans in the Kun Lun Mountains, China. *Journal of Geophysical Research*, **101**, 23091–23100.

Goff, J. A., 1990. Comment on "Fractal mapping of digitized images: application to the topography of Arizona and comparisons with synthetic images". *Journal of Geophysical Research*, **95**, 5159–5161.

Greeley, R., Blumberg, D., McHone, J. F., Dobrovolskis, A., Iversen, J. D., Lancaster, N., Rasmussen, K. R., Wall, S. D., and White, B. R., 1997. Application of spaceborne radar laboratory data to the study of aeolian processes. *Journal of Geophysical Research*, **102**, 10,971–10,983.

Henderson, F. M., and Lewis, A. J. (eds.), 1998. *Principles and Applications of Imaging Radar, Manual of Remote Sensing*. New York: Wiley, Vol. 2, p. 866.

Huang, J., and Turcotte, D. L., 1989. Fractal mapping of digitized images: application to the topography of Arizona and comparisons with synthetic images. *Journal of Geophysical Research*, **94**, 7491–7495.

Huang, J., and Turcotte, D. L., 1990. Fractal image analysis: application to the topography of Oregon and synthetic images. *Journal of the Optical Society of America*, **7**, 1124–1130.

Lescinsky, D. T., Skoblenick, S. V., and Mansinha, L., 2007. Automated identification of lava flow structures using local Fourier spectrum of digital elevation data. Journal of Geophysical Research, **112**, doi:10.1029/2006JB004263.

Morris, A. R., Anderson, F. S., Mouginis-Mark, P. J., Haldemann, A. F. C., Brooks, B. A., and Foster, J., 2008. The roughness of Hawaiian volcanic terrains. *Journal of Geophysical Research*, **113**, E12007.

Shepard, M. K., Campbell, B. A., Bulmer, M. H., Farr, T. G., Gaddis, L. R., and Plaut, J. J., 2001. The roughness of natural terrain: a planetary and remote sensing perspective. *Journal of Geophysical Research*, **106**, 32,777–32,795.
Thomas, T. R., 1999. *Rough Surfaces*. London: Imperial College London, p. 278.
Tsang, L., Kong, J. A., and Ding, K. H., 2000. *Scattering of Electromagnetic Waves: Theories and Applications*. New York: Wiley, p. 426.
Ulaby, F. T., Moore, R. K., and Fung, A. K., 1982. *Microwave Remote Sensing*. Reading: Addison-Wesley, Vol. 1, 2, 3, p. 2162.
van Zyl, J. J., Burnette, C. F., and Farr, T. G., 1991. Inference of surface power spectra from inversion of multifrequency polarimetric radar data. *Geophysical Research Letters*, **18**, 1787–1790.
Wall, S. D., Farr, T. G., Muller, J.-P., Lewis, P., and Leberl, F. W., 1991. Measurement of surface microtopography. *Photogrammetric Engineering and Remote Sensing*, **57**, 1075–1078.

Cross-references

Geomorphology
Geophysical Retrieval, Inverse Problems in Remote Sensing
Land Surface Emissivity
Lidar Systems
Microwave Radiometers
Microwave Surface Scattering and Emission
Radars
Radar, Scatterometers
Radar, Synthetic Aperture
Surface Truth
Trafficability of Desert Terrains

LAND SURFACE TEMPERATURE

Alan Gillespie
Department of Earth and Space Sciences, University of Washington, Seattle, WA, USA

Definition

Land surface temperature (LST). Average temperature of an element of the exact surface of the Earth calculated from measured radiance (for a complete definition, see Norman and Becker, 1995).
Blackbody. An ideal material absorbing all incident energy or emitting all thermal energy possible. A cavity with a pinhole aperture approximates a blackbody.
Color temperature. Temperature satisfying Planck's law for spectral radiances measured at two different wavelengths: for a gray body (this entry), for any emitter, or the blackbody temperature for which visual color is the same as some other source (e.g., in photography).
Emissivity ε. The efficiency with which a surface radiates its thermal energy.
Irradiance. The power incident on a unit area, integrated over all directions (Wm^{-2}).
Longwave infrared (LWIR). For most terrestrial surfaces (340– 240 K) peak thermal emittance occurs at LWIR (8–14 μm).
Mid-infrared (*MIR*). Forest fires (1,000–600 K) have peak thermal emittances in the MIR (3–5 μm).
MODTRAN. A computer code package that describes the generation and transmission of energy in the Earth's atmosphere. MODTRAN can be used to predict τ, $S_{\uparrow}$, and $I_{\downarrow}$ for terrestrial remote sensing (Berk et al., 2005).
Path radiance $S_{\uparrow}$. The power per unit area incident on a detector and emitted upward from within the atmosphere ($W\ m^{-2}\ sr^{-1}$).
Radiance. The power per unit area from a surface directed toward a sensor, in units of $W\ m^{-2}\ sr^{-1}$.
Reflectivity ρ. The efficiency with which a surface reflects energy incident on it.
Shortwave infrared (SWIR). Erupting basaltic lavas (1,400 K) have their maximum thermal emittance at 2.1 μm in a third atmospheric window (0.4–2.5 μm). Part of this spectral region (1.4–2.5 μm) is called the SWIR.
Sky irradiance $I_{\downarrow}$. The irradiance on the Earth's surface originating as thermal energy radiated downward by the atmosphere ($W\ m^{-2}$).
Spectral radiance L. Radiance per wavelength, in units of $W\ m^{-2}\ \mu m^{-1}\ sr^{-1}$.
Thermal infrared (*TIR*). Thermal energy is radiated from a body at frequencies or wavelengths in proportion to its temperature. The wavelengths for which this radiant energy is significant for most terrestrial surfaces (1.4–14 μm) are longer than the wavelength of visible red light and hence are known as thermal infrared. The TIR is subdivided into three ranges (LWIR, MIR, and SWIR) for which the atmosphere is transparent (atmospheric "windows") so that the energy can be measured from space.
Transmissivity τ. The efficiency with which a material transmits energy incident on it.

Introduction

Temperature is a fundamental property of the Earth's surface that can be determined remotely. At all spatial scales, temperature is used in energy-balance and ecological studies, and it is important for geothermal and volcanic monitoring. At fine scales, temperature images are used to identify "hot spots" in fighting fires. Recently, they have been important for monitoring the seasonal onset of melting and freezing conditions in the Arctic, where melting is anticipated to occur earlier, and freezing later, as "global warming" worsens.

The land surface temperature (LST) itself is not measured directly from airborne or spaceborne sensors. Instead, the surface radiates thermal energy in the thermal infrared (TIR) part of the spectrum. The energy is radiated in proportion to temperature; therefore, the temperature can be calculated from it.

Temperature is variable at all temporal scales, but diurnal and seasonal fluctuations are perhaps the most noticeable. Figure 1 compares day-and nighttime TIR images of the same scene, the summit of Mauna Loa, Hawaii. The daytime image is dominated by cooling due

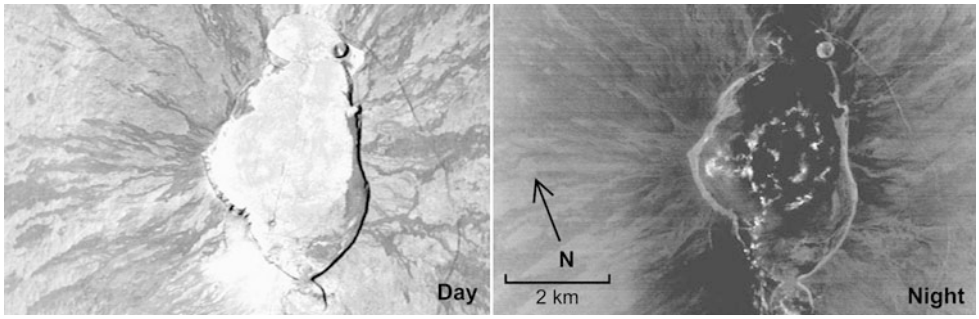

Land Surface Temperature, Figure 1 TIR radiance images of the caldera of Mauna Loa volcano, Hawaii. Satellite images from the multispectral thermal imager (MTI), acquired at 8.65 μm 10/09/00 (day) and 10/12/00 (night).

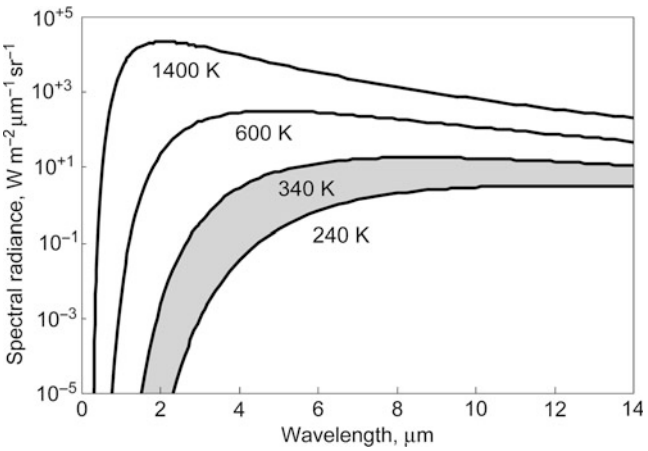

Land Surface Temperature, Figure 2 The spectrum of emitted spectral radiance for surfaces at different temperatures (note logarithmic scale on y-axis). Most terrestrial remote sensing is for surfaces between 340 and 240 K (*shaded area*). The peak spectral radiance occurs at longer wavelengths for cooler surfaces, but at any given wavelength it rises exponentially with temperature.

to topographic shading and thermal inertia of the lavas. Darker surfaces absorb more sunlight and so will be warmer. At night, the topographic effects are minimal, and white fractures in the lava (70 °C) delineate zones of geothermal heat rising within the caldera.

The basic equation governing relationship of surface or "skin" temperature and radiant energy is Planck's law (Figure 2):

$$B(\lambda, T) = \frac{c_1}{\pi\lambda^5}\left(\exp\left(\frac{c_2}{\lambda T}\right) - 1\right)^{-1} \quad (1)$$

where B is the spectral radiance (Wm^{-2} μm^{-1} sr^{-1}) at wavelength λ (μm) and temperature T (K) and $c_1 = 3.7418 \cdot 10^{-16}$ Wm^2 and $c_2 = 14{,}388$ μm K. It is assumed that the surface emits equally in all directions.

Integrating Equation 1 across all wavelengths gives the Stefan-Boltzmann law

$$j = \frac{\sigma}{\pi}T^4 \quad (2)$$

where j is the radiance (Wm^{-2} sr^{-1}) and $\sigma = 5.669 \times 10^8$ Wm^{-2} K^{-4}. For broadband measurements of j, inversion of Equation 2 could yield the LST.

Most surfaces are not perfect emitters, however, and a parameter called the emissivity (ε) is used to describe the efficiency with which they radiated heat. For a perfect emitter, $\varepsilon = 1$, but commonly $0.8 < \varepsilon < 1.0$. Therefore, for most surfaces $j = \varepsilon\sigma\pi^{-1}T^4$. Furthermore, ε varies with wavelength for many surfaces, including most geological surfaces of rock and soil (e.g., Lyon, 1965), so that Equation 1 also must be modified by including the multiplicative factor, $\varepsilon(\lambda)$. Inversion of this modified Planck function is generally used to calculate LST. Because it is underdetermined, however, additional information is required for solution. Providing these constraints is not straightforward, which is why there are numerous approaches. Figure 3 of "Land Surface Emissivity," compares radiance, temperature, and emissivity data for a TIR image.

The discussion that follows addresses several factors that complicate the calculation of LST: effects of atmospheric absorption, emission, and scattering on the measured spectral radiance; effects of land surface heterogeneity, including skin effects, and spatial integration during measurement of spectral radiance; short-term temporal fluctuations in the temperature field; and simplifying assumptions and algorithms used to recover temperatures.

Atmospheric effects

The Earth's atmosphere interacts with surface-emitted radiation as a function of surface elevation and atmospheric conditions, especially temperature and humidity profiles. Constituent gases such as ozone are also important. Atmospheric gases absorb differently across the spectrum, and at some wavelengths it is almost opaque. Remote sensing of the surface can only occur in atmospheric windows in spectral regions between these opaque bands. The three main windows for TIR remote

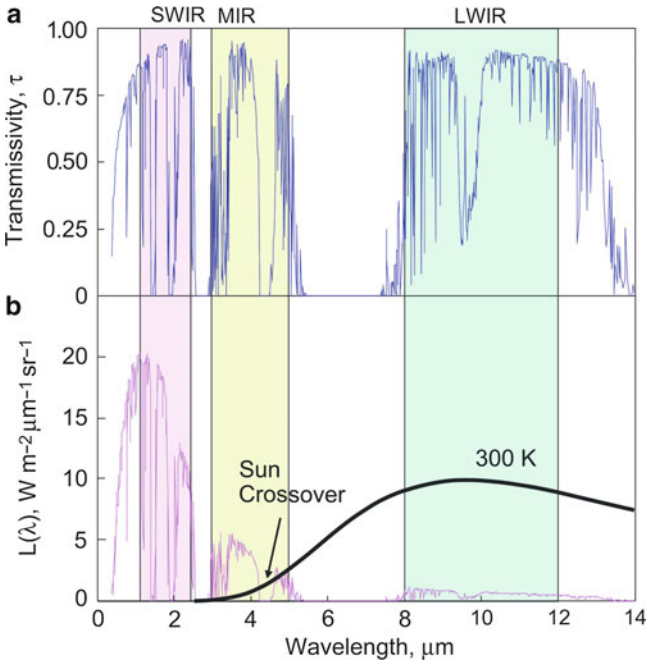

Land Surface Temperature, Figure 3 Radiance and transmissivity spectra. (**a**) Atmospheric transmissivity at sea level, zenith–nadir path (MODTRAN, mid-latitude summer atmosphere: Berk et al., 2005). (**b**) 300 K blackbody and sunlight reflected from a sea-level horizontal surface with 10 % albedo. Most remote-sensing detectors operate only within transparent atmospheric "windows" shown as labeled and *shaded bars*.

sensing are the longwave, mid-, and shortwave infrared (Figure 3). The maximum transmissivity $\tau(\lambda)$ of the atmosphere in the TIR is about 90 % (sea level). Therefore, it is necessary to account for atmospheric absorption and other effects quantitatively if accurate LSTs are to be recovered.

In addition to absorbing surface-emitted radiance, the atmosphere emits its own thermal energy in all directions. Two summary terms are important in the radiative transfer of energy from Earth to satellite: the upwelling "path radiance" ($L_{\uparrow}(\lambda)$) that never interacts with the land surface and the down-welling "sky irradiance" ($I_{\downarrow}(\lambda) = \pi L_{\downarrow}(\lambda)$), where $L_{\downarrow}$ is the equivalent average directional radiance (per steradian) term. Using these factors, the modified Planck function can be rewritten as

$$L(\lambda, T) = \tau(\lambda)\varepsilon(\lambda)B(\lambda, T) + L_{\uparrow}(\lambda) + \tau(1 - \varepsilon(\lambda))L_{\downarrow}(\lambda) \quad (3)$$

where L is the spectral radiance measured at the satellite and where the reflectivity and emissivity of the land surface are related by Kirchhoff's law:

$$\rho(\lambda) = (1 - \varepsilon(\lambda)). \quad (4)$$

The atmospheric terms and τ, $L_{\uparrow}$, and $L_{\downarrow}$ are themselves functions of the angle of the exitant ray relative to local zenith, as well as of the factors mentioned above. In evaluating Equation 3, it is important to note that there are five unknowns for a single spectral radiance measured from a homogeneous, isothermal surface. For multispectral data with n image channels at different wavelengths, there are $(1 + 4n)$ unknowns per measurement. This indeterminacy must be eliminated if LST is to be recovered.

Compensation for atmospheric effects

Before compensation can be attempted, the atmosphere must be characterized and the atmospheric parameters τ, $L_{\uparrow}$, and $L_{\downarrow}$ must be estimated. Probably the most common approach has been to use generalized atmospheric profiles of pressure, temperature, and humidity, from which the three parameters are estimated via an atmospheric radiative transfer model such as MODTRAN (e.g., Berk et al., 2005). Such an approach has been used in the retrieval of LST from Landsat TM5, for example, (Sobrino et al., 2004). This approach requires accounting for ground elevations using a digital elevation model (DEM).

It is potentially more accurate to estimate τ, $L_{\uparrow}$, and $L_{\downarrow}$ pixel by pixel, from the remote-sensing data themselves, as is done by MODIS to recover atmospheric profiles of temperature and humidity (Seeman et al., 2006). These profiles are then used in atmospheric radiative transfer models to calculate τ, $L_{\uparrow}$ and $L_{\downarrow}$. But profile recovery requires a complex sensor with many bands in and out of the LWIR window, and most remote-sensing platforms do not support this level of TIR measurement. Some airborne scanners such as NASA's MODIS Airborne Simulator (MAS) do allow measurements across an H_2O absorption band at 0.93 μm, from which total column water (TCW) can be estimated (Conel et al., 1988; Gao and Goetz, 1990). TCW can be used to constrain MODTRAN by scaling the default or assumed humidity profiles such that the measured integral is the TCW (Tonooka et al., 2005).

ASTER does not use internal image data to estimate atmospheric characteristics, but relies on reanalysis data from radiosonde balloons, launched routinely from weather stations and airports, interpolated to a 1° latitude/longitude grid and sampled every 6 h (e.g., Kalnay et al., 1996; Tonooka and Palluconi, 2005). They and a DEM are input to MODTRAN. The atmospheric data are available over the Internet (http://www.cpc.ncep.noaa.gov/products/wesley/reanalysis.html, last accessed 15 August 2008).

Because τ, $L_{\uparrow}$, and $L_{\downarrow}$ are partly correlated, it has proven possible to use just two LWIR channels in order to estimate them, provided the surface emissivities are known (Wan and Dozier, 1996). This is the case for the oceans, and such a two-channel or "split-window" algorithm for calculating sea surface temperature (SST) was developed and tested successfully early in the history of terrestrial remote sensing (Anding and Kauth, 1970). Details of this approach for SSTs are available in "Ocean, Measurements and Applications" and "Sea Surface Temperature."

For images of constant or known high emissivity (~1.0), especially of grasslands or forests, it is possible to normalize the atmospheric τ and $L_{\uparrow}$ from channel to channel of a multispectral TIR image (Young et al., 2002), eliminating the need to measure it independently. In this approach, $L_{\downarrow}$ is overlooked because ρ is near zero. A reference channel *ref* is chosen, and variation diagrams are constructed in which $L(\lambda_i)$ is plotted against $L(\lambda_{ref})$ for enough pixels that a range of LSTs are represented. A line fit to the high radiance edge of the data cluster will have a slope of τ and an intercept of $L_{\downarrow}$, where these parameters are relative to those for the reference channel. This approach is successful in removing the appearance of atmospheric effects from multispectral images, but a whole-spectrum scaling still needs to be applied in order to accurately portray land-leaving spectral radiance.

Land surface heterogeneity

The temperature of the Earth's surface is variable in space and time at a wide range of scales. Both types of variability must be considered in TIR remote sensing.

Energy absorbed or radiated from the surface changes the "skin temperature" of the immediate surface. This establishes a temperature gradient into the surface, and the skin temperature is not a completely accurate representation of the temperature of even the upper few centimeters of the Earth. Sensible heat transport, for example, cooling by wind, also creates a temperature gradient. Because wind is rarely constant, the LST fluctuates on a scale of seconds or minutes, with an amplitude of a few Kelvin, especially over vegetation. The ephemeral variability of LST means that measurements by remote scanners, with a dwell time of milliseconds at each pixel, are hard to compare to other remote or in situ measurements, since the exact time of measurements are unlikely to be the same. This is sometimes called the "snapshot" problem.

These considerations are especially important for energy-balance studies and validation exercises for LST products. However, rapid temporal fluctuations are most severe at fine scales (e.g., 10^0–10^1 m) and are reduced at the moderate scales (e.g., 10^1–10^3 m) of many civilian TIR scanners such as MODIS or GOES.

LST variability from point to point also poses a problem, because the measured radiance is integrated from surface elements of different temperatures:

$$L(\lambda, T_e) = \int B(\lambda, T_{x,y}) dx dy. \qquad (5)$$

where (x,y) are geographic coordinates. The temperature recovered by inversion of Equation 1 for the integrated spectral radiance yields an effective temperature, T_e. Because radiance is an exponential function of temperature, the exact relationship of T_e and the actual distribution of $T_{x,y}$ are hard to predict exactly and change over the day. For example, in a scene half covered by trees, T_e in the morning will be weighted toward the temperature of the trees, which warm faster than rock, but in the evening T_e will be weighted toward the temperature of the rock surface, which cools more slowly. This may not be a serious concern to all analysts. As an example, for an afternoon scene with 50 % trees at 280 K and 50 % rocks at 310 K, the effective temperature will be 296.3 K, only 1.3 K greater than the average skin temperature. However, this error is noticeable in, for example, an ASTER image.

Directional effects

Many remotely sensed images are acquired looking straight down through the atmosphere, but wide-angle images from airborne scanners and from AVHRR and MODIS have off-nadir look angles as large as ~55°. In addition to the dependency of atmospheric effects on the slant range, there are three effects that must be considered in calculating LST. These can lead to gradients in images of LST, such that the temperatures on the edges of the image may be hard to relate to those for equivalent surfaces viewed at nadir. First, in viewing rough surfaces at different angles, some views will include more shaded (typically cooler) surfaces, and others will include more sunlit surfaces (typically warmer). The magnitude of this effect depends on the time of day and the position of the sun, and the effect is minimized at night. However, during the day, the temperature difference between sunlit and shadowed surfaces may be 10 K or more, and the effect may be a few Kelvin across an LST image. This effect is not artifactual in that it is a faithful representation of the T_e field, and to remove it requires careful modeling and measurement of roughness. For daytime data, the ASTER stereo capability permits optical assessments of roughness (Mushkin and Gillespie, 2005) that could serve as input for such models. MODIS LST standard products have had to be made with the effects of non-Lambertian surfaces viewed at a range of angles from nadir in mind (Wan, 1999).

Second, specular reflection (Snyder and Wan, 1998) is also a factor at oblique view angles. This reflection is most obvious for smooth, mirrorlike surfaces such lakes and ponds. The reflected emittance may be from the sky ($L_{\downarrow}$) or from neighboring landscape elements. For images acquired within ~42° of nadir, reflected radiance is generally minimal.

Third, the bidirectional reflectance distribution (BRDF) of the surface may not be isotropic (e.g., Wan and Dozier, 1992). According to Kirchhoff's law, this means that a surface will look hotter from some angles than others. For rough surfaces, temperature differences due to shadowing (see above) can masquerade as an anisotropic BRDF; other surfaces may inherently be anisotropic. Because it is necessary to characterize the surface before the BRDF can be compensated for, it has been necessary to use generalized approaches (e.g., Wan, 1999).

Algorithms for calculating LST

Consideration of all the fluxes and factors contributing to the spatially integrated measurement of spectral radiance shows that accurate LST estimation is only possible under restricted circumstances or with independent constraints and simplifying assumptions. For example, it may be necessary to regard the landscape pixel as having a known, single emissivity ε and an effective temperature T_e which may, in fact, exist nowhere within the pixel. However, over decades of study, the assumptions have proven reasonable, and T_e has proven to be a useful measure.

Below, several common approaches for recovery of T_e are discussed. They are based either on the amplitude of the spectral radiance or on the shape of the spectrum if two or more image channels are measured. All approaches here are described assuming that the spectral range of measurement, $\Delta\lambda = f_2 - f_1$, is very narrow. If this is not the case, a calibration must be done to estimate the spectral radiance at the central wavelength of the sensor response $f(\lambda)$:

$$L(\lambda, T) \approx \frac{\int_{\lambda=f1}^{f2} f(\lambda)\varepsilon(\lambda)B(\lambda, T)d\lambda}{\int_{\lambda=f1}^{f2} f(\lambda)d\lambda} \tag{6}$$

Brightness temperature, T_b

The simplest estimate of LST is T_b, the temperature at which a blackbody ($\varepsilon \equiv 1.0$) would emit the remotely measured radiance. This approach is used when there is a single image channel. Finding T_b requires inverting the Planck function:

$$T_b = \frac{c_2}{\lambda \ln\left(\frac{c_1}{B(\lambda,T)\pi\lambda^5} + 1\right)} \tag{7}$$

where it is understood that λ refers to the central wavelength of the image channel.

Model temperature, T_m

In a slight variation, the surface emissivity may be estimated a priori to provide a refined estimate of LST (T_m). If the surface composition is known, the emissivity may be found from one of several spectral libraries available online (e.g., http://speclib.jpl.nasa.gov, last accessed 15 August 2008). For water and closed-canopy vegetation, the LWIR emissivity is >0.98. Many soils also have a high emissivity, >0.95. Lyon (1965) pointed out that, for most rocks, the emissivity at ~10 μm is ~0.95.

Once ε has been estimated, LST is found by

$$T_m = \frac{c_2}{\lambda \ln\left(\frac{c_1}{\varepsilon(\lambda)B(\lambda,T)\pi\lambda^5} + 1\right)} \tag{8}$$

Image classification has been used to determine surface composition, from which ε can be inferred. For example, van de Griend and Owe, (1993) showed that in the 8 – 14 μm spectral range, ε is highly correlated with NDVI, the normalized difference vegetation index, for different vegetation types:

$$\varepsilon \approx a + b \ln NDVI; NDVI = \frac{\rho 0.85 - \rho 0.65}{\rho 0.85 + \rho 065} \tag{9}$$

where ρ is evaluated at near-infrared ($\lambda = 0.85$ μm) and visible red ($\lambda = 0.65$ μm) wavelengths. Equation 9 allows ε to be estimated pixel by pixel, improving LST estimates especially for agricultural areas with simple geological substrates (homogeneous soils). Empirical coefficients a and b in Equation 9 are dependent on substrate emissivities, but if these can be estimated it is possible to extend greatly the range of surfaces for which accurate model LSTs can be calculated.

Model temperatures have been calculated for lava flowing from volcanoes, using Landsat Thematic Mapper (TM) Band 7 (2.25 μm) images and emissivities appropriate for lava (Pieri et al., 1990). The SWIR bands are effective because the peak thermal radiance is near 2 μm, whereas the emitted TIR radiance is too high and exceeds the dynamic range of the TIR band. Care must be taken because the emissivity of the hot lava appears to vary with temperature (Abtahi et al., 2001).

Color temperature, T_c

The simplest approach that utilizes the changing shape of the Planck function to estimate LST is a ratio of two spectral bands centered at λ_a and λ_b, and for which emissivities are known. The ratio is a monotonic function of temperature:

$$\frac{L(\lambda_a, T)}{L(\lambda_b, T)} = \frac{\varepsilon(\lambda_a)\lambda_b^5}{\varepsilon(\lambda_b)\lambda_a^5}\left(\frac{\exp\left(c_2(\lambda_b T)^{-1}\right) - 1}{\exp\left(c_2(\lambda_a T)^{-1}\right) - 1}\right). \tag{10}$$

Generally, it is assumed that $\varepsilon(\lambda_a) = \varepsilon(\lambda_b)$. Equation 10 is sometimes simplified further (Wien's approximation) by ignoring the (−1) term, such that

$$T_c = \left(\frac{c_2}{\lambda_b} - \frac{c_2}{\lambda_a}\right)\left(\ln\left(\frac{L(\lambda_a, T)\lambda_a^5}{L(\lambda_b, T)\lambda_b^5}\right)\right)^{-1} \tag{11}$$

For typical LSTs (e.g., 300 K), T_c is best calculated for widely separated central wavelengths, for example, 3 and 10 μm, because the ratio is more sensitive to LST, and therefore measurement precision has less of an effect on the recovered T_c. However, the use of MIR channels is generally limited to night time data because of the need to make large corrections for reflected sunlight.

Generalized split-window algorithm

Wan and Dozier, (1996) showed that provided the emissivity was known, the SST algorithm could be generalized for use over land. This algorithm is based on spectral radiance differences rather than ratios and has empirical coefficients a and b that permit the elimination of atmospheric effects. The form is

$$T_s = T_4 + \frac{1}{a-1}(T_4 - T_5) - \frac{b}{a-1} \qquad (12)$$

T_4 and T_5 are the brightness temperatures for AVHRR (Advanced Very High Resolution Radiometer) bands 4 and 5 (10.8 and 11.9 μm) or MODIS bands 31 and 32. Equation 12 can be generalized further to account for directional effects, but is still of the form of a difference equation.

Summary and conclusions

Temperature and emissivity are generally both unknown for "geological" surfaces of rock and soil and must be solved for simultaneously using inversion of Planck's equation. These algorithms thus go beyond just finding LST and are discussed in the entry "Land Surface Emissivity."

Because of the underdetermined nature of the modified Planck equation (Equation 2), no single solution for LST has been found that satisfies all analysts. Therefore, literally dozens of algorithms have been proposed, tested, and applied. This entry summarized only a few, representative of the basic approaches.

Bibliography

Abtahi, A. A., Kahle, A. B., Abbott, E. A., Gillespie, A. R., Sabol, D., Yamada, G., and Pieri, D., 2002. Emissivity changes in basalt cooling after eruption from Pu'u O'o, Kilauea, Hawaii. *Eos Transactions of the American Geophysical Union*, **83**(47), Fall Meeting Supplement, Abstract V71A–1263.

Anding, D., and Kauth, R., 1970. Estimation of sea surface temperature from space. *Remote Sensing of Environment*, **1**, 217–220.

Berk, A., Anderson, G. P., Acharya, P. K., Bernstein, L. S., Muratov, L., Lee, J., Fox, M., Adler-Golden, S. M., Chetwynd, J. H., Hoke, M. L., Lockwood, R. B., Gardner, J. A., Cooley, T. W., and Lewis, P. E., 2005. MODTRAN5: a reformulated atmospheric band model with auxiliary species and practical multiple scattering options. In *Proceedings of Algorithms and Technologies for Multispectral, Hyperspectral, and Ultraspectral Imagery*, SPIE, 5806: 662; DOI:10.1117/12.606026.

Conel, J. E., Green, R. O., Carrere, V., Margolis, J. S., Alley, R. E., Vane, G., Bruegge, C. J., and Gary, B. L., 1988. Atmospheric water mapping with the airborne visible/infrared imaging spectrometer (AVIRIS), Mountain Pass, CA. In Vane, G. (ed.), *Proceedings of the AVIRIS Performance Evaluation Workshop*. JPL Publication 88–38, Pasadena: Jet Propulsion Lab., pp. 21–26.

Gao, B.-C., and Goetz, A. F. H., 1990. Column atmospheric water vapor and vegetation liquid water retrievals from airborne imaging spectrometer data. *Journal of Geophysical Research-Atmospheres*, **95**, 3549–3564.

Kalnay, E., Kanamitsu, M., Kistler, R., Collins, W., Deaven, D., Gandin, L., Iredell, M., Saha, S., White, G., Woollen, J., Zhu, Y., Chelliah, M., Ebsuzaki, W., Higgins, W., Janowiak, J., Mo, K. C., Ropelewski, C., Wang, J., Leetma, A., Reynolds, R., Jenne, R., and Joseph, D., 1996. The NCEP/NCAR 40-year reanalysis project. *Bulletin of the American Meteorological Society*, **77**, 437–470.

Lyon, R. J. P., 1965. Analysis of rocks by spectral infrared emission (8 to 25 microns). *Economic Geology*, **60**(4), 715–736.

Mushkin, A., and Gillespie, A. R., 2005. Estimating sub-pixel surface roughness using remotely sensed stereoscopic data. *Remote Sensing of Environment*, **99**, 75–83.

Norman, J. M., and Becker, F., 1995. Terminology in thermal infrared remote sensing of natural surfaces. *Remote Sensing Reviews*, **12**, 159–173.

Pieri, D. C., Glaze, L. S., and Abrams, M. J., 1990. Thermal radiance observations of an active lava flow during the June 1984 eruption of Mt. Etna. *Geology*, **18**, 1018–1022.

Seeman, S. W., Borbas, E. E., Li, J., Menzel, W. P., and Gumley, L. E., 2006. MODIS atmospheric profile retrieval algorithm theoretical basis document, version 6. Available from http://modis.gsfc.nasa.gov/data/atbd/atbd_mod07.pdf. Accessed 7 June, 2013.

Snyder, W. C., and Wan, Z.-M., 1998. BRDF models to predict spectral reflectance and emissivity in the thermal infrared. *IEEE Transactions on Geoscience and Remote Sensing*, **36**, 214–255.

Sobrino, J. A., Jiménez-Muñoz, J. C., and Paolini, L., 2004. Land surface temperature retrieval from Landsat TM 5. *Remote Sensing of Environment*, **90**, 434–440.

Tonooka, H., 2005. Accurate atmospheric correction of ASTER thermal infrared imagery using the water vapor scaling method. *IEEE Transactions on Geoscience and Remote Sensing*, **43**(12), 2778–2792.

Tonooka, H., and Palluconi, F. D., 2005. Validation of ASTER/TIR standard atmospheric correction using water surfaces. *IEEE Transactions on Geoscience and Remote Sensing*, **43**(12), 2769–2777.

van de Griend, A. A., and Owe, M., 1993. On the relationship between thermal emissivity and the normalized difference vegetation index for natural surface. *International Journal of Remote Sensing*, **14**(6), 1119–1131.

Wan, Z., 1999. MODIS land-surface temperature algorithm theoretical basis document (LST ATBD), Version 3.3. Contract NAS5-31370.

Wan, Z., and Dozier, J., 1992. Effects of temperature-dependent molecular absorption coefficients on the thermal infrared remote sensing of the earth surface. In *Proceedings IGARSS'92*. pp. 1242–1245.

Wan, Z., and Dozier, J., 1996. A generalized split-window algorithm for retrieving land-surface temperature from space. *IEEE Transactions on Geoscience and Remote Sensing*, **34**(4), 892–905.

Young, S. J., Johnson, R., and Hackwell, J. A., 2002. An in-scene method for atmospheric compensation of thermal hyperspectral data. *Journal of Geophysical Research*, **107**(24), 4774, doi:10.1029/2001JD001266.

Cross-references

Crop Stress
Cryosphere and Polar Region Observing System
Fields and Radiation
Global Programs, Operational Systems
Land Surface Emissivity
Ocean, Measurements and Applications
Optical/Infrared, Radiative Transfer
Sea Surface Temperature
Thermal Radiation Sensors (Emitted)
Volcanism
Water and Energy Cycles
Water Vapor

LAND SURFACE TOPOGRAPHY

G. Bryan Bailey
USGS Earth Resources Observation and Science Center, Sioux Falls, SD, USA

Synonyms

Elevation; Landscape; Relief; Terrain

Definition

Topography of the Land Surface. The three-dimensional arrangement of physical attributes (such as shape, height, and depth) of a land surface in a place or region. Physical features that make up the topography of an area include mountains, valleys, plains, and bodies of water. Human-made features such as roads, railroads, and landfills are also often considered part of a region's topography (American Heritage Science Dictionary, 2005).

Importance of topographic information

The topography of the land surface is one of the most fundamental geophysical measurements of the Earth, and it is a dominant controlling factor in virtually all physical processes that occur on the land surface. Topography of the land surface also significantly controls processes within the overlying atmosphere, and it reflects the processes within the underlying lithosphere. Consequently, topographic information is important across the full spectrum of earth sciences.

Precipitation, runoff, soil moisture, incident sunlight, and temperature all vary with topography. Consequently, topography dominantly controls the local and regional distribution and character of vegetation. Erosion and sedimentation, and consequently soil formation and nutrient transport, also are strongly controlled by topography and are key factors in ecological studies. Topography strongly influences the location and magnitude of surface and subsurface water flow. Modeling of water supply and flood potential requires knowledge of the area's drainage extent, its slopes, and the pattern of the drainage network.

Particularly in rugged terrain, topography is commonly the dominant variable in remote sensing imagery. Topographic shading affects the radiance measured at every wavelength and is consequently the statistical principal component of many remotely sensed data sets. Meanwhile, atmospheric optical thickness varies inversely with topographic height, so that topography is an important factor in the atmospheric correction of remotely sensed data. Topographic data are imperative for the orthorectification of satellite imagery.

While topography controls many natural processes at and near the Earth's surface, many natural processes conversely control topography. Consequently, to various degrees, topography records and reveals evidence of current and past natural processes. An obvious example is the development and occurrence of erosional and depositional fluvial landforms. Tectonic, volcanic, glacial, and gravitational processes also produce characteristic landforms that reveal past and ongoing change. Consequently, topographic information is an important tool in the study of such processes (Crippen, 2008).

Describing the topography of the land surface

A *topographic map* (Figure 1) is a planimetric, or two-dimensional, representation of the three-dimensional configuration of the land surface where relief, or change in elevation, typically is represented by *contour lines*. A contour line is a line traced on the map such that all points on that line have the same elevation. That is, contour lines describe continuous points of equal elevation.

Until recent years, paper topographic maps were the most common tool used to describe the topography of the land surface. Until about 1940, most topographic maps were made by field crews who used alidades and plane tables to survey and map the topography of the landscape. World War II ushered in the age of *aerial photogrammetry* as the most common method for making topographic maps. This method, which uses overlapping and nadir-looking aerial photographs and a stereoplotter, revolutionized topographic mapping, resulting in greatly increased map coverage and enhanced map standardization (USGS, 1998).

Advances in computer technology brought about the latest great change in topographic mapping, the digital mapping revolution. Perhaps most notable was the replacement of the analog stereoplotter by the computer-assisted analytical stereoplotter. Not only has computer-assisted map production made it easier to make new paper maps and revise old ones, computer technology has accelerated demand for topographic data and other map information in *digital form* for use with the ever-growing number of computer-based mapping applications (McGlone, 2007).

A digital elevation model or DEM (Figure 2) is the generic term used most frequently to denote digital topographic data in all their various forms. The word "model" is applied because computers can use such data to model and automatically analyze the Earth's topography in three dimensions, thus avoiding much time-consuming human interpretation (Maune et al., 2007). Digital terrain model (DTM) and digital surface model (DSM) are two other common terms with similar meaning to DEM.

A *DEM* is a digital file consisting of terrain elevations for ground positions at regularly spaced horizontal intervals. The shorter those intervals are, the higher the spatial resolution of the DEM. The U.S. Geological Survey National Elevation Dataset (NED) typically has elevation data spaced at 30 m intervals, and it is thus said to have 30 m postings. DEMs are referenced to a vertical

G. Bryan Bailey has retired.

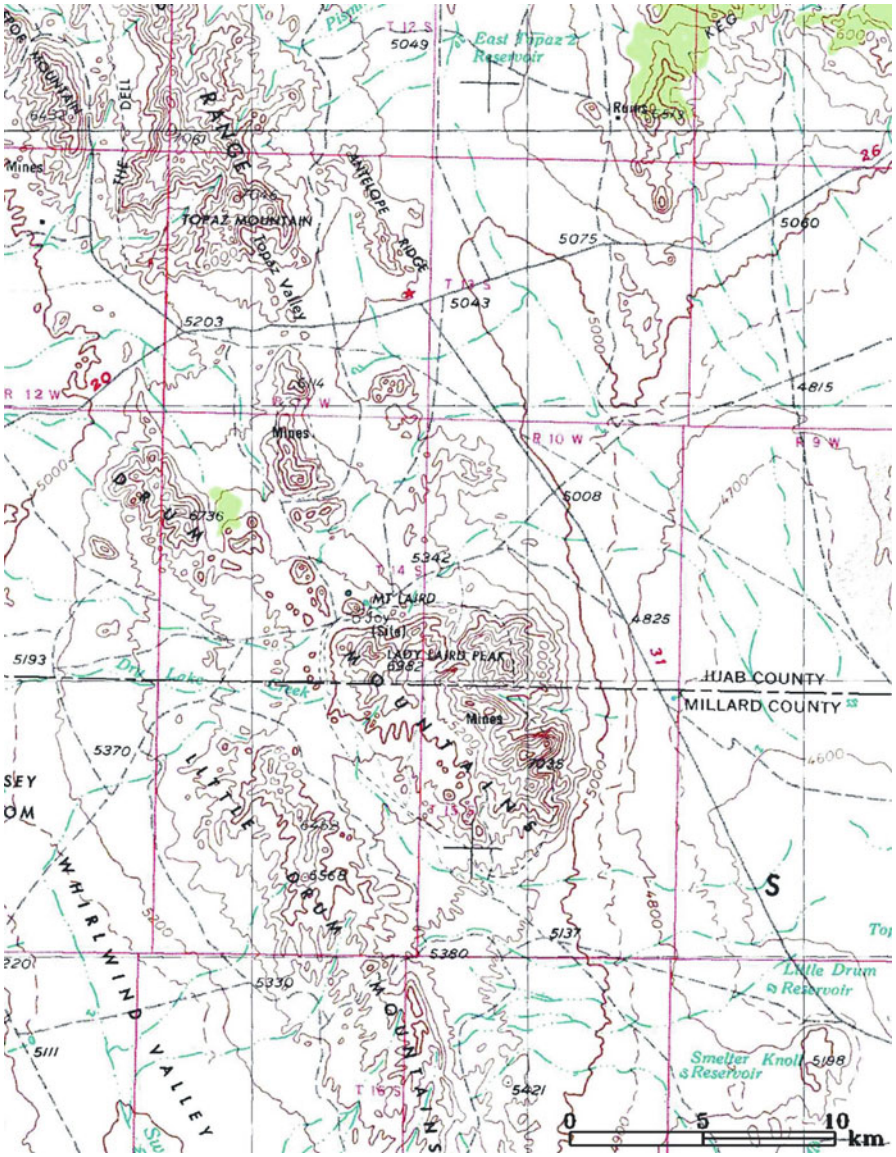

Land Surface Topography, Figure 1 Part of USGS 1:250,000 topographic map of the Drum Mts., Utah, area.

datum, such as the WGS84/EGM96 geoid, and to a geographic coordinate system, such as Universal Transverse Mercator (UTM).

Determining land surface topography from remotely sensed digital data

Many DEMs have been, and continue to be, generated by digitizing topographic maps produced largely by aerial photogrammetric techniques. However, today most DEMs of the Earth's land surface are being generated, using a variety of automated processes, directly from digital data acquired by a rather large variety of airborne sensors and land surface-imaging satellite systems.

Most DEMs produced today from remotely sensed digital data are derived from one of three primary sources: optical imaging systems, interferometric synthetic aperture radar systems, and lidar systems (McGlone, 2007).

Optical imaging systems

Three types of optical imaging sensors are used for photogrammetric production of DEMs: airborne film cameras, airborne digital sensors, and digital sensors onboard satellites. *Film mapping cameras*, for decades the staple of aerial photogrammetric mapping, continue to be important sources of stereo images for DEM generation. Aerial film is scanned by high-resolution scanners to produce digital

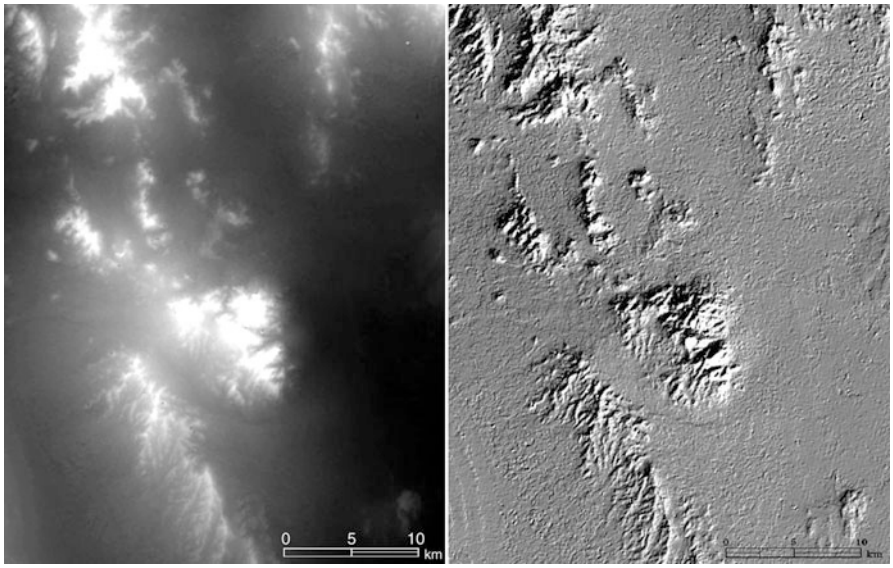

Land Surface Topography, Figure 2 DEM intensity image (*left*) and DEM shaded relief image (*right*) of the Drum Mts., Utah.

images that can be processed by a softcopy stereoplotter or by one of the many available DEM generation software systems (McGlone, 2007).

Airborne and spaceborne digital sensors capable of collecting imagery useful in the generation of DEMs have certain similarities, but they also have important differences. Airborne systems are essentially digital mapping cameras capable of acquiring very high-spatial-resolution images, but typically with fewer spectral bands than spaceborne optical imaging systems. Stereo acquisition by airborne digital sensors typically is achieved by overlap of successive images acquired along the flight path of the aircraft, similar to film mapping cameras.

Optimal stereo coverage for DEM generation by satellite sensors is achieved along the orbital track of the satellite by using two (or more) sensors. One of the sensors is nadir looking, while the other points at some fixed angle along the orbital track fore and/or aft of the spacecraft. Some satellite systems acquire stereo imagery from adjacent orbits by pointing across track, and some are able to acquire limited stereo coverage along the same orbit using a single sensor that looks forward to image an area from one angle and then is pointed backward to image the same area from a different angle.

Generating DEMs from imagery acquired by airborne or spaceborne digital sensors is accomplished with the aid of a softcopy stereoplotter or one of the many available DEM generation software systems. The process may or may not employ the use of ground control points (GCPs), and it typically involves a sequence of steps that include selecting tie points in each of the stereo pair, co-registration of the stereo images, stereo correlation for parallax difference measurement (image matching), and calculation of elevation values. In the co-registered stereo images, any positional differences between common points parallel to the direction of travel (parallax differences) are attributed to displacements caused by relief. Relative ground elevations are determined by measuring the parallax differences in the registered images, which then are converted to elevation (Lang and Welch, 1999).

Interferometric *SAR* systems

Synthetic aperture radars (SAR) illuminate the Earth's surface with microwave pulses, and they receive and record the return signals with respect to the magnitude and phase of those sine wave pulses (Bamler, 1997). While it is possible to generate accurate DEMs from stereo radar images using techniques similar to those described for optical imaging systems, DEMs are generated more commonly from *interferometric synthetic aperture radar* (InSAR).

InSAR exploits the phase of SAR signals to measure stereo parallaxes to an accuracy of a fraction of a wavelength. The phase of the return radar wave depends on the distance to the ground, so it is possible to accurately determine land surface elevation on a pixel-by-pixel basis from the phase information. To generate a DEM, InSAR uses two SAR images of the same land surface area taken from slightly different positions and determines phase differences between them, producing an image called an *interferogram*. Further processing of the interferogram results in the generation of a DEM of the land surface imaged by the two sensors (Henslely et al., 2007).

Lidar systems

Lidar stands for Light Detection and Ranging, and like radar, it is an active remote sensing system. Lidars use

laser technology to measure distances to specific points by transmitting pulses or continuous waves of light, amplifying the light that is scattered back, and recording the precise time the transmitted pulse takes to travel to the target and back (Fowler et al., 2007). Most lidar systems used today to produce DEMs are airborne systems, and they employ a variety of different beam steering or scanning strategies. They also operate at a wide range of altitudes above the land surface, depending on the resolution requirements for the DEM to be produced. DEMs produced from lidar data typically have significantly greater spatial detail and better accuracy than DEMs produced from optical imaging systems or InSAR.

Lidar is a complex remote sensing technology, and the data processing required to convert raw lidar data to DEMs also is complex. Typically, such processing is done by the company or agency that collects that data, because the processing software has been developed specifically for the lidar system that collected the data (Fowler et al., 2007). The lidar product most commonly associated with topography is a DEM known as the *bare earth model*, which is a product from which the processing has removed virtually all returns not associated with the bare land surface (Figure 3).

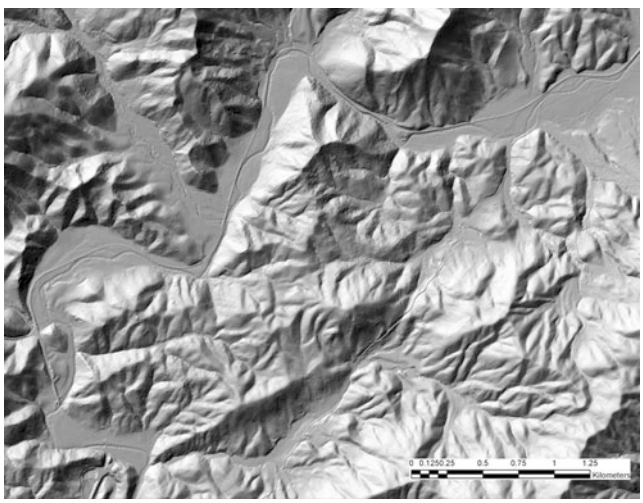

Land Surface Topography, Figure 3 Example of bare earth model DEM produced from lidar data collected over North Carolina.

Satellite systems that produce topographic data

This section briefly examines the system and data characteristics of selected Earth-observing *satellite systems* that acquire or have acquired data from which DEMs of the global land surface can be or have been generated. Airborne systems provide data from which highly accurate DEMs can be produced, but there is not one program or system that can provide such data for anywhere on the Earth's surface. The international remote sensing and earth science communities need access to quality DEMs for the entire global land surface, hence the emphasis here on satellite systems.

Radar satellite systems

Beginning in 1991, a number of polar-orbiting SAR satellite systems have been in operation, providing a continuous collective capability to acquire InSAR data from which DEMs can be generated for virtually any place on the global land surface. However, it was not until the 2010 launch of TanDEM-X, which operates in tandem formation with TerraSAR-X, that systematic efforts to produce a consistent global DEM from InSAR data were undertaken. Table 1 lists the SAR satellite systems that have contributed to DEM generation over the past two decades.

Shuttle radar topography mission (SRTM)

In 2000, the US National Aeronautics and Space Administration (NASA) and National Geospatial-Intelligence Agency (NGA) cooperated with the German Space Agency (DLR) to fly a Space Shuttle mission dedicated to acquiring digital topographic data for more than 80 % of the Earth's land surface. NASA flew a C-band SAR and DLR flew an X-band SAR, both of which were configured with one antenna in the bay of the space shuttle and the other at the end of a 60 m collapsible mast. The mission lasted 11 days, and NASA's C-band SAR collected complete InSAR coverage of the global landmass between 60 °N to 56 °S latitude. The X-band SAR was not designed for uninterrupted coverage.

Land Surface Topography, Table 1 International SAR systems from which DEMs can be produced from InSAR data

Country/agency	Satellite/sensor	Band	Launch date	Still active
European Space Agency (ESA)	ERS-1	C-band	1991	No
ESA	ERS-2	C-band	1995	No
Canadian Space Agency (CSA)	RADARSAT-1	C-band	1995	No
CSA	RADARSAT-2	C-band	2007	Yes
Japan (JAXA)	JERS-1	L-band	1992	No
ESA	Envisat ASAR	C-band	2002	No
Japan (JAXA)	ALOS PALSAR	L-band	2006	No
Germany (DLR)	TerraSAR-X	X-band	2007	Yes
Germany (DLR)	TanDEM-X	X-band	2010	Yes

The SRTM DEM data set is available from NASA and from the U.S. Geological Survey at no charge to users. Data are at 1 arc-second (30 m) for the United States and its territories and 3 arc-seconds (90 m) for all other covered areas. Vertical accuracy specification for the 1 arc-second data was 16 m (Rabus et al., 2003), but the data frequently have vertical accuracies better than 10 m (at 90 % confidence).

SPOT satellites

The French Système Pour l'Observation de la Terre (SPOT) satellites have been capable of acquiring cross-track stereo digital imagery from which DEMs can be generated since their initial launch in 1984. Spatial resolution of SPOT sensors has increased over that time, so the spatial details of DEMs that can be generated from those data likewise have increased. Currently, SPOT Image offers for sale DEMs produced from SPOT optical image data that cover most of the global land surface. The DEMs have 30 m postings and a vertical accuracy of less than 10 m where the slope of terrain is less than 20 %.

ASTER

The Advanced Spaceborne Thermal Emission and Reflection Radiometer (ASTER) was built by the Japanese Ministry of Economy, Trade and Industry (METI), and it flies onboard NASA's Terra satellite. ASTER collects along-track stereo optical data with 15 m spatial resolution from which DEMs with 30 m postings are routinely produced as standard data products without the need for GCPs. The accuracy of ASTER DEMs varies some depending on terrain and other conditions, but they routinely have vertical accuracies better than 15 m (Fujisada et al., 2005). ASTER 60 km by 60 km DEMs are available for purchase to the general user from METI's Earth Resources Data Analysis Center and NASA's Land Processes Distributed Active Archive Center.

Since ASTER was launched in late 1999, more than two million scenes have been acquired of the global land surface. NASA and METI cooperated to produce a global DEM from these ASTER data. The *ASTER Global DEM*, which covers the Earth's landmasses from 83 °N to 83 °S latitude with nominal accuracies of 20 m vertical and 30 m horizontal at 95 % confidence, has 30 m postings. The ASTER Global DEM was contributed to the Global Earth Observing System of Systems (GEOSS) by NASA and METI, and thus it is available at no cost to users worldwide.

Cartosat and prism

Two optical imaging satellite systems that were designed to acquire data for generation of DEMs are the Indian Space Research Organisation's (ISRO) Cartosats and the Japanese Aerospace Exploration Agency's (JAXA) Prism sensor that flew onboard the Advanced Land Observation Satellite (ALOS). All acquire stereo image data along the orbital track. Cartosat-1 has a spatial resolution of 2.5 m with a 30 km swath, and Cartosat-2 has a spatial resolution of less than 1 m with a 9.6 km swath. Prism has a 2.5 m spatial resolution and a 35 km swath. DEMs are not offered as standard products by either ISRO or JAXA, but the image data are available for purchase.

Summary and conclusions

The topography of the land surface is one of the most fundamental geophysical measurements of the Earth, and it is a dominant controlling factor in virtually all natural physical processes that occur on the land surface. The topographic map, which is a planimetric representation of the three-dimensional land, has been the most common tool used to describe the topography of the land surface until recently. Now, digital topographic data, in the form of a DEMs, are the tools of choice for many who wish to characterize the topography of the land surface.

DEMs are most frequently generated by automated computer techniques from digital data acquired by airborne and spaceborne sensors. Locally to regionally, airborne film and electro-optical systems and lidar systems provide users with high-quality and very accurate DEMs. For global studies, spaceborne optical systems capable of acquiring stereo imagery and InSAR systems offer the opportunity to produce DEMs with improving quality and accuracy worldwide. The SRTM DEM that cover 80 % of the global land surface and the ASTER Global DEM that covers virtually all of it are examples of two recent contributions by land remote sensing systems to better characterize the global land surface topography. Almost certainly, even greater advancements will be achieved in the next few years.

Bibliography

Bamler, R., 1997. Digital terrain models from radar interferometry. In Fritsch, D., and Hobbie, D. (eds.), *Photogrammetric Week 1997*. Heidelberg: Wichmann Verlag, pp. 93–105.

Crippen, R. E., 2008. Global topographic exploration and analysis with the SRTM and ASTER elevation models. In *Elevation Models for Geoscience*, Special Publication. London: Geological Society (in press).

Fowler, R. A., Samberg, A., Flood, M. J., and Greaves, T. J., 2007. Topographic and terrestrial lidar. In Maune, D. F. (ed.), *Digital Elevation Model Technologies and Applications: The DEM Users Manuel*, 2nd edn. Bethesda: American Society of Photogrammetry and Remote Sensing, pp. 199–252.

Fujisada, H., Bailey, G. B., Kelly, G., Hara, S., and Abrams, M., 2005. ASTER DEM performance. *IEEE Transactions on Geoscience and Remote Sensing*, **43**, 2715–2724.

Henslely, S., Munjy, R., and Rosen, P., 2007. Interferometric synthetic aperture radar (IFSAR). In Maune, D. F. (ed.), *Digital Elevation Model Technologies and Applications: The DEM Users Manuel*, 2nd edn. Bethesda: American Society of Photogrammetry and Remote Sensing, pp. 141–198.

Lang, H. R., and Welch, R., 1999. *ATBD-AST-08 Algorithm Theoretical Basis Document for ASTER Digital Elevation Models (Standard Product AST14)*. Washington, DC: National Aeronautics and Space Administration/Earth Observing System Program, p. 69.

Maune, D. F., Kopp, S. M., Crawford, C. A., and Zervas, C. E., 2007. Introduction. In Maune, D. F. (ed.), *Digital Elevation Model Technologies and Applications: The DEM Users Manuel*,

2nd edn. Bethesda: American Society of Photogrammetry and Remote Sensing, pp. 1–36.
McGlone, J. C., 2007. Photogrammetry. In Maune, D. F. (ed.), *Digital Elevation Model Technologies and Applications: The DEM Users Manuel*, 2nd edn. Bethesda: American Society of Photogrammetry and Remote Sensing, pp. 119–140.
Rabus, B., Eineder, M., Roth, A., and Bamler, R., 2003. The shuttle radar topography mission: a new class of digital elevation models acquired by spaceborne radar. *ISPRS Journal of Photogrammetry and Remote Sensing*, **57**, 241–262.
The American Heritage® Science Dictionary Copyright © 2005 by Houghton Mifflin Company. Published by Houghton Mifflin Company.
USGS, 1998. *Topographic Mapping*. Reston: U.S. Geological Survey. (Out of print; online version: http://erg.usgs.gov/isb/pubs/booklets/topo/topo.html).

Cross-references

Geodesy
Geomorphology
Land Surface Roughness
Lidar Systems
Radar, Synthetic Aperture
Reflected Solar Radiation Sensors, Multiangle Imaging

LAND-ATMOSPHERE INTERACTIONS, EVAPOTRANSPIRATION

Joshua B. Fisher
Jet Propulsion Laboratory, California Institute of Technology, Pasadena, CA, USA

Synonyms

Evaporation; Water flux

Definition

Evapotranspiration (ET). The transfer of liquid water from open water and through plant transpiration to the atmosphere as water vapor.
Transpiration. The loss of water vapor through plant pores called stomata on leaves/needles or stems.

Basics of evapotranspiration

Evapotranspiration (ET) is the movement and transfer (i.e., flux) of water as a liquid at the Earth's surface to the atmosphere as a gas. ET is a combination of open water evaporation and plant transpiration. (Sublimation, which is the transition of solid water (i.e., ice, snow) to vapor due to low atmospheric pressure (i.e., high altitude), dry air, and high sunlight, is generally considered separate from ET.) Sources of open water evaporation could include oceans, seas, lakes, rivers, ponds, puddles, and water on objects such as plants, buildings, rocks, the soil surface (including movement of water vertically through the soil to the surface), or in the context of measuring devices such as a pan. Plants take up water from the soil through their roots, transferring that water through their stems via conduits called xylem to their leaves, where it is used in the process of photosynthesis. The photosynthetic machinery in leaves (e.g., chlorophyll) takes in CO_2 from the atmosphere through stomatal pores and combines it with water and energy (i.e., light) to create sugars used to maintain and grow plant tissue and functions. While stomata are open, plants may lose water from their leaves to the atmosphere – this water loss is called transpiration. Plants regulate the opening and closing of their stomata to minimize water loss (closed), yet maximize CO_2 absorption (open).

Energy is required to break the strong bonds that hold water molecules together as a liquid – when those bonds break, the individual water molecules may enter the surrounding atmosphere as vapor. Energy may be in the form of heat, radiation, or pressure. Regardless of the availability of energy, water molecules may not be able to enter the atmosphere if the atmosphere is already saturated with moisture (humidity) or if there is no wind to facilitate the transfer of the molecules from the water source to the atmosphere. The wind itself may be differentially influenced by friction as it passes over smooth versus rough surfaces. Therefore, solar radiation (or, indirectly, air temperature), air humidity, and wind speed are the main climate influences on ET. The main vegetative controls include leaf and canopy structures, regulation of stomata, and rooting dynamics. Finally, soil characteristics control soil moisture retention of precipitation inputs. All of these potential controls vary in influence depending on the system in question, as well as the associated spatial and temporal scales of analysis (Fisher et al., 2011).

Remote sensing of ET

ET can be measured "remotely" with instruments attached to towers extending over vegetation using the eddy covariance technique (e.g., FLUXNET: Baldocchi et al., 2001). These same instruments may be attached to airplanes for regional measurements. However, ET cannot be measured directly from satellite remote sensing, so it must be inferred from a model or the residual of other measurements. There are three orders of complexity in space-based estimation of ET:

- Simple: Empirical, semiempirical
- Intermediate: Water balance, energy balance
- Complex: Land surface/Earth system models

Empirical, semiempirical approaches

One of the simplest approaches to estimating ET is to take another closely related variable that is measureable and convert that to ET using a statistical relationship. The statistical relationship (e.g., linear regression) may be developed from studies where both the other variable and ET were measured and then used to extrapolate beyond the site. One commonly used variable is the Normalized Difference Vegetation Index (NDVI), as well as related "greenness" indices, constructed from

measurements primarily in the red and near-infrared (NIR) wavelengths, and which is indicative of plant productivity. Where there is plenty of water and energy, there will be both high NDVI and ET; where there is no water and energy, one would not expect much NDVI and ET. However, this relationship may fall apart, for example, under deforestation or nutrient limitation (high ET, low NDVI), or diurnal/seasonal water stress (low ET, high NDVI). NDVI may be obtained from satellite instruments such as the Advanced Very High Resolution Radiometer (AVHRR), the Moderate resolution Imaging Spectroradiometer (MODIS), or the Visible Infrared Imager Radiometer Suite (VIIRS).

Another commonly used variable is Land Surface Temperature (LST), constructed from thermal-infrared (TIR) measurements. A given surface may be cooled (lower LST) when evaporating and hotter when there is less ET. However, other forces may change the temperature of the surface, including advecting warm/cool/dry/moist air. LST may be obtained from satellite instruments such as MODIS, the Atmospheric Infrared Sounder (AIRS), or Landsat. LST may be combined with NDVI for a somewhat more complex empirical approach. One of the leading empirical approaches comes from the MPI-BGC product, which is constructed from a machine learning technique and model tree ensemble that developed statistical relationships between measured ET and globally available ancillary data at over 250 FLUXNET sites (Jung et al., 2009). Finally, many agriculturalists use semiempirical algorithms to estimate ET, using physics-based equations for potential ET (PET), then converting or downscaling PET to actual ET (AET) using an empirical scalar multiplier, called a crop coefficient, developed for their specific crop and location.

Water balance

ET may be calculated as the residual of known measurements in the water balance equation:

$$P = dS + Q + ET \tag{1}$$

where P is precipitation (rainfall and snow); dS is the change in stored standing water (e.g., lakes, ponds, or in/on plants), soil moisture, and groundwater; and Q is runoff. From a remote sensing standpoint, rainfall is measured from a variety of satellites including the Tropical Rainfall Measuring Mission (TRMM) (the Global Precipitation Mission (GPM) is currently in development as the next major multi-satellite precipitation-measuring mission) and snow from MODIS. dS is measureable at large spatial scales from the Gravity Recovery And Climate Experiment (GRACE). Q is not yet measureable from space, (The proposed Surface Water Ocean Topography (SWOT) mission currently in development would measure river discharge from space.) but is readily obtained from river discharge measurements, though many rivers are sparsely instrumented, for example, in developing nations. Equation 1 may be rearranged to solve for ET given the known measurements of the three other variables in the equation.

Energy balance

ET may also be considered an energy (water fluxes such as precipitation and ET are usually given in units of depth per time (i.e., mm · day^{-1}); the units are consistent when they are in volume per area per time (i.e., m^3 · ha^{-1} · day^{-1}). 1 m^3 is equal to 1,000 l. Water can also be expressed in units of mass – 1 kg of water is equal to 1 mm of water spread over 1 m^2. ET, like R_n, can be expressed in units of energy too. Because it requires 2.45 MJ to vaporize 1 kg of water (at 20°C), 1 kg of water is therefore equivalent to 2.45 MJ; 1 mm of water is thus equal to 2.45 MJ · m^{-2}) variable, called the latent heat of evaporation (LE), as it requires a certain amount of energy to convert a given quantity of liquid water to gas. Energy coming from the sun less any radiation that gets reflected back to the atmosphere – or net radiation (R_n) – is energy available to drive ET. Any R_n that does not drive ET either gets converted to sensible heat (H) or stored in the soil or other objects (G):

$$R_n = ET + H + G \tag{2}$$

A few space-based R_n are available, including those from the Surface Radiation Budget (SRB), the Clouds and Earth's Radiant Energy System (CERES), the International Satellite Cloud Climatology Project (ISCCP), and MODIS. H and, to a lesser extent, G are not remotely measureable and are the focus of models such as the Surface Energy Balance System (SEBS), the Atmosphere-Land Exchange Inverse (ALEXI), the Surface Energy Balance Algorithm for Land (SEBAL), and Mapping EvapoTranspiration at high Resolution with Internalized Calibration (METRIC), all of which rely particularly on remotely sensed LST (Li et al., 2009).

Direct approaches

ET may also be calculated "directly" from the physics that control ET, as outlined earlier in the "Basics of Evapotranspiration" subsection. The most widely used equation for determining ET comes in the form of the Penman-Monteith equation:

$$ET = \frac{\Delta R_n + \frac{c_p \rho VPD}{ra}}{\Delta + \gamma + \gamma\left(\frac{r_s}{r_a}\right)} \tag{3}$$

where Δ is the slope of the saturation-to-vapor pressure curve, c_p is the specific heat of water, ρ is air density, VPD is vapor pressure deficit, r_a is aerodynamic resistance, γ is the psychrometric constant, and r_s is surface resistance. Equation 3 forms the foundation of the algorithm for the official MODIS ET product (MOD16) (Mu et al., 2011), which relies on MODIS-based leaf area index (LAI), fraction of absorbed photosynthetically active radiation (fAPAR), land cover, and a general

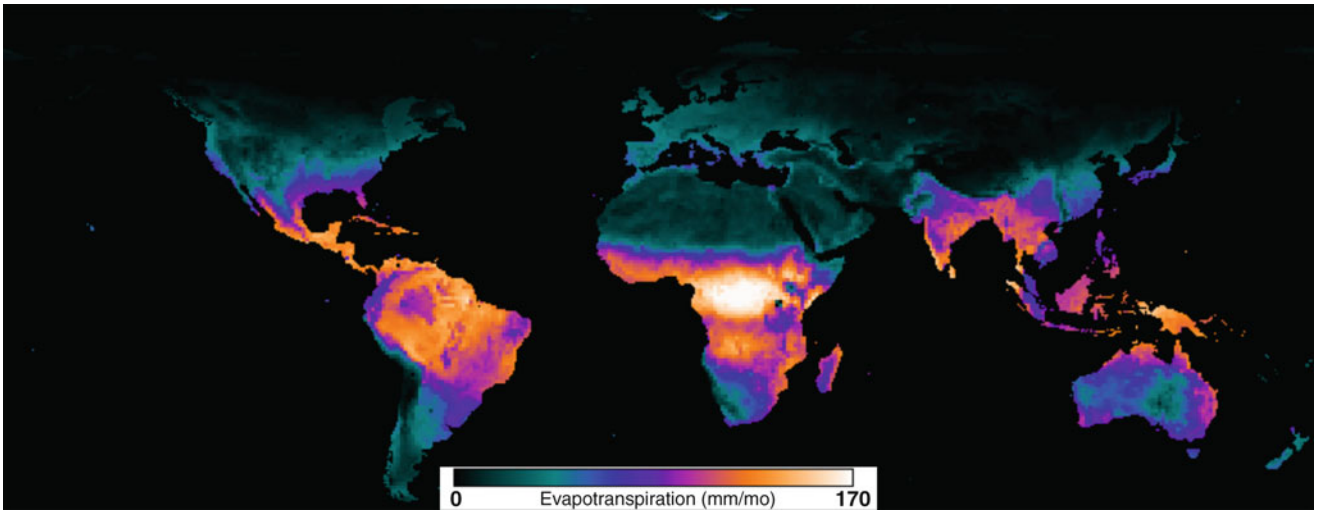

Land-Atmosphere Interactions, Evapotranspiration, Figure 1 Mean monthly ET for 2004 from the PT-JPL product.

biome-specific lookup table to parameterize the resistances. R_n, *VPD*, and air temperature (T_a; i.e., included in Δ) in MOD16 are derived from the NASA/GMAO Modern Era Retrospective Analysis (MERRA).

The PT-JPL product (Figure 1: Fisher et al., 2008) is based on the PET formulation of the Priestley-Taylor equation, which is a reduced version of the Penman-Monteith equation, eliminating the need to parameterize the stomatal and aerodynamic resistances, leaving only equilibrium evaporation multiplied by a constant (1.26) called the α coefficient:

$$PET = \alpha \frac{\Delta}{\Delta + \gamma} R_n \tag{4}$$

PET is reduced to AET using ecophysiological constraint functions (*f*-functions, unitless multipliers, 0–1) based on atmospheric moisture (*VPD* and relative humidity, *RH*) and vegetation indices (*NDVI* and *SAVI*):

$$ET = ET_s + ET_c + ET_i \tag{5}$$

$$ET_c = (1 - f_{wet}) f_g f_T f_M \alpha \frac{\Delta}{\Delta + \gamma} R_{nc} \tag{6}$$

$$ET_s = (f_{wet} + f_{SM})(1 - f_{wet})) \alpha \frac{\Delta}{\Delta + \gamma} (R_{nc} - G) \tag{7}$$

$$ET_i = f_{wet} \alpha \frac{\Delta}{\Delta + \gamma} R_{nc} \tag{8}$$

where ET_s, ET_c, and ET_i are evaporation from the soil, canopy, and intercepted water, respectively, each calculated explicitly. f_{wet} is relative surface wetness (RH^4), f_g is green canopy fraction (f_{APAR}/f_{IPAR}), f_T is a plant temperature constraint ($\exp(-((T_{max} - T_{opt})/T_{opt})^2)$), f_M is a plant moisture constraint ($f_{APAR}/f_{APARmax}$) and f_{SM} is a soil moisture constraint, (RH^{VPD}). f_{APAR} is absorbed photosynthetically active radiation (PAR), f_{IPAR} is intercepted PAR, T_{max} is maximum air temperature, T_{opt} is T_{max} at max($R_n T_{max} SAVI/VPD$), and G is the soil heat flux.

Land surface models/Earth system models

The most complex approach to estimating ET is through full Land Surface Models (LSMs) or Earth System Models (ESMs). These models are typically driven by meteorological data and aim to simulate all of the relevant biogeochemical processes and states governing the exchange of energy, water, and carbon throughout the entire land surface or complete Earth system, including ocean and atmosphere. Some of these models assimilate any relevant observation from both space and in situ to constrain the complexity of linkages and feedbacks. While the estimate of ET from LSMs and ESMs is subject to potentially greater uncertainty relative to the previously described approaches due to increased complexity and degrees of freedom, LSMs and ESMs allow more realistic feedbacks to and from ET given changes in the Earth system or climate (Mueller et al., 2011).

Summary

Remote sensing of ET is currently a high-level research and science priority, especially as ET is central to connecting the water, energy, and carbon cycles; a modulator of regional rainfall; a significant factor in flood and drought processes and models; the primary climatic predictor of biodiversity; and critical for the agricultural industry. In situ measurement of ET requires

cost-constraining equipment; as such, major international efforts, such as the Global Energy and Water Cycle Experiment (GEWEX), have focused on determination of ET from existing remote sensing assets (Jiménez et al., 2011; Vinukollu et al., 2011). The techniques described here provide an overview of how the scientific community estimates ET from remote sensing.

Acknowledgment

This research was carried out at the Jet Propulsion Laboratory, California Institute of Technology, under a contract with the NASA.

Bibliography

Baldocchi, D., et al., 2001. FLUXNET: a new tool to study the temporal and spatial variability of ecosystem-scale carbon dioxide, water vapor, and energy flux densities. *Bulletin of the American Meteorological Society*, **82**, 2415–2434.

Fisher, J. B., Tu, K., and Baldocchi, D. D., 2008. Global estimates of the land-atmosphere water flux based on monthly AVHRR and ISLSCP-II data, validated at 16 FLUXNET sites. *Remote Sensing of Environment*, **112**, 901–919.

Fisher, J. B., Whittaker, R. H., and Malhi, Y., 2011. ET come home: a critical evaluation of the use of evapotranspiration in geographical ecology. *Global Ecology and Biogeography*, **20**, 1–18.

Jiménez, C., et al., 2011. Global inter-comparison of 12 land surface heat flux estimates. *Journal of Geophysical Research*, **116**, 1–27, doi:10.1029/2010JD014545.

Jung, M., Reichstein, M., and Bondeau, A., 2009. Towards global empirical upscaling of FLUXNET eddy covariance observations: validation of a model tree ensemble approach using a biosphere model. *Biogeosciences*, **6**, 2001–2013.

Li, Z.-L., et al., 2009. A review of current methodologies for regional evapotranspiration estimation from remotely sensed data. *Sensors*, **9**, 3801–3853.

Mu, Q., Zhao, M., and Running, S. W., 2011. Improvements to a MODIS global terrestrial evapotranspiration algorithm. *Remote Sensing of Environment*, **111**, 519–536.

Mueller, B., et al., 2011. Evaluation of global observations-based evapotranspiration datasets and IPCC AR4 simulations. *Geophysical Research Letters*, **38**, 1–7, doi:10.1029/2010GL046230.

Vinukollu, R. K., Wood, E. F., Ferguson, C. R., and Fisher, J. B., 2011. Global estimates of evapotranspiration for climate studies using multi-sensor remote sensing data: evaluation of three process-based approaches. *Remote Sensing of Environment*, **115**, 801–823.

LANDSLIDES

Vernon H. Singhroy
Applications Development Section, Natural Resources Canada, Canada Centre for Remote Sensing, Ottawa, ON, Canada

Synonyms

Debris flow; Mass movement; Mudslide; Rock avalanche

Definition

Landslide is used to describe the downslope movement of soil and rock under the effects of gravity. In some cases, other terms such as mass movements and slope failure are used interchangeably with landslides. The most common triggers of landslides are earthquakes, heavy rains, thawing of frozen ground, river and coastal erosion, and frequent infrastructure and building development. Many types of landslides are usually associated with specific mechanics of slope failure and the properties and characteristics of failure type. Figure 1 shows a simple illustration of a rotational landslide which illustrates the commonly used labels for the parts of a landslide.

Introduction

Landslides are among one of the serious geological hazards which threaten and influence the socioeconomic conditions of many countries (Schuster, 1996). They are the manifestation of slope instability. An example of their destructive nature is shown in Figure 2. The La Conchita landslide in California killed ten persons. Geologists and engineers have long tried to identify the conditions of slope failure and mitigate their risk to infrastructure and populated areas.

There are various techniques used to map and evaluate landslides. Large-scale, stereo aerial photographs are one of these tools that have been extensively used in landslide investigations. Because of their three-dimensional capability, they provide essential geologic and geomorphic information necessary for landslide inventory mapping. Recently, there has been increasing uses of high-resolution satellite images (1–5 m) for various landslide investigations. The recent advances in radar interferometry are providing valuable insights in monitoring slow-moving landslides. The following section briefly discusses the uses of these techniques in landslide investigations.

Landslide mapping

Stereo aerial photographs are used extensively to produce landslide inventory maps. They allow the identification of geomorphic, geologic, and related land use features related to landslides (Mollard and Janes, 1993). Geological and geomorphologic units related to landslide inventories can be interpreted on the basis of morphological, textural, and structural characteristics using stereo aerial photos and high-resolution satellite images. Landslide inventory maps are usually published at various scales, such as national (1; 1,000,000), regional (1:100,000), medium (1:25,000–50,000), and large scales (>1:15,000).

For instance, detail inventory requires detail aerial photos and high-resolution satellite images to assist the interpreter to make conclusions on types and causes of the landslide. Recently, the high-resolution satellite Google images provided a cheap and valuable source of

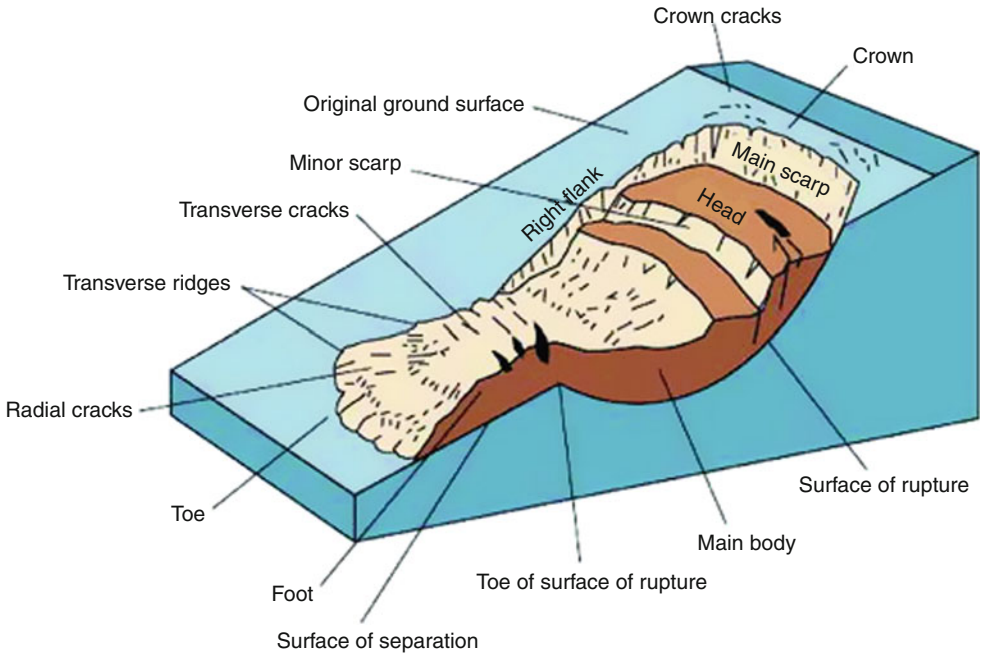

Landslides, Figure 1 Parts of a landslide (Modified from Varnes (1978), by Highland and Bobrowsky (2008)).

Landslides, Figure 2 This landslide occurred at La Conchita, California, USA, in 2005. Ten people were killed (USGS Photo).

locating landslides before and after the devastating earthquake in Haiti in January 2010 (Figure 3).

Other high-resolution optical systems (1–5 m) such as IKONOS, Quickbird, and IRS images and the stereo capability of SPOT 5 are useful for landslide recognition and related land use mapping. Whenever possible, the highest-resolution images should be used to identify and interpret the geomorphic and associated features shown in Figure 1. Large landslides are easily recognized from medium resolution 30 m Landsat TM images.

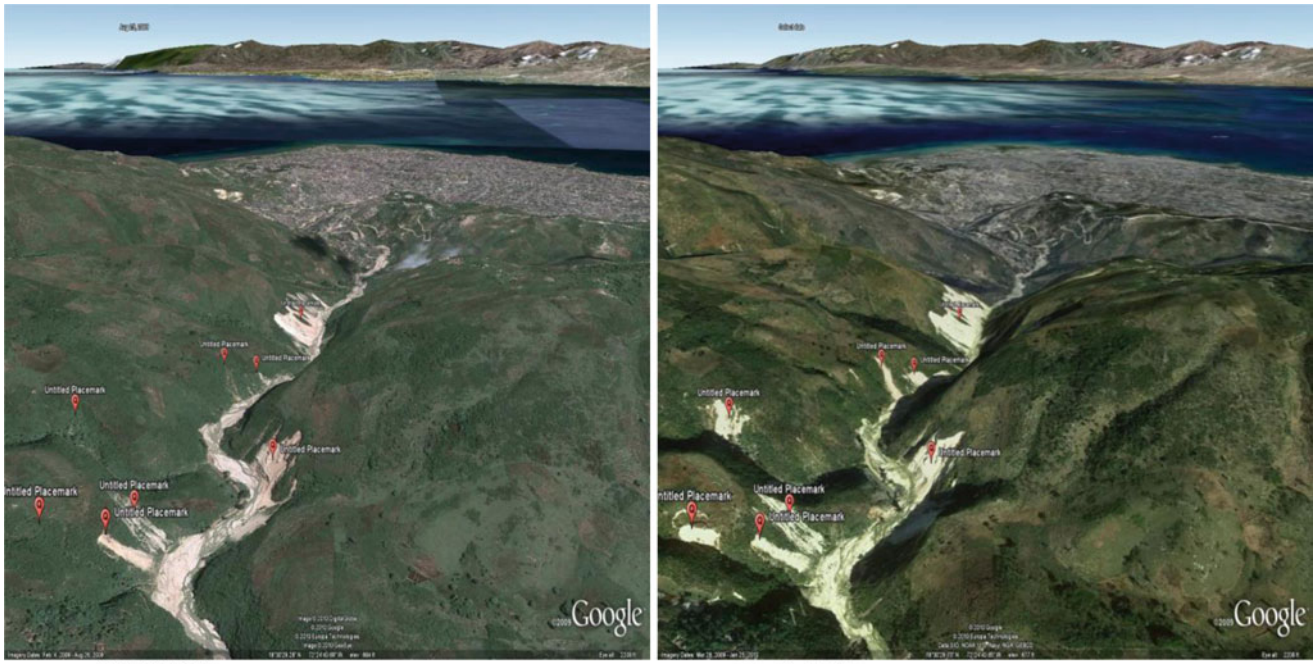

Landslides, Figure 3 Landslides near Port-au-Prince, before and after Haiti earthquake.

Recent research has shown that high-resolution stereo radar and optical images, combined with topographic and geological information, have assisted in mapping the geomorphic characteristics of deep-seated landslides needed to produce of landslide inventory maps (Singhroy et al., 1998; Singhroy, 2005). The multi-incidence angle, stereo, and high-resolution capabilities of the various radar satellites are particularly useful in providing terrain and geomorphic information needed to produce landslide inventory maps.

Currently, damage assessment related to landslides and other disasters in support of relief efforts uses aerial photography, videos, high-resolution satellite images, and ground checks.

Landslide monitoring using InSAR

Landslides usually resulted in extreme economic and societal costs, despite our increased understanding of the mechanisms of failure and large ground deformation. Current state of the art in real-time monitoring of active slopes developed for early warning of landslides is very expensive. Satellite radar interferometry is used increasingly to complement real-time monitoring such as GPS and in situ field measurements (Singhroy, 2008).

Interferometric Synthetic Aperture Radar (InSAR) techniques are being used to measure small millimeter displacement on slow-moving landslides. An interferometric image represents the phase differences between the backscatter signals in two SAR images obtained from similar positions in space. In case of spaceborne SAR, the images are acquired from repeat-pass orbits. The phase differences between two repeat-pass images result from topography and from changes in the line-of-sight distance (range) to the radar due to displacement of the surface or change in the atmospheric propagation path length. For a nonmoving target, the phase differences can be converted into a digital elevation map if very precise satellite orbit data are available.

Typical scales for SAR interferometry application to landslide movements are millimeters to centimeters per orbit cycle of the radar satellite. This orbit cycle can range from 44 days for ALOS and 10 days for TerraSAR-X. Constellation missions such as Cosmo-SkyMed, Sentinel, and RADARSAT constellation mission are reducing the orbits to 1–4 days.

It is clear that InSAR techniques can be used to monitor landslide motion under specific conditions, provided coherence is maintained over the respective orbit cycle. Using data pairs with short perpendicular baselines, short time intervals between acquisitions, and correcting for the effect of topography and atmospheric effects, reliable measurements of surface displacement can be achieved. The InSAR deformation maps provide linear motion at the line of site. Although this is very useful information, landslide motion is very complex with nonlinear vectors. Therefore, InSAR techniques do not provide the complete 3d motion

Vegetation decorrelates the radar signals. Therefore, stable coherent targets such as installed corner reflectors or man-made constructions such as houses, roads, and bridges are used to calculate the landslide motion. The uses of installed field corner reflectors are increasing on remote vegetated sites. Acquiring about 30 InSAR images on coherent targets over long periods are analyzed by a Permanent

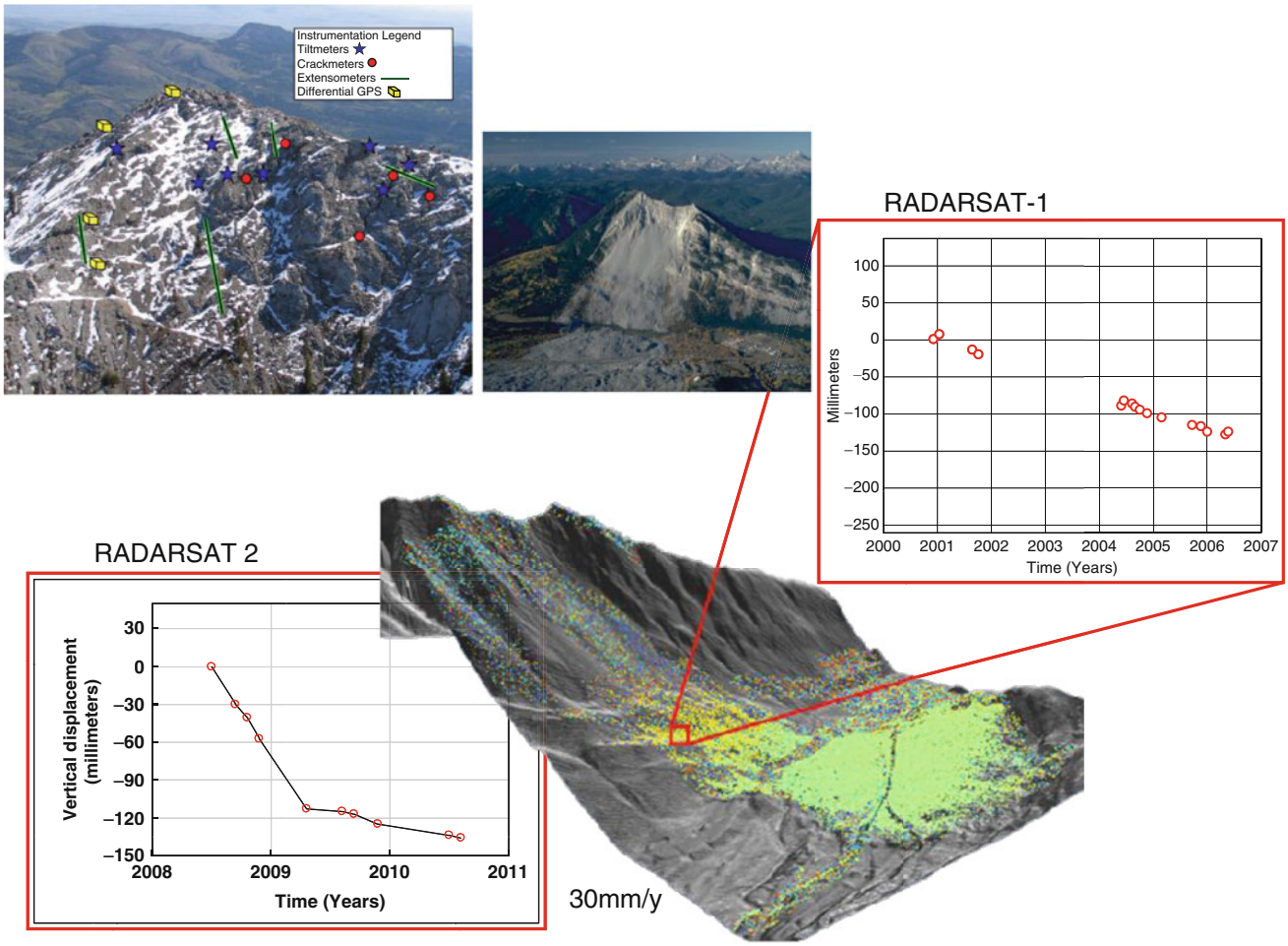

Landslides, Figure 4 Frank Slide, Canada: monitoring landslide motion from RADARSAT InSAR (2000–2010) (Modified from Mei et al. 2007).

Scatterer Technique PSInSAR™ developed by Ferretti et al. (2001). With the Permanent Scatterer Technique, the movement of small objects (down to about 1 m^2) can be monitored. This method has been applied to map subsidence and slow-moving landslides and many parts of the world.

The *Frank rock avalanche* is provided to demonstrate the capability of InSAR to monitor gradual motion on large rock avalanche in the Canadian Rockies. The Frank Slide, a 30 × 106 m^3 rock avalanche of Paleozoic limestone, occurred in April 1903 on the east face of Turtle Mountain in southern Alberta, Canada. Seventy fatalities were recorded. This slide is still active. Several factors contribute to this rock avalanche. These include the geological structure of the mountain, subsidence from coal mining at the toe of the mountain, blast-induced seismicity, above-average precipitation in years prior to the slide, and freeze-thaw cycles (Cruden and Hungr, 1996). GPS stations and several in situ monitors are installed to monitor post-slide activity at specific locations (Figure 4). Current InSAR monitoring is complementing the in situ measurements. The fact that the rock covering the rock avalanche is bare and dry leads to the high coherence and identification of more than 95 % of the coherent target monitoring targets for the Frank Slide area. Due to their great density and excellent coverage, the coherent target measurements of this area are a reliable reflection of current deformation pattern. The most recent InSAR results (Figure 4) have shown that during a period from April 2004 to October 2006, the foot of the eastern slope of Turtle Mountain, the ground surface above the coal mine, was found to subside at an average rate of about 3.1 mm per year supporting the speculation that underground coal mining triggered the Frank landslide (Mei et al., 2007).

The above examples show that satellite images are providing reliable complementary techniques to landslide mapping and monitoring, and therefore, its uses are increasing in landslide investigation and mitigation.

Bibliography

Cruden, D. M., and Hungr, O., 1996, 1986. The debris of Frank Slide and theories of rockslide-avalanche mobility. *Canadian Journal of Earth Sciences*, **23**, 425–432.

Ferretti, A., Prati, C., and Rocca, F., 2001. Permanent scatterers in SAR interferometry. *IEEE Transactions on Geoscience and Remote Sensing*, **39**, 8–20.

Highland, L. M., and Bobrowsky, P., 2008. *The Landslide Handbook – A Guide to Understanding Landslides*. Reston: U.S. Geological Survey Circular, Vol. 1325, p. 129.

Mei, S., Poncos, V., and Froese, C., 2007. *InSAR Mapping of Millimetre-scale Ground Deformation over Frank Slide, Turtle Mountain, Alberta*. Alberta Energy and Utilities Board, EUB/AGS Earth Science Report 2007, 1–62 pp.

Mollard, J. D., and Janes, J. R., 1993. *Airphoto Interpretation of the Canadian Landscape*. Ottawa: Energy, Mines and Resources, Canada, p. 415p.

Schuster, R. L., 1996. Socio- economic significance of landslides. In Turner, A. K., and Schuster, R. L. (eds.), *Landslides: Investigation and Mitigation*. Washington, DC: National Academy Press. Report 247, Transportation Research Board, NRC, pp. 12–35.

Singhroy, V., 2005. Remote sensing for landslide assessment: chapter 16. In Glade, T., Anderson, M., and Crozier, M. J. (eds.), *Landslides Hazard and Risk*. Chichester/Hoboken: Wiley, pp. 469–549.

Singhroy, V., 2008. Satellite remote sensing applications for landslide detection and monitoring (chap. 7). In Sassa, K., and Canuti, P. (eds.), *Landslide Disaster Risk Reduction*. Berlin: Springer, pp. 143–158.

Singhroy, V., Mattar, K. E., and Gray, A. L., 1998. Landslide characteristics in Canada using interferometric SAR and combined SAR and TM images. *Advances in Space Research*, **3**, 465–476.

Varnes, D. J., 1978. Slope movement, types and processes. In Schuster, R. L., and Krizek, R. J. (eds.), *Landslides-Analysis and Control*. Washington, DC: National Research Council. Transportation Research Board Special Report 176, pp. 11–23.

LAW OF REMOTE SENSING

Joanne Irene Gabrynowicz
National Center for Remote Sensing, Air, and Space Law, The University of Mississippi School of Law, Missisippi, MS, USA

Overview

All of the international space law began with the Declaration of Legal Principles Governing the Activities of States in the Exploration and Use of Outer Space (Declaration), adopted in 1962 by the United Nations General Assembly. National space laws, like that of the United States, were influenced by international space law and developed in tandem.

The Declaration is the foundation for the Treaty on Principles Governing the Activities of States in the Exploration and Use of Outer Space, including the Moon and Other Celestial Bodies (Outer Space Treaty). The Outer Space Treaty entered into force at the height of the Cold War on October 10, 1967. It contains fundamental space law principles that are directly applicable to remote sensing activities, such as all nations have the nonexclusive right to use space. In less than a decade, four more treaties followed, some of which also have legal principles applicable to remote sensing.

Legislative history in the United Nations

In 1970, Prof. A.A. Cocca of Argentina first introduced remote sensing as a specific legal topic in a paper to the Legal Subcommittee of the U.N. Committee on the Peaceful Uses of Outer Space (UNCOPUOS). In 1971, a Working Group was formed in the Legal Subcommittee to consider the paper, and in 1973, the Scientific and Technical Subcommittee of UNCOPUOS issued its first report containing a section on remote sensing. In 1974, the General Assembly adopted a resolution recommending that the LSC should consider the question of the legal implications of remote sensing of the Earth from space.

In 1975–1976, the first discussions concerning the legal implications of remote sensing began. Initially, the participating Nation-States organized themselves into three groups, or blocs: the Soviet Union/East Europe; the Group of 77 (G-77), consisting of developing nations in Africa, Asia, and Latin America; and the Western Group. The primary issues were whether or not sensing States had to obtain the consent of a sensed State prior to acquiring data from space or prior to distributing data to a third party. The Soviet Union and France submitted a proposal to require sensing States to obtain the prior consent of sensed States before data could be made available to other entities. The G-77 initially opposed both remote sensing itself and the distribution of data. The United States, then the only sensing state, advocated a free flow of data and therefore opposed prior constraints.

In 1975, the General Assembly recommended that the Legal Subcommittee continue consideration of remote sensing from space as a high priority. It specifically pointed to the use of remote sensing regarding the Earth's natural resources and environment. It also recommended drafting principles regarding points on which States agreed. The General Assembly noted that the Scientific and Technical Subcommittee had examined operational and experimental questions and now recommended that studies be conducted on organizational and financial matters. It also endorsed an international remote sensing training center for personnel from developing nations. In 1976, this work slowed down because the Soviet Union attempted to link some remote sensing issues to the developing Moon Treaty. By late 1976, progress was made on formulating some draft principles. The General Assembly noted in a resolution that the Legal Subcommittee formulated five draft principles and identified three new common elements identified by States.

Main issues

From 1977 to 1979, the Working Group focused on three main issues: whether or not "should" or "shall" ought to

be used in the principles, providing consultation and dispute resolution procedures, and the Soviet Union's proposal to limit image gathering to 50 m spatial resolution. Cold War politics drove the legal debate. A specific attempt to codify the 50 m limit was made on May 19, 1978, when Cuba, Czechoslovakia, the German Democratic Republic, Hungary, Mongolia, Poland, Romania, and the Union of Soviet Socialist Republics signed the Convention on Transfer and Use of Data of Remote Sensing of the Earth from Outer Space in Moscow. It provided that if a Contracting Party was in possession of data with resolution higher than 50 m, it was forbidden from making the data available to anyone without the explicit consent of the sensed State. This did not significantly influence the Legal Subcommittee negotiations. In a 1979 resolution, the General Assembly again recommended that the Legal Subcommittee continue work on the draft principles on a priority basis.

The evolution and use of the US *Landsat* system catalyzed addressing many general and specific remote sensing issues in legal terms. In 1982 and 1983, as a cost recovery method, the United States raised the access fee for a *Landsat* ground station from $200,000 (US) to $600,000 (US), and the cost of computer-compatible tapes increased. The United States announced its intention to commercialize the *Landsat* system. Identifying principles regarding data access, among others, became more pressing. In 1981, 1982, 1983, and 1984, the General Assembly adopted resolutions that noted each year's progress toward developing principles and continued to urge the Legal Subcommittee to develop the legal implications of remote sensing on a priority basis.

In 1984, the US Congress passed the Land Remote Sensing Commercialization Act (Commercialization Act). It adopted the nondiscriminatory access policy forged in the Legal Subcommittee and provided for a three-phased process to establish commercial remote sensing. The first phase was to award a contract for existing *Landsat* operations to a private sector operator. The second phase was to be a transition period in which both the government and the private sector would operate satellites, with government activities phasing out. The third phase was to be a fully private, commercial environment. The US contract award process had begun and the negotiators in the United Nations took note. Conversely, the United States needed to have the legitimacy of commercial remote sensing activities accepted. France was preparing to launch its first remote sensing satellite, *SPOT-1*, which it did in 1986. In 1984, France proposed alternate language for the draft data access principle, and negotiations on the remote sensing principles were revitalized.

In 1985, significant portions of the draft principles were still not agreed upon. According to at least one report, the Soviet Union/Eastern bloc did not participate in discussions of Article XII, the data access principle, out of concern that there would be no acceptable solutions for the G-77 nations. Some nations, including Mexico and Vietnam, believed there was insufficient time to consider the draft text. The General Assembly again adopted a resolution endorsing the Legal Subcommittee's work and added that it should finalize the draft set of principles. The Chair of the Working Group was Austria, and it offered an alternate text based on consultations regarding the French proposal. Discussions on the Austrian text were held. No changes were made in 1986. On December 3, 1986, The Principles Relating to Remote Sensing of the Earth from Outer Space (Principles) were adopted by the General Assembly.

The principles relating to remote sensing of the Earth from outer space

The Principles embody the view that Outer Space is a resource for all humanity and should be used for the general benefit of all nations. They encourage international cooperation and address access and distribution of data and information generated by national civilian remote sensing systems. Primary data are the raw data delivered in the form of electromagnetic signals, photographic film, magnetic tape, or any other means. Processed data are the products resulting from processing primary data, and analyzed information means information resulting from interpreting processed data. Remote sensing activities include operations, data collection, storage, processing, interpretation, and dissemination.

The Principles set a standard of international cooperation among sensing and sensed States while attempting to achieve a balance between their rights and interests. Needs of developing nations are given special regard. The Principles specifically promote protection of the Earth's environment and of humanity from natural disasters. States that possess remotely sensed information useful for averting harmful phenomena are required to disclose the information to concerned States. If the potential harm threatens people, the obligation to disclose requires promptness and extends to processed data and analyzed information.

The rights and responsibilities of sensed and sensing States are particularly addressed in Articles IV and XII. Article IV sets a legal standard for behavior among sensed and sensing States, and Article XII is a data dissemination statute. Together, they provide a fluid legal regime that obliges sensing States to avoid harm to sensed States and to provide them with access to primary data and processed data concerning their own territory on a nondiscriminatory basis. This was the compromise between terrestrial sovereignty and the freedom to use space. The legitimacy of space-based remote sensing was accepted by ensuring that a sensed State would have access to the imagery of its territory. Analyzed information available to sensing States is also to be available to the sensed States on the same basis and terms. In turn, sensed States are to meet reasonable cost terms and do not have access to analyzed information legally unavailable to the sensed States, for example, proprietary information.

The Principles were contained in the first major resolution to emerge from COPUOS in more than a decade and provide a foundation for the continued evolution of international remote sensing law. The question of whether or not the remote sensing principles ought to become a treaty continues to be raised in the COPUOS Legal Subcommittee.

US law: The oldest national remote sensing law

On October 28, 1992, the US Congress passed the Land Remote Sensing Policy Act of 1992 (Policy Act). It replaced the 1984 Commercialization Act. Congress adopted the nondiscriminatory access policy for second time. The Policy Act's focus is long-term remote sensing policy and its numerous facets. Specific matters addressed include program management, *Landsat 7* procurement, *Landsat 4* through *7* data policy, transfer of *Landsat 6* program responsibilities, regulatory authority and administration of public and private remote sensing systems, federal research and development, advanced technology demonstration, *Landsat 7* successor systems, data availability and archiving, and the continued prohibition of weather satellite commercialization. The legislation features a focus on the value of remote sensing in conducting global change research and other public sector applications, a recasting of remote sensing activities, and provisions for the future evolution of remote sensing policy. In 2008, efforts were made to replace the 1992 law with a new statute titled, the *National Land Imaging Program*. This bill was intended to embody the US new national remote sensing policy to implement a long-term operational land imaging program. It was not made into law.

New law and policy of remote sensing nations

India, the United Kingdom, and some other remote sensing nations have policies rather than laws. However, increasingly, major remote sensing nations are promulgating national laws. In 1999, Canada announced a policy that, in 2005, received Royal Assent and which came into force in April of 2007 as the *Remote Sensing Space Systems Act*. In 2007, the *German Act on Satellite Data Security* entered into force. These laws address the commercial availability of high-resolution imagery, and both seek to ensure national security interests within a commercial context. In 2008, Japan and France each passed a comprehensive national space law that includes sections on remote sensing. Court decisions in France, Germany, and the United States regarding the intellectual property and other aspects of remote sensing are also adding to the overall corpus of law.

Globalizing Earth observations

In the 1990s, the trend to internationalize Earth observation satellite operations began, and important new agreements were formulated. On November 19, 1998, the US National Oceanic and Atmospheric Administration and the European Organisation for the Exploitation of Meteorological Satellites entered into an agreement on a joint polar-orbiting operational system, and a second agreement was entered into on June 24, 2003. *The International Charter on Space and Major Disasters* became operational on November 1, 2000. Some nations, like Belgium, do not have indigenous remote sensing capabilities but, nonetheless, are developing national remote sensing laws because they are participating in remote sensing consortia. It is clear that remote sensing law will continue to develop.

Bibliography

Christol, C. Q., 1982. *The Modern International Law of Outer Space*. New York: Pergamon Press.

Gabrynowicz, J., 2002a. *The United Nations Principles Relating to Remote Sensing of the Earth from Space: A legislative History – Interviews of Members of the United States Delegation*. Oxford, MS: The National Center for Remote Sensing, Air, and Space Law. ISBN 0-9720432-1-7.

Gabrynowicz, J., 2002b. *Proceedings, The First International Conference on the State of Remote Sensing Law*. Oxford, MS: The National Center for Remote Sensing, Air, and Space Law. ISBN 0–9720432-3–3.

Gabrynowicz, J., 2005. The perils of landsat from grassroots to globalization: a comprehensive review of U.S. remote sensing law with a few thoughts for the future. *Chicago Journal of International Law*, **6**, 72.

Gabrynowicz, J., 2008. The second international conference on the state of remote sensing law. *Journal of Space Law*, **34**(1), ISSN 0095–7577 - 9720432–3–3, The National Center for Remote Sensing, Air, and Space Law: Oxford, MS.

Graham, J. F., and Gabrynowicz, J., 2002. *Landsat 7: Past, Present and Future*. Oxford, MS: The National Center for Remote Sensing, Air, and Space Law. ISBN 0-9720432-0-9.

The Land Remote Sensing Laws and Policies of National Governments: A Global Survey, The National Center for Remote Sensing, Air, and Space Law, Oxford, MS, 2007. Available from http://www.spacelaw.olemiss.edu/resources/pdfs/noaa.pdf. Last accessed 21 June 2012.

United Nations Office for Outer Space Affairs. *United Nations Office for Outer Space Affairs*, http://www.unoosa.org/oosa/en/SpaceLaw/index.html. Last accessed 21 June 2012.

LIDAR SYSTEMS

Robert Menzies
Jet Propulsion Laboratory, California Institute of Technology, Pasadena, CA, USA

Synonyms

Ladar; Laser radar

Definitions

Lidar. LIght Detection And Ranging
Ladar. LAser Detection And Ranging

Introduction

A lidar system in the strictly defined sense of the acronym measures range to a "target" that provides a signal that can be detected. Thus, the lidar system includes both a transmitter and a receiver. Ranging is accomplished using time-of-flight methods. The target can be a "hard" target that is essentially opaque to the lidar wavelength, not allowing measureable penetration beyond its range, or a "diffuse" scattering medium that allows penetration and range gating. Examples of the former are the surfaces of the Earth and other planets, or man-made objects. Examples of the latter are atmospheric aerosols and gases. In reality, these are terms that are commonly used but do not have strict, universally accepted definitions. In fact, the term "lidar" itself is commonly applied to systems that contain transmitters and receivers but do not have inherent range measurement capability. The lidar community is inclusive in this regard.

Following David Tratt's introductory entry ("Emerging Technologies: Lidar"), which describes lidar basics and various classes or categories of lidar, we provide here a summary of the current capabilities in these various lidar applications areas. Our lidar categories are altimetry and mapping systems, backscatter systems, Doppler systems, and differential absorption systems. Comments on emerging technologies and methods are included. Lidar/ladar applications cover a wide range of activities and interests. The 3D imaging applications are a growth area with strong support from the defense community. System developments in this area are included only in brief overview mode. The balance in this entry is tilted more toward systems developed for scientific investigations.

Altimetry and mapping systems

Laser altimetry is relatively mature, with heritage in aircraft instruments, followed by Earth-orbiting, Mars-orbiting, and Lunar-orbiting systems. The early altimeter/mapping instruments used a form of threshold detection to trigger a circuit that enabled range measurement to a "first return" scattering surface. The implementation of fast waveform recovery, or multistop detection circuits, increases data rates but provides structure information in the line-of-sight dimension. The Geoscience Laser Altimeter System (GLAS) on the Earth-orbiting ICESat (Abshire et al., 2005) provided structure detail in the time domain, a capability that is essential for future use of laser 3D mappers in obtaining global estimates of biomass. High-resolution 3D imaging with very high depth resolution (~1 mm) can be achieved at km distances using fiber lasers and high bandwidth waveform encoding and decoding techniques (Buck et al., 2007). The current and next-generation systems combine multi-beam transmitter patterns with structural detail in the range dimension. The laser altimetric observational method provides line-of-sight detail that complements radar methods as well as higher spatial resolution in the cross dimensions. Spatial coverage is a challenge, however. The advent of avalanche photodiode (APD) arrays and photon-counting receivers (e.g., Aull et al., 2002; Albota et al., 2002), combined with optical methods for simultaneous transmission of multiple beams, have greatly increased the mapping efficiencies of airborne and space systems. The use of statistical methods in a photon-counting mode has allowed the use of compact, high pulse-repetition frequency (prf), low pulse energy laser transmitters in various imaging and mapping systems (Degnan et al., 2008; Steinvall et al., 2008). The Lunar Orbiter Laser Altimeter (LOLA) instrument, scheduled to launched in June, 2009, uses a Diffractive Optical Element (DOE) to produce a 5-beam pattern for provision of more spatial coverage than with prior space laser altimeters (Ramos-Izquierdo et al., 2009; Smith et al., 2010). The DOEs have found use in various airborne laser 3D mappers.

An alternative to the use of scanners or elements such as DOEs, matched with APD arrays, is a flash lidar/ladar. The images in this type of system record the intensity reflected by the scene when flood-illuminated by the laser transmitter pulse. The laser transmitter irradiates the entire field of view of the receiver camera pixel array, and each pulse generates an entire frame of data (Stettner et al., 2005). The array elements are high-speed detectors that are periodically sampled in time at nanosecond timescales. The advances in hybridizing the focal planes with silicon CMOS read-out integrated circuits (ROICs), utilizing steady improvements in high-speed circuitry, provide the potential for growth with this approach. Laser sources can include semiconductor lasers and fiber lasers mated to power amplifiers.

Backscatter lidars

Here we include elastic backscatter lidars and various types of inelastic backscatter lidars (e.g., Raman, fluorescence). The emphasis is on atmospheric studies using these systems. The intensity or energy in the return signal is important with backscatter lidar measurements. Some method of calibration and/or normalization must be used in order to turn the data into useful observations. In the visible, the molecular density, if known sufficiently well, can be used to provide a Rayleigh backscatter intensity that effectively calibrates at least the range dependence of the lidar efficiency factor, or the efficiency factor itself at a particular atmospheric altitude where particle scattering is assumed negligible. This is not a viable technique at longer wavelengths in the infrared, due to the rapid decrease of the Rayleigh scattering cross section with increasing wavelength.

Backscatter lidars for cloud and aerosol studies date back to the early years of lidar, when ground-based lidars operating at visible wavelengths probed the stratospheric aerosol layers (e.g., Fiocco and Grams, 1964). The first Earth-orbiting lidar used for atmospheric studies was an elastic backscatter lidar (LITE, launched in 1994). GLAS operated both as an altimeter and an atmospheric lidar

(Spinhirne et al., 2005). Currently the CALIPSO lidar is in Earth orbit, being used for cloud and aerosol studies. The CALIPSO transmitter is a diode-array pumped Nd: YAG laser, by far the most commonly used in backscatter lidars. A wide dynamic range of pulse energies and pulse-repetition frequencies are available in this laser medium. The compact micropulse lidars, which emit pulses in the micro-Joule range, are deployed around the globe in networks such as the MPLNET (Micropulse Lidar Network) (Campbell et al., 2008). Cloud and aerosol detection, characterization, and monitoring algorithms continue to improve for these compact lidars, making them more useful for deployment. The underlying technologies are robust. The vertical profiling capabilities of these lidars cannot be duplicated with passive instruments. Recently, a compact backscatter lidar was deployed on the surface of Mars as part of the Phoenix mission (Whiteway et al., 2008).

A variant of the elastic backscatter lidar that is taking center stage in current and future atmospheric investigations is the High Spectral Resolution Lidar or HSRL. Although Doppler lidars are the ultimate high spectral resolution lidars, the term "HSRL" is commonly used in the lidar community to refer to a system that can separate the molecular Rayleigh backscatter signal from the aerosol backscatter signal. This obviates the need to assume a "lidar ratio" (i.e., aerosol extinction-to-backscatter ratio) when interpreting the range-dependent backscatter signals to deduce aerosol optical properties, thereby achieving more robust estimates of aerosol extinction coefficients. A progression in HSRL implementation has gone from early 1980s laser technology such as fragile dye laser systems (Shipley et al., 1983) to more robust solid-state lasers (Grund and Eloranta, 1991). Iodine vapor filters offer simplicity compared with the etalon filters in the HSRL receiver (Hair et al., 2001). More recently, airborne HSRL has been developed, and measurement results have been reported (Hair et al., 2008). The next-generation Earth-orbiting backscatter lidar for cloud and aerosol studies will likely be an HSRL. In fact, the European Space Agency's Atmospheric Laser Doppler Instrument (ALADIN), a Doppler lidar in the Atmospheric Dynamics Mission (ADM) with atmospheric wind field measurements as its primary objective, is fundamentally an HSRL and will be used for investigations of aerosol optical properties (Ansmann et al., 2007) (see www.esa.int for further information).

Resonance fluorescence lidars have been in use for decades to study dynamics and thermal properties of the middle atmosphere, particularly the mesosphere. Lidars built to measure alkalis in the upper mesosphere were also used as Rayleigh backscatter lidars to measure density and temperature profiles in the stratosphere and mesosphere (Hauchecorne and Chanin, 1980). Developments in solid-state laser technology and injection seeding methods have resulted in systems that are more amenable to transportation and operation at remote sites (e.g., She et al., 2007). Systems that interact with a variety of metals in addition to sodium and the other alkalis are now in development for investigations over a wider range of altitudes (Gardner, 2004).

Raman lidars are now commonly used for water vapor profiling and for characterizing the optical and microphysical properties of atmospheric aerosol. The latter method was described 20 years ago (Ansmann et al., 1990) and has continued to evolve into systems that are being used for characterization of major dust plumes that are transported long distances (e.g., Asian dust, Saharan dust) and for calibration/validation exercises (Mona et al., 2007). The former method has a long history and has slowly evolved with the use of improved techniques for minimizing background light, improved algorithms, and improved understanding of sources of bias. The use of Raman lidar for water vapor profiling in the lower atmosphere continues to gain credibility as the level of accuracy continues to improve (Adam and Venable, 2007; Leblanc and McDermid, 2008).

Doppler lidars

The atmospheric gas molecules and aerosol particles are in bulk motion in the dynamic atmosphere, and backscattering of laser radiation from the molecules and aerosol particles produces Doppler shifts in frequency. Doppler lidars detect these frequency shifts to deduce wind profiles. Two types of Doppler lidar have received attention over the years: direct detection and coherent detection lidars.

The coherent detection lidar is more sensitive and less difficult to implement at relatively longer wavelengths in the infrared, particularly at wavelengths longer than 1.5 μm, the so-called eye-safe region. The ultrahigh spectral resolution that is inherent with these systems makes coherent detection suitable for measuring Doppler-shifted backscatter from the atmospheric aerosol particles. The signal processing has similarities with Doppler radar. The use of rare-earth-doped solid-state laser technologies in the 2 μm wavelength region has been a popular choice for compact coherent detection systems. An example is the NOAA shipborne lidar, which has been used in many field campaigns (Tucker et al., 2009). Airborne systems date back to the mid-1980s when carbon dioxide gas laser transmitters were used (Bilbro et al., 1986). More recent, much more compact systems have also been deployed for measuring wind profiles with high spatial resolution (Hannon et al., 1999). Both the rare-earth-ion-doped solid-state crystal laser technology at 2 μm and the fiber laser technology developed primarily by the telecom industry have been employed in recent ground-based coherent Doppler lidars stationed at airports for airport safety enhancements. These lidar systems are being used for both wake vortex monitoring (e.g., Kopp et al., 2004) and wind shear detection and warning (e.g., Shun and Chan, 2008). Fiber laser

technologies are being incorporated into current and future systems.

Direct detection lidar is the appropriate choice for regions of the atmosphere containing very low aerosol particle concentration in the size range that is useful for optical scattering. The predominant scattering is molecular Rayleigh scattering. An early example was the use of direct detection Rayleigh lidar, modified with the incorporation of twin Fabry-Pérot interferometer filters in the receiver, for measurements of horizontal winds in the middle atmosphere (Chanin et al., 1989). An airborne direct detection Doppler lidar was developed, for tropospheric wind field measurements (Gentry et al., 2007). It is designed for autonomous operation on a high-altitude aircraft. The European Space Agency's ALADIN lidar is planned for launch in 2010, as the centerpiece instrument in the Atmospheric Dynamics Mission (ADM). ALADIN uses solid-state Nd: YAG laser transmitter technology, frequency-tripled to the 355 nm near-UV wavelength. It contains two receivers, one for the narrow-band Mie scattered radiation from the atmospheric aerosol particles (employing a multichannel Fizeau interferometer) and the other for the Rayleigh scattered radiation from the molecules (employing a double-edge Fabry-Pérot etalon). Accumulation CCD's are used in both receivers (see www.esa.int for further information).

Differential absorption lidars

Differential absorption lidars require typically two carefully selected closely spaced transmit wavelengths and a laser transmitter subsystem that has either discrete or continuous tenability in the desired spectral region to interact with the species of interest. Early systems used dye lasers or nonlinear optics such as optical parametric oscillators to provide tunability. Atmospheric ozone and water vapor have been favorite measurement subjects for decades. More recent systems rely on solid-state laser technologies and modern techniques for generating tunable single-mode radiation with high spectral purity. Airborne systems have progressed in sophistication, with corresponding reductions in mass and dimensions as well. The LASE (Lidar Atmospheric Sensing Experiment) system was demonstrated in the 1990s as an autonomous operation water vapor differential absorption lidar on the high-altitude ER-2 aircraft (Browell et al., 1997). Currently, intercomparison campaigns involving multiple airborne water vapor systems with different designs are being planned and implemented in order to better understand the accuracies of measurement and quantify biases that might exist (Behrendt et al., 2007). Results to date show that measurement accuracies are in good agreement with expectations.

Currently, a major challenge for differential absorption lidar is the measurement of atmospheric CO_2. Measurements with very high accuracy over regional to global scales would improve understanding of fluxes between atmosphere, land surface, and ocean surface. The influence that increasing carbon dioxide mixing ratio has on climate change has spurred an interest in applying both passive and active remote sensing techniques to address this question. Desired mixing ratio accuracy levels of better than 1 % place great demands on a differential absorption lidar system itself and require the minimization of errors due to imperfect knowledge of the relevant atmospheric parameters (Menzies and Tratt, 2003; Ehret et al., 2008). Demonstrations of CO_2 mixing ratio measurement capability using ground-based, coherent detection systems have been reported (Gibert et al., 2008; Koch et al., 2008). Airborne systems are now being tested in flight campaigns, using both the solid-state 2 μm laser technology and the 1.6 μm fiber laser technology (Abshire et al., 2010; Spiers, et al., 2011). Studies of Earth-orbiting lidar systems for CO_2 measurements are being conducted under the sponsorship of European, US, and Japanese space agencies (ESA, NASA, and JAXA respectively).

Summary

Using an unofficial taxonomy of lidar systems, selected highlights of recent developments and future plans have been provided. Generally speaking, the future applications for altimetry and three-dimensional mapping will motivate increases in coverage within a given available time frame. This will most likely come from increases in total laser transmitter output power, along with optical technology. In other lidar application areas, engineering advances will be critical. For example, advances in compactness, electrical power efficiency, autonomy, and reliability will be essential for further use in hazard detection and monitoring, as well as expansion of regional and global networks for weather, climate, atmospheric composition, and environmental monitoring. Atmospheric greenhouse gas measurements, on a global scale, present high-precision measurement challenges. Nearly 50 years after the first demonstration of the laser, many lidar system applications are still driven by laser technology advances. For example, many applications still await the development of a wider range of laser sources in infrared spectral regions that are presently underutilized. The advent of the quantum cascade laser and other "bandgap-engineered" semiconductor laser technologies, as well as fiber laser/amplifier technologies, are good examples of continuing laser technology advances.

Acknowledgment

This research was carried out at the Jet Propulsion Laboratory, California Institute of Technology, under a contract with the NASA.

Bibliography

Abshire, J. B., Graham, H. R., Allan, R., Weaver, C. J., Mao, J., Sun, X., Hasselbrack, W. E., Kawa, S. R., and Biraud, S.,

2010. Pulsed airborne lidar measurements of atmospheric CO_2 column absorption. *Tellus*, **62B**, 770–783.

Abshire, J. B., Sun, X., Riris, H., Sirota, J. M., McGarry, J. F., Palm, S., Yi, D., and Liiva, P., 2005. Geoscience laser altimeter system (GLAS) on the ICESat mission: on-orbit measurement performance. *Geophysical Research Letters*, **32**, L21S02, doi:10.1029/2005GL024028.

Adam, M., and Venable, D., 2007. Systematic distortions in water vapor mixing ratio and aerosol scattering ratio from a Raman lidar. In *Proceedings of SPIE*, Vol. 6750, doi:10.1117/12.738205.

Albota, M. A., Heinrichs, R. M., Kocher, D. G., Fouche, D. G., Player, B. E., O'Brien, M. E., Aull, B. F., Zayhowski, J. J., Mooney, J., Willard, B. C., and Carlson, R. R., 2002. Three-dimensional imaging laser radar with a photon-counting avalanche photodiode array and microchip laser. *Applied Optics*, **41**, 7671, doi:10.1364/AO.41.007671.

Ansmann, A., Riebesell, M., and Weitkakmp, C., 1990. Measurements of atmospheric aerosol extinction profiles with a Raman lidar. *Optics Letters*, **15**, 746–748.

Ansmann, A., Wandinger, U., Le Rille, O., Lajas, D., and Straume, A. G., 2007. Particle backscatter and extinction profiling with the spaceborne high-spectral-resolution Doppler lidar ALADIN: methodology and simulations. *Applied Optics*, **46**, 6606–6622.

Aull, B. F., Loomis, A. H., Young, D. J., Heinrichs, R. M., Felton, B. J., Daniels, P. J., and Landers, D. J., 2002. Geiger-mode avalanche photodiodes for three-dimensional imaging. *Lincoln Laboratory Journal*, **13**, 335–343.

Behrendt, A., Wulfmeyer, V., Kiemle, C., Ehret, G., Flamant, C., Schaberl, T., Bauer, H.-S., Kiio, S., Ismail, S., Ferrare, R., Browell, E. V., and Whiteman, D. N., 2007. Intercomparison of water vapor data measured with lidar during IHOP_2002. Part II: airborne-to-airborne systems. *Journal of Atmospheric and Oceanic Technology*, **24**, 22–39, doi:10.1175/JTECH1925.1.

Bilbro, J. W., DiMarzio, C. A., Fitzjarrald, D. E., Johnson, S. C., and Jones, W. D., 1986. Airborne Doppler lidar measurements. *Applied Optics*, **25**, 3952, doi:10.1364/AO.25.003952.

Browell, E. V., Ismail, S., Hall, W. M., Moore, A. S., Jr., Kooi, S. A., Brackett, V. G., Clayton, M. B., Barrick, J. D. W., Schmidlin, F. J., Higdon, N. S., Melfi, S. H., and Whiteman, D. N., 1997. LASE validation experiment. In Ansmann, A., Neuber, R., Rairoux, P., and Wandinger, U. (eds.), *Advances in Atmospheric Remote Sensing with Lidar*. Berlin: Springer, pp. 289–295.

Buck, J., Malm, A., Zakel, A., Krause, G., and Tiemann, B., 2007. High-resolution 3D coherent laser radar imaging. In *Proceedings of SPIE*, Vol. 6550, doi:10-1117/12.719483.

Campbell, J. R., Sassen, K., and Welton, E. J., 2008. Elevated cloud and aerosol layer retrievals from micropulse lidar signal profiles. *Journal of Atmospheric and Oceanic Technology*, **25**, 685–700, doi:10.1175/2007JTECHA1034.1.

Chanin, M. L., Garnier, A., Hauchecorne, A., and Porteneuve, J., 1989. A Doppler lidar for measuring winds in the middle atmosphere. *Geophysical Research Letters*, **16**, 1273–1276.

Degnan, J., Machan, R., Leventhal, E., Lawrence, D., Jodor, G., and Field, C., 2008. In-flight performance of a second-generation, photon counting, 3D imaging lidar. In *Proceedings of SPIE*, Vol. 6950, Laser Radar Technology and Applications XIII, doi:10-1117/12.784759.

Durand, Y., Chinal, E., Endemann, M., Meynart, R., Reitebuch, O., and Treichel, R., 2006. ALADIN airborne demonstrator: a Doppler wind lidar to prepare ESA's ADM-Aeolus Explorer mission. In *Proceedings of SPIE*, Vol. 6296, 62961D, doi:10.1117/12.680958.

Ehret, G., Kiemle, C., Wirth, M., Amediek, A., Fix, A., and Houweling, S., 2008. Space-borne remote sensing of CO2, CH4, and N2O by integrated path differential absorption lidar: a sensitivity analysis. *Applied Physics B*, **90**, 593–608, doi:10.1007/s00340-007-2892-3.

Esselborn, M., Wirth, M., Fix, A., Tesche, M., and Ehret, G., 2008. Airborne high spectral resolution lidar for measuring aerosol extinction and backscatter coefficients. *Applied Optics*, **47**, 346–358.

Fiocco, G., and Grams, G., 1964. Observation of the aerosol layer at 20 km by optical radar. *Journal of Atmospheric Science*, **21**, 323–324.

Gardner, C. S., 2004. Performance capabilities of middle-atmosphere temperature lidars: comparison of Na, Fe, K, Ca, Ca+, and Rayleigh systems. *Applied Optics*, **43**, 4941–4956.

Gentry, B., McGill, M., Schwemmer, G., Hardesty, M., Brewer, A., Wilkerson, T., Atlas, R., Sirota, M., Lindemann, S., and Hovis, F., 2007. Development of an airborne molecular direct detection Doppler lidar for tropospheric wind profiling. In *Proceedings of SPIE*, Vol. 6681, doi:10.1117/12.739379.

Gibert, F., Flamant, P. H., Cuesta, J., and Bruneau, D., 2008. Vertical 2-μm heterodyne differential absorption lidar measurements of mean CO2 mixing ratio in the troposphere. *Journal of Atmospheric and Oceanic Technology*, **25**, 1477–1497, doi:10.1175/2008JTECHA1070.1.

Grund, C. J., and Eloranta, E. W., 1991. University of Wisconsin high spectral resolution lidar. *Optical Engineering*, **30**, 6–12.

Hair, J. W., Caldwell, L. M., Krueger, D. A., and She, C.-Y., 2001. High-spectral-resolution lidar with iodine-vapor filters: measurements of atmospheric-state and aerosol profiles. *Applied Optics*, **40**, 5280–5294.

Hair, J. W., Hostetler, C. A., Cook, A. L., Harper, D. B., Ferrare, R. A., Mack, T. L., Welch, W., Ramos-Izquierdo, L., and Hovis, F. E., 2008. Airborne high spectral resolution lidar for profiling aerosol optical properties. *Applied Optics*, **47**, 6734–6752.

Hannon, S. M., Bagley, H. R., and Bogue, R. K., 1999. Airborne Doppler lidar turbulence detection: ACLAIM flight test results. In *Proceedings of SPIE*, Vol. 3707, 234, doi:10.1117/12.351378.

Hauchecorne, A., and Chanin, M.-L., 1980. Density and temperature profiles obtained by lidar between 35 and 70 km. *Geophysical Research Letters*, **7**, 565–568.

Koch, G. J., Petros, M., Barnes, B., Beyon, J. Y., Amzajerdian, F., Yu, J., Kavaya, M. J., and Singh, U. N., 2004. Validar: a testbed for advanced 2-micron Doppler lidar. In *Proceedings of SPIE*, Vol. 5412, pp. 87–98, doi:10.1117/12.542116.

Koch, G. J., Beyon, J. Y., Gibert, F., Bernes, B. W., Ismail, S., Petros, M., Petzar, P. J., Yu, J., Modlin, E. A., Davis, K. J., and Singh, U. N., 2008. Side-line tunable laser transmitter for differential absorption lidar measurements of CO2: design and application to atmospheric measurements. *Applied Optics*, **47**, 944–956.

Kopp, F., Rahm, S., and Smalikho, I. M., 2004. Characterization of aircraft wake vortices by 2-μm pulsed Doppler lidar. *Journal Atmospheric and Oceanic Technology*, **21**, 194–206.

Leblanc, T., and McDermid, I. S., 2008. Accuracy of Raman lidar water vapor calibration and its applicability to long-term measurements. *Applied Optics*, **47**, 5592–5603.

Menzies, R. T., and Tratt, D. M., 2003. Differential laser absorption spectrometry for global profiling of tropospheric carbon dioxide: selection of optimum sounding frequencies for high-precision measurements. *Applied Optics*, **42**, 6569, doi:10.1364/AO.42.006569.

Mona, L., Amodeo, A., D'Amico, G., and Pappalardo, G., 2007. First comparisons between CNR-IAMM multi-wavelength Raman lidar measurements and CALIPSO measurements. In *Proceedings of the SPIE*, Vol. 6750, 675010, doi:10.1117/12.738011.

Ramos-Izquierdo, L., Scott, V. S., Connelly, J., Schmidt, S., Mamakos, W., Guzek, J., Peters, C., Liiva, P., Rodriguez, M., Cavanaugh, H., and Riris, H., 2009. Optical system design and integration of the lunar orbiter laser altimeter. *Applied Optics*, **44**, 3035–3049, doi:10.1364/AO.44.007621.

She, C. Y., Vance, J. D., Kawahara, T. D., Williams, B. P., and Wu, Q., 2007. A proposed all-solid-state transportable narrowband sodium lidar for mesopause region temperature and horizontal wind measurement. *Canadian Journal of Physics*, **85**, 111–118.

Shipley, S. T., Tracy, D. H., Eloranta, E. W., Trauger, J. T., Sroga, J. T., Roesler, F. L., and Weinman, J. A., 1983. High spectral resolution lidar to measure optical scattering properties of atmospheric aerosols. 1: theory and instrumentation. *Applied Optics*, **22**, 3716–3724.

Shun, C. M., and Chan, P. W., 2008. Applications of an infrared Doppler lidar in detection of wind shear. *Journal of Atmospheric and Oceanic Technology*, **25**, 637–655, doi:10.1175/2007JTECHA1057.1.

Smith, D. E., Zuber, M. T., Neumann, G. A., Lemoine, F. G., Mazarico, E., Torrence, M. H., McGarry, J. F., Rowlands, D. D., Head, III, J. W., Duxbury, T. H., Aharonson, O., Lucey, P. G., Robinson, M. S., Barnouin, O. S., Cavanaugh, J. F., Sun, X., Liiva, P., Mao, D., Smith, J. C., and Bartels, A. E., 2010. Initial observations from the Lunar Orbiter Laser Altimeter (LOLA). *Geophysical Research Letters*, **37**, L18204, doi:10.1029/2010gl043751.

Spiers, G. D., Menzies, R. T., Jacob, J., Christensen, L. E., Phillips, M. W., Choi, Y., and Browell, E. V., 2011. Atmospheric CO_2 measurements with a 2 μm airborne laser absorption spectrometer employing coherent detection. *Applied Optics*, **50**(14).

Spinhirne, J. D., Palm, S. P., Hart, W. D., Hlavka, D. L., and Welton, E. J., 2005. Cloud and aerosol measurements from GLAS: overview and initial results. *Geophysical Research Letters*, **32**, L22S03, doi:10.1029/2005GL023507.

Steinvall, O., Sjoqvist, L., Henriksson, M., and Jonsson, P., 2008. High resolution ladar using time-correlated single-photon counting. In *Proceedings of SPIE*, Vol. 6950, doi:10.1117/12.778323.

Stettner, R., Bailey, H., and Silverman, S., 2005. Large format time-of-flight focal plane detector development. In *Proceedings of SPIE*, Vol. 5791, pp. 288–292.

Tucker, S. C., Brewer, W. A., Banta, R. M., Senff, C. J., Sandverg, S. P., Law, D. C., Weickmann, A. M., and Hardesty, R. M., 2009. Doppler lidar estimation of mixing height using turbulence, shear, and aerosol profiles. *Journal of Atmospheric and Oceanic Technology*, **26**, 673–688, doi:10.1175/2008JTECHA1157.1.

Werner, C., Flamant, P. H., Reitebuch, O., Köpp, F., Streicher, J., Rahm, S., Nagel, E., Klier, M., and Herrmann, H., 2001. Wind infrared Doppler lidar instrument. *Optical Engineering*, **40**, 115, doi:10.1117/1.1335530.

Whiteway, J., Daly, M., Carswell, A., Duck, T., Dickinson, C., Komguem, L., and Cook, C., 2008. Lidar on the Phoenix mission to Mars. *Journal of Geophysical Research*, **113**, E00A08, doi:10.1029/2007JE003002.

Cross-references

Cryosphere, Measurements and Applications
Ocean, Measurements and Applications
Optical/Infrared, Atmospheric Absorption/Transmission, and Media Spectral Properties
Optical/Infrared, Radiative Transfer
Optical/Infrared, Scattering by Aerosols and Hydrometeors

LIGHTNING

Rachel I. Albrecht[1], Daniel J. Cecil[2] and Steven J. Goodman[3]
[1]Divisão de Satélites e Sistemas Ambientais (DSA/CPTEC), Instituto Nacional de Pesquisas Espaciais (INPE), Cachoeira Paulista, SP, Brazil
[2]Marshall Space Flight Center (MSFC), National Aeronautics and Space Administration (NASA), Huntsville, AL, USA
[3]National Environmental Satellite, Data, and Information Service (NESDIS), National Oceanic and Atmospheric Administration (NOAA), Silver Spring, MD, USA

Synonyms

Cloud flash; Ground flash

Definition

Lightning or *lightning discharge*. A series of transient and multiple electrical breakdown pulses producing high-current channels (Uman, 1987).

Lightning flash. A luminous manifestation accompanying a sudden electrical discharge which takes place from or inside a cloud or, less often, from high structures on the ground or from mountains (WMO, 2011).

Introduction

A lightning flash is a noncontinuous multi-scale physical process that ranges from the initial breakdown of air to the actual discharge propagation in discrete steps that can occur from cloud to ground (CG) or inside the clouds, i.e., intracloud (IC). In the case of CG lightning, the lightning channel formation is led by *stepped leaders* (that creates a conducting path between charge centers) and then followed by one or multiple *return strokes* that traverse the channel moving electric charges and neutralizing the leaders (Rakov and Uman, 2003). These series of return strokes are the lightning flash, and each stroke is guided by the *dart leaders* that propagate downward on the track of a preceding return stroke. CG flashes are also classified by the polarity of lowered charge: negative and positive. Negative flashes are more common and exhibit several return strokes, while positive flashes have a single or very few return strokes, but higher current than the negative ones. These processes occur too rapidly for the human eye to distinguish, and the flash appears as a single channel lasting for less than a second. Lightning detection networks typically look for the electric field changes associated with such processes. In the case of IC lightning, *recoil streamers* propagate within the track of positive branches of a bi-leader carrying strong negative charges. The lightning flash is terminated when the electric field is reduced to the point where it cannot sustain the discharge's propagation anymore.

The electromagnetic spectrum of lightning

The rapid release of electric energy inside the lightning channel generates a shock wave and electromagnetic radiation in a broad spectrum, see the entry *Radiation, Electromagnetic*. The shock wave rapidly decays into an acoustic wave we know as thunder. The electromagnetic radiation ranges from radio frequencies through visible to X-rays and gamma rays, composing the basis for ground-based lightning location systems (LLS) and remote sensing from satellites.

Each lightning component (stepped leaders, return strokes, recoil streamers) emits electromagnetic energy proportional to the charge carried and its derivative in time. Negative stepped leaders are associated with strong negative currents in very short pulses (1 ms) and are detectable in very high frequencies (VHF, 1–200 MHz), as well as the dart leaders and recoil streamers, but with a relatively lower electrical current (MacGorman and Rust, 1998). The return strokes of a CG are high-energy discharges typically of the magnitude 10–100 kA in long pulses and radiate from the very low to high frequency range (1 kHz–10 MHz). Positive CG return strokes usually have continuous high current (>100 kA) and therefore are easily detected by VLF systems.

Radio emissions from lightning occur in the form of short pulses by accelerated charges during the fast-changing current steps, while the optical emissions occur from ionized and dissociated gases by thermal radiation of the lightning channel (Goodman et al., 1988). The heating in the channel reaches temperatures above 20,000 K resulting in optical emissions primarily in discrete atomic lines with some continuum at shorter wavelengths. Several measurements of lightning emission in the cloud top have shown strongest emissions at the neutral oxygen (OI(l)) and neutral nitrogen (NI(l)) lines, i.e., 777.4 and 868.3 nm in the near infrared, respectively (Goodman et al., 1988).

The radio electromagnetic waves of the lightning processes described above travel through the atmosphere and then are likely to be dissipated, reflected, scattered, refracted, and absorbed. The main effect is the dissipation, reducing the amplitude of the signal inversely proportional to the square of the distance. Ionospheric reflection, where the energy from waves with frequency lower than 5 MHz is trapped in the atmospheric waveguide formed by the ionosphere and the ground, permits long-range propagation of waves from high-energy return strokes. In the optical spectrum, the scattered energy by the cloud particles is observed from satellites as a diffuse light source at cloud top (Christian et al., 1989).

Ground-based lightning location systems

Several instruments can be used to locate lightning flashes, and more detail can be found at MacGorman and Rust, (1998) and Betz et al., (2009). The main technique consists of a network of sensors that detect IC and/or CG lightning by recording the electromagnetic radiation from VLF to VHF continuously with time. The radiation detected by each sensor is then compared to other sensors in the network using two main location methods: the time-of-arrival and interferometer techniques. In the time-of-arrival method (TOA), time difference of lightning waveforms from several stations is computed and the location of lightning occurrence is given by the intersection of the hyperbolas for equal time differences. The interferometer method consists of determining the directions of the lightning waveform (azimuth and elevation) by analyzing the phase difference of an incident wave at several stations, and the intersection of these directions gives the location of the lightning source.

Today's operational lightning detection networks usually consist of different sensor types that use one or more location method for redundancy. These networks can be local, regional, or global depending on their operation baseline (distance between the sensors), and their detection efficiency and location accuracy are determined by the density of sensors and radio frequency used (Betz et al., 2009). Table 1 summarizes some of these more widely used lightning networks. The largest regional network is the US National Lightning Detection Network (NLDN) created in 1998, composed by 114 sensors operating in LF that locates mainly CG lightning in North America. Similar regional networks are found in Australia, Brazil, Canada, and Europe. Long-range networks operate in VLF and have been deployed worldwide in an attempt to locate lightning over remote areas like the oceans and the tropics. These networks operate with a sensor baseline of thousands of kilometers, which limits the detection efficiency to the stronger amplitude lightning signals (Cramer and Cummins, 1999).

Total lightning (IC + CG lightning) is monitored using VHF and a combination of LF and VLF or VHF and LF. In the USA, total lightning is monitored by several VHF Lightning Mapping Array (LMA) research networks (Table 1) developed by New Mexico Tech (Rison et al., 1999). The individual LMA regional networks consist of 10 or more stations extending ~80 km. The LMA measures the TOA of the magnetic peak signals at the different receiving stations to locate the source of impulsive VHF radio signals. Hundreds to thousands of sources per flash can be correlated in space and time, allowing a 3-D or 2-D lightning mapping of the channel over a regional domain of ~200 km.

Lightning detection from space

Several astronauts reported seeing lightning while looking down from space in the 1960s, describing flashes with hundreds of kilometers in extent and simultaneous flashes occurring between widely separated storms. Lightning was detected in early satellite imagery (Sparrow and Ney, 1971), and in 1981, the space shuttle astronauts recorded lightning in a 16 mm movie camera (Goodman et al., 1993). Although it was not their primary objective, several instruments onboard of the US Air Force DMSP

Lightning, Table 1 Ground-based lightning location systems operating in the world

Network	Frequency used	Type of discharges detected	Coverage area	Website
NLDN (US National Lightning Detection Network)	LF	Mainly CG	United States of America	http://www.vaisala.com/
CLDN (Canadian Lightning Detection Network)	LF	Mainly CG	Canada	http://www.ec.gc.ca/foudre-lightning/default.asp?lang=En&n=D88E34E8-1
EUCLID (EUropean Cooperation for LIghtning Detection)	LF	Mainly CG	Europe	http://www.euclid.org
RINDAT (Rede Integrada Nacional de Detecção de Descargas Atmosféricas)	LF	Mainly CG	South-Southeast Brazil	http://www.rindat.com.br/
LINET (LIghtning location NETwork)	VLF, LF	Total lightning (IC + CG)	Europe	http://www.pa.op.dlr.de/linet/
LDAR (Lightning Detection and Ranging)	VHF	Total lightning (IC + CG)	Florida, USA	http://branch.nsstc.nasa.gov/PUBLIC/LDARII/
LMA (Lightning Mapping Array)	VHF	Total lightning (IC + CG)	USA-New Mexico, Oklahoma, Northern Alabama, Western Texas, Colorado, Atlanta, Washington DC, Spain	http://lightning.nmt.edu/nmt_lms/
ENTLN (Earth Networks Total Lightning Networks)	ELF-HF	Total lightning (IC + CG) Mainly CG	Australia, Americas, Europe Globe	http://www.earthnetworks.com/
STARNET (Sferics Timing and Ranging NETwork)	VLF	Mainly CG	South America and East Africa	http://www.zeus.iag.usp.br/
WWLLN (World Wide Lightning Location Network)	VLF	Mainly CG	Globe	http://wwlln.net/
Vaisala GLD360 (Global Lightning Dataset 360)	VLF	Mainly CG	Globe	http://www.vaisala.com/
GLN (Global Lightning Network)	VLF	Mainly CG	Globe	http://www.uspln.com/gln.html
ATDnet (Met Office's Arrival Time Difference network)	VLF	Mainly CG	Globe	http://www.metoffice.gov.uk/

(Defense Meteorological Satellite Program) satellites have also recorded lightning, providing the first global lightning distribution map as a bonus to the mission (Goodman et al., 1993).

The Optical Transient Detector (OTD) onboard of the Microlab-1 (later renamed as OrbView-1) satellite was the first instrument designed to measure lightning from space day and night with storm scale resolution. The OTD operated between 1995 and 2000 in a 70° inclination low Earth orbit (see Low Earth Orbit (LEO)) at an altitude of 740 km. From this altitude, the OTD observed an individual storm for about 3 min. The design concept was based on the earlier research on optical emissions of lightning at cloud top (Christian and Goodman, 1987; Goodman et al., 1988). The OTD detected optical impulses with a 128 × 128 charge-coupled device (CCD) using a 1 nm narrow-band interference filter centered at 777.4 nm (Christian et al., 2003). Whereas the earlier satellite-based studies were limited to detecting visible lightning flashes during the darkness of night, the near-infrared wavelength combined with the use of spatial and temporal filtering used by OTD also allowed lightning detection during daylight. In 1997, the Lightning Imaging Sensor (LIS) onboard the Tropical Rainfall Measuring Mission (TRMM) (Kummerow et al., 1998) was launched into a lower orbit inclination of 35° at an altitude of 350 km, later raised to 402 km in August 2001 to extend the mission lifetime. From this altitude, the LIS observed an individual storm for about 90 s.

The OTD was a flight qualified engineering model of the LIS, and thus, they share the same basic design heritage. In both OTD and LIS, the signal is read out from the focal plane into a real-time event processor for lightning event detection. The background scene is updated during each frame readout sequence and when a pixel's brightness compared to the prior background values exceeds a threshold, it is identified as a lightning *event*. The events are sent to the satellite ground station for geolocation processing in space and time, and an algorithm clusters the events into "flashes" (multiple CCD events grouped into time and space). The flash cannot be distinguished between CG and IC lightning, although in a statistical sense, the fraction of CG and IC flashes might be retrievable from a large sample of flashes (Koshak, 2010).

FORTE (Fast On-Orbit Recording of Transient Events) satellite was built by Los Alamos National Laboratory to study lightning signals from space (Jacobson et al., 2000,

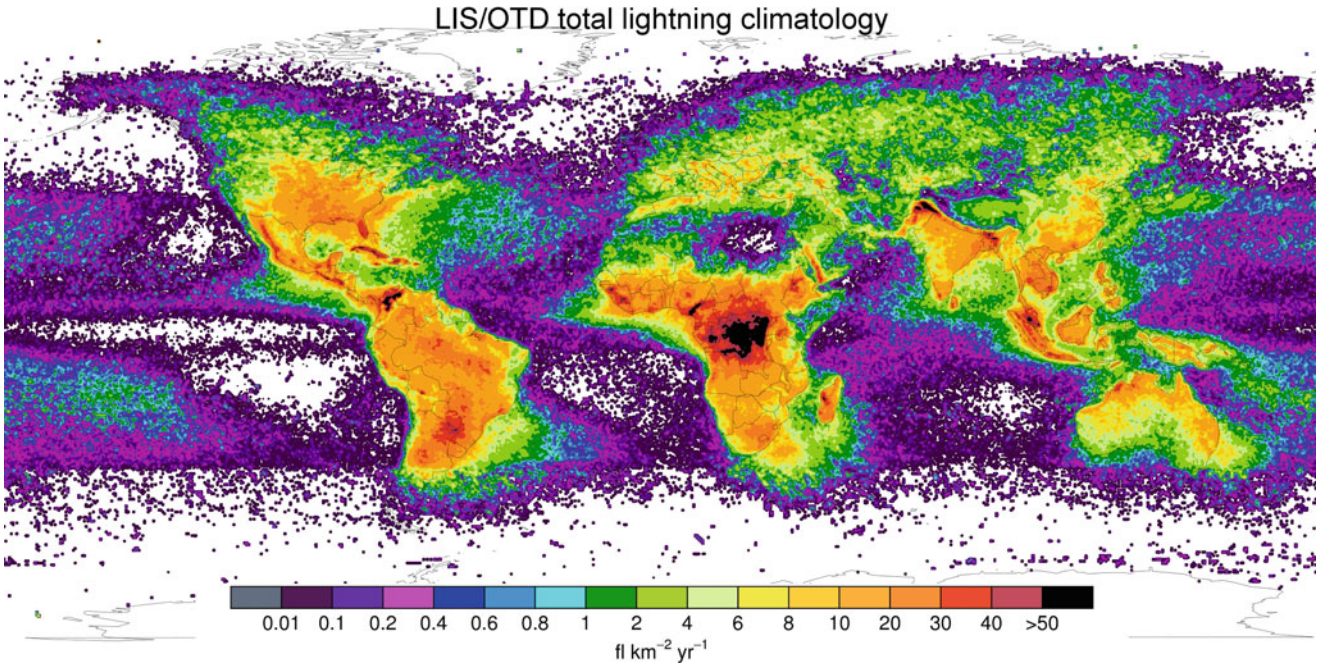

Lightning, Figure 1 Total lightning climatology derived from OTD (1995–2000) and LIS (1998–2010) at 0.5° resolution.

Suszcynsky et al., 2000; Hamlin et al., 2009). Launched in August 1997 at 800 km of altitude with a 70° of inclination and a circular orbit, the optical lightning location system has the same design of OTD and LIS but it also carries a broad band photo diode and the VHF receivers had two broad band channels which are selectable from a grid covering the entire high frequency and to very high frequency (Hamlin et al., 2009), allowing a combined optical and radio frequency observations of lightning. FORTE demonstrated that lightning can be located from space based on multiple-satellite VHF receivers. The "ORAGE" project has also been studying the possibility of locating lightning flashes using VHF-UHF interferometry from a constellation of microsatellites (Bondiou-Clergerie et al., 1999).

OTD and LIS findings

The first global distribution of total lightning was derived from 5 years of OTD measurements by Christian et al., (2003), who found that the annual average global flash rate is 44 fl s^{-1}, with a maximum of 55 fl s^{-1} in the boreal summer and a minimum of 35 fl s^{-1} in the boreal winter. Recently, Blakeslee et al. (2012) and Cecil et al. (2012) found that these values remained nearly the same combining OTD (1995–2000) and LIS observations (1998–2010). These authors also showed that all continents display a strong diurnal variation with lightning peaking in the late afternoon, while oceans exhibit a minimal nearly flat diurnal variation, but morning hours are typically slightly enhanced over afternoon. In Figure 1, we present the updated LIS/OTD climatology for 16 years of OTD (1995–2000) and LIS (1999–2010) combined observations of total lightning flash rate density (FRD, fl km^{-2} year^{-1}) from Marshall Space Flight Center gridded LIS-OTD climatology product (High Resolution Flash Climatology, HRFC_COM_FR - Cecil et al. 2012). The difference between land and ocean can be clearly observed, with lightning occurring more frequently over continental (> 20 fl km^{-2} year^{-1}) regions having greater instability and stronger vertical motion than oceanic environments. However, some coastal regions presented moderate FRD (1–10 fl km^{-2} year^{-1}) associated with frequent synoptic scale extratropical cyclones and cold fronts (such as south-southeast coasts of Brazil, South Africa, Australia, and United States), and large-scale convergence zones (such as the South Atlantic, South Pacific, and the Intertropical Convergence Zones).

High elevated and complex terrain regions over the tropics can be identified by high thunderstorm activity (> 30 fl km^{-2} year^{-1}) at the mountains foot (e.g., Andes, Himalayas, Sierra Madre Occidental, Cameroon Line, and Mitumba Mountains). Congo Basin is dramatically highlighted by its extensive area of large FRD (> 50 fl km^{-2} year^{-1}), where the greatest annual number of individual thunderstorms is observed (Zipser et al., 2006). However, higher resolution (0.10°) LIS climatological maps highlighting topographical features and complex

terrain indicate the Congo Basin has the second highest climatological FRD, with 232 fl km^{-2} $year^{-1}$ (at the foothills of Mitumba Mountains), while the total lightning "hot spot" on Earth is observed over Lake Maracaibo with 250 fl km^{-2} $year^{-1}$ (Albrecht et al., 2011). Lake Maracaibo thunderstorm activity is very localized, determined by nocturnal convergence of land-lake and mountain-valley breezes over a warm lake, building the perfect scenario for thunderstorm development of more than 300 days per year (Albrecht et al., 2011). Frequent lightning activity (30–50 fl km^{-2} $year^{-1}$) is also observed over Florida, Cuba, and Indonesia-Malaysia due to land-ocean sea breezes and over the borders of Argentina, Paraguay, and Brazil where the greatest individual flash rates per mesoscale convective systems are observed (Cecil et al., 2005; Zipser et al., 2006).

In addition to mapping the lightning distribution, the instrument suite on the TRMM satellite allows more detailed characterization of the thunderstorms producing lightning. The TRMM radar and radiometer (see Microwave Radiometers) also show more intense storms over land (Cecil et al., 2005; Zipser et al., 2006). But for a given radar or radiometer signature, a storm over land is likely to produce more lightning than an otherwise similar storm over ocean (Liu et al., 2011). This suggests differences in the mixed phase microphysics and precipitation, hinted at by lightning but not resolved by the radar or radiometer uniquely by themselves.

More information on LIS and OTD can be found at http://thunder.msfc.nasa.gov/.

The future of lightning mapping from space

The next generation of NOAA Geostationary Operational Environmental Satellite (GOES-R) series and the EUMETSAT Meteosat Third Generation (MTG) will detect, locate, and measure continuous total lightning activity over their full disk with a nominal resolution of 10 km. GOES-R will carry the Geostationary Lightning Mapper (GLM) and it is scheduled to be launched in late 2015, while the MTG will carry the Lightning Imager (LI) and it is scheduled to be launched in 2018. Both GLM and LI are heritages of OTD and LIS, but GOES-R and MTG are equipped with improved communications systems and much greater telemetry bandwidth to ensure a continuous and reliable flow of the remote sensing products. The GOES-R series will maintain the 2-satellite system over the western hemisphere, with the operational GOES-R satellites at 75 °W and 137 °W. The GLM and LI together will provide continuous full-disk total lightning for storm warning and nowcasting (e.g., early warnings of tornadic activity, hail, and floods – see *Severe Storms*) for half of the globe. A geostationary lightning imager (GLI) having more limited coverage of mainland China and adjacent ocean is also planned for the Chinese FY-4 next-generation geostationary satellite series. More information on GOES-R GLM and MTG-LI can be found at http://www.goes-r.gov/ and http://www.eumetsat.int/, respectively.

Bibliography

Albrecht, R. I., et al., 2011. The 13 years of TRMM lightning imaging sensor: from individual flash characteristics to decadal tendencies. In *Proceedings XIV International Conference on Atmospheric Electricity*. Rio de Janeiro, 08–12, Aug 2011.

Betz, H. D., Schumann, U., and Laroche, P., 2009. *Lightning: Principles, Instruments and Applications. Review of Modern Lightning Research*. Dordrecht: Springer, p. 641.

Blakeslee, R. J., Mach, D. M., Bateman, M. G., and Bailey, J. C., 2012. Seasonal variations in the lightning diurnal cycle and implications for the global electric circuit. Atmospheric Research, http://dx.doi.org/10.1016/j.atmosres.2012.09.023.

Bondiou-Clergerie, A., Blanchet, P., Théry, C., Delannoy, A., Lojou, J.Y., Soulage, A., Richard, P., Roux, F., and Chauzy, S., 1999. "ORAGES": a project for space-borne detection of lightning flashes using interferometry in the VHF-UHF band. In *Proceedings of the 11th International Conference on Atmospheric Electricity*, Guntersville, Alabama, pp. 184–187.

Cecil, D. J., Buechler, D. E., and Blakeslee, R. J., 2012. Gridded lightning climatology from TRMM-LIS and OTD: Dataset description. *Atmospheric Research*, doi: http://dx.doi.org/10.1016/j.atmosres.2012.06.028.

Cecil, D. J., Goodman, S. J., Boccippio, D. J., Zipser, E. J., and Nesbitt, S. W., 2005. Three years of TRMM precipitation features. Part I: radar, radiometric, and lightning characteristics. *Monthly Weather Review*, **133**(3), 543–566.

Christian, H. J., and Goodman, S. J., 1987. Optical observations of lightning from a high altitude airplane. *Journal of Atmospheric and Oceanic Technology*, **4**, 701–711.

Christian, H. J., Blakeslee, R. J., and Goodman, S. J., 1989. The detection of lightning from geostationary orbit. *Journal of Geophysical Research*, **94**, 13329–13337.

Christian, H. J., et al., 2003. Global frequency and distribution of lightning as observed from space by the optical transient detector. *Journal of Geophysical Research*, **108**, 4005, doi:10.1029/2002JD002347.

Cramer, J. A., and Cummins, K. L., 1999. Long-range and transoceanic lightning detection. In *Proceedings 11th International Conference on Atmospheric Electricity*. Guntersville, 7–11, June 1999, pp. 250–253.

Goodman, S. J., Christian, H. J., and Rust, W. D., 1988. Optical pulse characteristics of intracloud and cloud-to-ground lightning observed from above clouds. *Journal of Applied Meteorology*, **27**, 1369–1381.

Goodman, S. J., Christian, H. J., and Rust, W. D., 1993. Global observations of lightning. In Gurney, R. J., Foster, J. L., and Parkinson, C. L. (eds.), *Atlas of Satellite Observations Related to Global Change*. Cambridge, UK: Cambridge University Press, pp. 191–219.

Hamlin, T., Wiens, K. C., Jacobson, A. R., Light, T. E. L., and Eack, K. B., 2009. Space- and ground-based studies of lightning signatures. In *Lightning: Principles, Instruments and Applications. Review of Modern Lightning Research*. Dordrecht: Springer, pp. 287–2017.

Jacobson, A. R., Cummins, K. L., Carter, M., Klingner, P., Dupre, D. R., and Knox, S. O., 2000. FORTE radiofrequency observations of lightning strokes detected by the National Lightning Detection Network. Journal of Geophysical Research, 105, 15653–15662.

Koshak, W. J., 2010. Optical characteristics of OTD flashes and the implementations for flash-type discrimination. *Journal of Atmospheric and Oceanic Technology*, **27**, 1822–1838.

Kummerow, C., Barnes, W., Kozu, T., Shiue, J., and Simpson, J., 1998. The tropical rainfall measuring mission (TRMM) sensor package. *Journal of Atmospheric and Oceanic Technology*, **15**, 809–817.

Liu, C., Cecil, D., and Zipser, E. J., 2011. Relationships between lightning flash rates and passive microwave brightness temperatures at 85 and 37 GHz over the tropics and subtropics. *Journal of Geophysical Research*, **116**, D23108.
MacGorman, D. R., and Rust, W. D., 1998. *The Electrical Nature of Storms*. New York: Oxford University Press.
Rakov, V. A., and Uman, M. A., 2003. *Lightning: Physics and Effects*. Cambridge, UK: Cambridge University Press, p. 687.
Rison, W., Thomas, R. J., Krehbiel, P. R., Hamlin, T., and Harlin, J., 1999. A GPS-based three-dimensional lightning mapping system: initial observations in central New Mexico. *Geophysical Research Letters*, **26**, 3573–3576.
Sparrow, J. G., and Ney, E. P., 1971. Lightning observations by satellite. *Nature*, **232**, 540–541.
Suszcynsky, D. M., Kirkland, M. W., Jacobson, A. R., Franz, R. C., Knox, S. O., Guillen, J. L. L., and Green, J. L., 2000. FORTE observations of simultaneous VHF and optical emissions from lightning: Basic phenomenology. Journal of Geophysical Research, 10(D2), 2191–2201.
Uman, M. A., 1987. *The Lightning Discharge*. New York: Elsevier, p. 228.
World Meteorological Organization (WMO), 2011. METOTERM http://www.wmo.int/pages/prog/lsp/meteoterm_wmo_en.html. Visited on 16, Oct 2011.
Zipser, E., Cecil, D., Liu, C., Nesbitt, S. W., and Yorty, S., 2006. Where are the most intense thunderstorms on Earth? *Bulletin of the American Meteorological Society*, **87**, 1057–1071.

Cross-references

Microwave Radiometers
Optical/Infrared, Radiative Transfer
Radiation, Electromagnetic
Severe Storms

LIMB SOUNDING, ATMOSPHERIC

Nathaniel Livesey
Jet Propulsion Laboratory, California Institute of Technology, Pasadena, CA, USA

Synonyms

Limb profiling; Occultation measurements

Definition

Limb. The portion of a planetary (or stellar) atmosphere at the outer boundary of the disk, viewed "edge on."
Limb sounding. Atmospheric remote sounding technique involving observing radiation emitted or scattered from the limb.
Occultation. Atmospheric remote sounding technique involving observing radiation emitted (or reflected) by a distant body (solar, stellar, lunar, or an orbiting satellite), transmitted along a limb path through an absorbing and/or scattering planetary atmosphere, and detected by a remote observer.

Introduction

Limb sounding is a widely used atmospheric remote sounding technique, whereby the atmosphere is viewed "edge on" by a space- or airborne instrument. Limb sounding observations are made from the microwave and infrared – where thermal emission is observed – to the visible and ultraviolet, where observations are typically of sunlight scattered in the limb or of airglow. A wide range of spaceborne limb sounding instruments have been used to observe atmospheric temperature, composition, and dynamics from the upper troposphere (~10 km altitude) to the mid-thermosphere (~450 km). A closely related technique, known as "occultation," involves observing the atmospheric absorption and/or scattering of radiation emitted by a remote source (solar, lunar, stellar, or, more recently a GPS satellite).

Limb sounding has significant advantages over nadir sounding (i.e., viewing straight down) or near-nadir sounding. Firstly, scanning the instrument field of view vertically across the atmospheric limb can give atmospheric profile information with greater vertical resolution than is typically possible from nadir sounders. In addition, complexities associated with emission or reflection of radiation by the planetary surface can be avoided. Finally, by viewing a significantly longer atmospheric path than nadir sounders, limb viewing instruments can achieve a stronger signal to noise for observations of tenuous atmospheric trace gases. However, this same long path length (typically a few 100 km) results in a poorer horizontal resolution than is possible with nadir sounding instruments.

With the exception of the infrared Mars Climate Sounder instrument (MCS, McCleese et al., 2007) on the Mars Climate Orbiter, limb sounding observations have been confined to those of Earth's atmosphere and are the focus of the discussion in this entry.

Principles and techniques

Limb radiances and line broadening

Each limb view is associated with a particular "tangent height" – the closest distance from the limb ray to the Earth's surface. High tangent height views typically give small signals, due to the tenuous atmosphere at these altitudes. As tangent altitudes decrease, atmospheric emission or scattering strengthens, increasing the observed signals. Eventually, the atmosphere becomes sufficiently opaque that signals from lower regions in the atmosphere are absorbed by the layers above and not seen by the instrument. At this point, radiances tend to remain fairly constant with decreasing tangent altitude (or to change only slightly, due to second-order geometrical effects) and are said to be "saturated" or "blacked out," as the signal continues to derive largely from the lowermost nonopaque layers. Refraction is significant for limb rays in the lower atmosphere but is generally negligible above ~20 km.

Molecular spectral lines are broadened in the atmosphere by a combination of the ensemble of Doppler shifts from the thermal motion of the molecules ("Doppler" broadening) and by collisions with other molecules ("collision" or "pressure" broadening). The latter generally dominates line widths of infrared and microwave signals up to ~60 km, while for visible and ultraviolet wavelengths, Doppler broadening dominates throughout the bulk of the atmosphere. Pressure broadening of spectral lines can provide valuable information on the vertical distribution of trace gases (in addition to the information gained by vertically scanning the instrument field of view) with frequencies further from line centers conveying information on lower regions of the atmosphere, where lines are broad enough to contribute to the observed signals. For wavelengths where pressure broadening is insignificant, vertical distribution information can still be obtained by observing in multiple spectral regions having different atmospheric absorptions (and thus penetration depths).

Solar occultation and related observations

Observation of the atmospheric absorption of solar radiation ("direct sun" measurements) has a long heritage in atmospheric science (e.g., the observations of ozone pioneered in the 1920s by Dobson). Solar occultation is a natural extension of these ground-based techniques (and similar observations from balloon and aircraft vantage points). An instrument on a low Earth-orbiting spacecraft can perform an occultation observation during sunrise and sunset on each of ~14 orbits per 24 h period. Typically, occultation instruments observe a narrow portion of the solar disk and track this as it rises or sets through the atmosphere. The strong solar signal provides excellent signal to noise and obviates the need to cool the instrument or its detectors. The observations of the sun above the atmosphere, before sunset or after sunrise, can be used to ensure a stable instrument calibration.

A succession of solar occultation instruments have provided a long record of atmospheric composition observations including the Stratospheric Aerosol and Gas Experiment (SAGE) I, II, and III series of instruments (McCormick et al., 1989), the Polar Ozone and Aerosol Measurement (POAM) instruments (Lucke et al., 1999), and the Halogen Occultation Experiment (HALOE) on the Upper Atmosphere Research Satellite (UARS) (Russell et al., 1993). Occultation observations were also made by the Atmospheric Trace Molecule Spectroscopy (ATMOS) instrument flown on the Space Shuttle ATLAS program (Gunson et al., 1996), and the Improved Limb Atmospheric Spectrometer instruments (ILAS I and II) on the Japanese Advanced Earth Observing Satellites (ADEOS I and II). The Scanning Imaging Absorption Spectrometer for Atmospheric CHartograpy instrument (SCIAMACHY, Bovensman et al., 1999) on the European Envisat performs solar occultation measurements in addition to limb and nadir imaging. Most recently, the Atmospheric Chemistry Experiment's Fourier Transform Spectrometer and Measurement of Aerosol Extinction in the Stratosphere and Troposphere Retrieved by Occultation (ACE/FTS and ACE/MAESTRO) instruments have been continuing and augmenting this record (Bernath et al., 2005). Currently, ACE is the only operating mission employing solar occultation, though other concepts are in formulation including plans to fly a SAGE III instrument on the International Space Station.

While offering good vertical resolution and outstanding signal to noise and calibration stability, solar occultation instruments are fundamentally limited by orbital geometry to making only ~30 observations per 24 h period. While some instruments augment this coverage with observations of lunar or stellar occultations, these, by definition, have poorer signal to noise than the solar occultation observations.

As described below, limb sounding observations of atmospheric emission or of scattered solar radiation offer comparable vertical resolution to occultation but have the advantage that observations can be made on a near-global basis daily.

Radio occultation

Observations of the atmospheric occultation of signals broadcast by GPS are a more recent development. In this technique, observations of refractive phase shift, as opposed to atmospheric absorption in different spectral regions, form the basis for the measurement. GPS occultation yields information on atmospheric refraction, and in turn temperature and/or water vapor profiles. More information on this technique is given elsewhere in this volume.

Microwave limb sounding

Atmospheric microwave emissions are generally associated with molecular rotational transitions, theoretically enabling observation of any atmospheric species with a significant dipole moment. Microwave limb sounding instruments have made observations of a wealth of species in the frequency range from ~60 GHz (5 mm wavelength) to ~2.5 THz (120 μm). Microwave signals are unaffected by aerosols and all but the thickest clouds, as the wavelengths used are longer than the typical particle sizes. This enables microwave observations of atmospheric composition in a limb sounding geometry in regions that are too cloudy for observations at other wavelengths.

To date, five spaceborne instruments employing limb sounding at microwave frequencies have flown: The Microwave Atmospheric Sounder (MAS) as part of the ATLAS payload on the Space Shuttle (Croskey et al., 1992), the Microwave Limb Sounder (MLS) instruments on the NASA UARS and Aura satellites (Barath et al., 1993; Waters et al., 2006), the Submillimeter Radiometer (SMR) on the Swedish Odin satellite (Murtagh et al., 2002), and, most recently, the Submillimeter-Wave Limb

Emission Sounder (SMILES) on the International Space Station (Ozeki et al., 2001).

Microwave instruments can achieve arbitrarily fine frequency resolutions, enabling individual transition lines to be resolved in great detail. The observations of line shape enable simultaneous observation of both atmospheric pressure (largely affecting the width of a given transition line in the pressure-broadening regime) and species abundance (largely affecting the line strength). By combining inferred atmospheric pressure information with limb tangent altitude information, and assuming hydrostatic balance, atmospheric temperature profile information can be obtained.

The field-of-view width for a microwave instrument is determined by the antenna size and wavelength employed, with narrower fields of view achieved for larger antennae and/or shorter wavelengths and somewhat large antennae dictated for many observations. For example, the Aura MLS instrument's 1.6 m antenna has a field of view that is ~3.5 km wide at the limb (full width, half maximum) at 200 GHz from a 700 km orbit. The lower vertical range of microwave limb sounding instruments is limited by continuum absorption from oxygen, nitrogen, and water vapor, with ~8 km altitude typically being the deepest penetration.

Infrared limb sounding

As with microwave limb sounding, infrared instruments observe thermal emission from the atmosphere, in this case mostly arising from molecular vibrational transitions. Again, collisional broadening enables determination of atmospheric pressure at the tangent point. Although not all infrared limb sounding instruments have the spectral resolution to resolve individual line shapes, pressure information can generally still be obtained from broader-band measurements.

Scattering and emission from clouds pose a more significant limitation to infrared limb sounders than microwave instruments, particularly in the tropics where clouds are prevalent in the upper troposphere. In clear-sky regions, infrared limb sounders can typically penetrate a few kilometers deeper than microwave sounders, but continuum absorption is, again, the ultimate limitation to this penetration. Infrared instruments can more easily achieve narrower fields of view than those in the microwave, and this can translate into a finer vertical resolution for the geophysical observations. However, the detectors typically need to be cooled (e.g., to ~70 K) in order to achieve a scientifically useful signal to noise.

Infrared limb sounding instruments have a long history in atmospheric science, starting with the Limb Radiance Inversion Radiometer (LRIR) on Nimbus 6, followed by the Limb Infrared Monitor of the Stratosphere (LIMS, Gille and Russell, 1984) and Stratospheric and Mesospheric Sounder (SAMS, Drummond et al., 1980) instruments on Nimbus 7. UARS included two infrared limb sounding instruments – the Cryogenic Limb Array Etalon Spectrometer (CLAES, Roche et al., 1993) and the Improved Stratospheric and Mesospheric Sounder (ISAMS, Taylor et al., 1993). More recent infrared limb sounders include the Michelson Interferometer for Passive Atmospheric Sounding instrument (MIPAS, Fischer et al., 2008) on ESA's Envisat spacecraft and the High-Resolution Dynamics Limb Sounder (HIRDLS, Gille et al., 2008) on NASA's Aura satellite.

The Sounding of the Atmosphere using Broadband Emission Radiometry (SABER) instrument on the Thermosphere, Ionosphere, Mesosphere Energetics and Dynamics (TIMED) mission (Russell et al., 1999) is another recently launched infrared limb sounder mainly focusing on the chemistry and structure of the upper atmosphere.

Visible and ultraviolet limb sounding

Limb viewing instruments at visible and ultraviolet wavelengths generally observe sunlight scattered by the atmospheric limb. These include the Optical Spectrograph and Infrared Imaging System (OSIRIS, Llewellyn et al., 2003) instrument on Odin and the planned limb sensor for the Ozone Mapping and Profiling Suite (OMPS) on the NPOESS (National Polar-orbiting Operational Environmental Satellite System) Preparatory Project (NPP). The SCIAMACY instrument on Envisat also includes a limb scattering capability. As collisional broadening does not significantly affect the (mainly electronic or vibronic) molecular transitions at these wavelengths, tangent pressure cannot be deduced from the observations, and the height registration of the resulting geophysical products is more critically reliant on independent knowledge of spacecraft pointing than is the case for longer wavelength observations.

In addition to limb scattering sounders, past instruments have observed visible atmospheric airglow emissions in the upper atmosphere. These include the Wind Imaging Interferometer (WINDII, Shepherd et al., 1993) and the High-Resolution Doppler Imager (HRDI, Hays et al., 1993) instruments, both on UARS, which used these observations to deduce upper atmospheric dynamics.

Inversion approaches for limb sounding instruments

Although scanning the field of view of an instrument up and down the atmospheric limb enables high-resolution observations of vertical profiles, the observed signals are (as with nadir sounding) affected by emission, absorption, and scattering throughout the ray path. Disentangling the impact of each atmospheric layer on the observed signal and deducing vertical profiles of temperature and composition is a nontrivial task, commonly known as a "retrieval" or "inverse" calculation.

A variety of techniques have been employed for limb sounding retrievals. The so-called onion peeling approach uses observations at the top of the limb scan to characterize the uppermost atmospheric region. This is then

accounted for when characterizing the next layer down, using lower-altitude limb views, and so on. A drawback of this technique is that the resulting profile depends strongly on the knowledge of the uppermost regions, where signal to noise is typically poor.

The most commonly adopted approach for limb sounding retrievals is the well-established "optimal estimation" method (Rodgers, 2000), which seeks the atmospheric state that matches all the observed signals simultaneously (taking into account potential noise on each signal). Although more computationally intensive than simpler approaches, this need not be a barrier with modern computing capabilities. Indeed, the most computationally demanding part of the calculation is typically the "forward model" (the computation that estimates the signal that would be observed by the instrument for a given atmospheric state), which is a central part of all but the simplest retrieval approaches, and upon which the accuracy of the resulting geophysical profiles ultimately depends.

Inhomogeneity along the limb line of sight can introduce biases in limb sounding retrievals, particularly in regions of strong atmospheric gradients. Some retrieval methods employ an iterative approach, whereby horizontal gradient information from a first pass is considered in a later retrieval step. In cases where the instrument line of sight is aligned with the spacecraft velocity vector, successive limb scans take multiple views through the same region of atmosphere, enabling a "tomographic" approach to the retrieval calculation to be taken (e.g., Livesey and Read (2000)).

Notable findings from limb sounding observations

The near-global daily coverage and good vertical resolution of limb sounding instruments has provided a wealth of information on atmospheric structure and composition from the upper troposphere through to the thermosphere. The early observations from LIMS and SAMS set the stage, with zonal-mean information on the abundance of key stratospheric and mesospheric trace gases. The three atmospheric composition limb sounders (CLAES, ISAMS, and MLS) on UARS, along with the HALOE solar occultation instrument, provided valuable insights into the dynamics and chemistry of Earth's stratosphere, most notably processes associated with chemical stratospheric ozone loss and the transport of air into and throughout the stratosphere. UARS observations also provided valuable information on the impact of volcanic gases and the resulting aerosols on the stratosphere, following the dramatic June 1991 eruption of Mt. Pinatubo in the Philippines (4 months before the UARS launch).

In addition to stratospheric and mesospheric composition observations, UARS MLS provided unprecedented information on water vapor and ice clouds in the upper troposphere. The Aura MLS and HIRDLS instruments have enhanced this record providing the first daily global observations of upper tropospheric ozone, carbon monoxide (MLS only), and nitric acid. The upper troposphere is an important region of the atmosphere for climate, as it is where water vapor (the strongest greenhouse gas) and ozone have their largest radiative impact.

Outlook

At the time of writing, the only limb sounding instruments in operation are Aura MLS, Odin SMR and OSIRS, and Envisat MIPAS. The SMILES instrument experienced a critical failure after ~6 months of operation, although plans are in formulation for a possible fix. While several new limb sounding instrument concepts are under formulation, to date none have been confirmed for launch. The most mature is the ESA Process Exploration through Measurements of Infrared and millimeter-wave Emitted Radiation (PREMIER) mission, which includes infrared and microwave limb sounding instruments observing the upper troposphere and lower stratosphere.

Conclusion

Limb sounding instruments provide a wealth of information on the composition, structure, and dynamics of Earth's atmosphere, through observations of emitted or scattered radiation in an "edge on" viewing geometry. Limb sounding offers a valuable combination of good vertical resolution and near-global daily coverage, using wavelengths ranging from the microwave to the ultraviolet, and can provide observations from the upper troposphere to the middle thermosphere. Limb sounding observations have led to important discoveries concerning key dynamical and chemical processes in Earth's stratosphere (including those processes associated with the "ozone hole"), and in the upper troposphere where water vapor and ozone have their strongest greenhouse forcing.

Acknowledgment

This research was carried out at the Jet Propulsion Laboratory, California Institute of Technology, under a contract with the NASA.

Bibliography

Barath, F. T., et al., 1993. The upper atmosphere research satellite microwave limb sounder experiment. *Journal of Geophysical Research*, **98**, 10, 751–10, 762.

Bernath, P. D., et al., 2005. Atmospheric chemistry experiment (ACE): mission overview. *Geophysical Research Letters*, **32**, L15S01, doi:10.1029/2005GL022386.

Bovensman, H., Burrows, J. P., Buckwitz, B., Frerick, J., Noël, S., Rozanov, V. V., Chance, K. V., and Goede, A. P. H., 1999. SCIAMACHY: mission objectives and measurement modes. *Journal of Atmospheric Science*, **56**, 127–150.

Croskey, C. L., et al., 1992. The millimeter wave atmospheric sounder (MAS): a shuttle-based remote sensing experiment. *IEEE Transactions on Microwave Theory and Techniques*, **40**(6), 1090.

Drummond, J. R., Houghton, J. T., Peskett, G. D., Rodgers, C. D., Wale, M. J., Whitney, J. G., and Williamson, E. J., 1980. The stratospheric and mesospheric sounder on nimbus 7.

Philosophical Transactions of the Royal Society of London, **296**(1418), 219–241.
Fischer, H., et al., 2008. MIPAS: an instrument for atmospheric and climate research. *Atmospheric Chemistry and Physics*, **8**, 2151–2188.
Gille, J. C., and Russell, J. M., III, 1984. The limb infrared monitor of the stratosphere: experiment description, performance and results. *Journal of Geophysical Research*, **89**, 5125–5140.
Gille, J., et al., 2008. High resolution dynamics limb sounder (HIRDLS): experiment overview, recovery and validation of initial temperature data. *Journal of Geophysical Research*, **113**, D16S43, doi:10.1029/2007JD008824.
Gunson, M. R., et al., 1996. The atmospheric trace molecule spectroscopy (ATMOS) experiment: deployment on the ATLAS space shuttle missions. *Geophysical Research Letters*, **23**, 2333–2336.
Hays, P. B., Abreu, V. J., Dobbs, M. E., Gell, D. A., Grassi, H. J., and Skinner, W. R., 1993. The high-resolution doppler imager on the upper atmosphere research satellite. *Journal of Geophysical Research*, **98**, 10, 713–10, 723.
Livesey, N. J., and Read, W. G., 2000. Direct retrieval of line-of-sight atmospheric structure from limb sounding observations. *Geophysical Research Letters*, **27**, 891–894.
Llewellyn, E. J., et al., 2003. First results from the OSIRIS instrument on-board Odin. *Sodankyla Geophysical Observatory Publications*, **92**, 1–47.
Lucke, R. L., et al., 1999. The polar ozone and aerosol measurement (POAM) III instrument and early validation report. *Journal of Geophysical Research*, **104**, 18785–18799.
McCleese, D. J., et al., 2007. Mars climate sounder: an investigation of the thermal and water vapor structure, dust and condensate distributions in the atmosphere, and energy balance of the polar regions. *Journal of Geophysical Research*, **112**, E05S06, doi:10.1029/1006JE002790.
McCormick, M. P., Zawodny, J. M., Velga, R. E., Larsen, J. C., and Wang, P. H., 1989. An overview of SAGE I and II ozone measurements. *Planetary and Space Science*, **37**, 1567–1586.
Murtagh, D., et al., 2002. An overview of the Odin atmospheric mission. *Canadian Journal of Physics*, **80**, 309–319.
Ozeki, H., et al., 2001. Development of superconducting submillimeter-wave limb emission sounder (JEM/SMILES) aboard the International Space Station. In Society of Photo-Optical Instrumentation Engineers (SPIE) Conference Series. Bellingham: SPIE, Vol. 4540, pp. 209–220.
Roche, A. E., Kumer, J. B., Mergenthaler, J. L., Ely, H. A., Uplinger, W. H., Potter, J. F., James, T. C., and Sterritt, L. W., 1993. The cryogenic limb array etalon spectrometer (CLAES) on UARS: experiment description and performance. *Journal of Geophysical Research*, **98**, 10, 763–10, 775.
Rodgers, C. D., 2000. *Inverse Methods for Atmospheric Science, Theory and Practice*. Singapore: World Scientific.
Russell, J. M., III, et al., 1993. The halogen occultation experiment. *Journal of Geophysical Research*, **93**, 10, 777–10, 798.
Russell, J. M., III, Mlynczak, M. G., Gordley, L. L., Tansock, J., and Esplin, R. 1999. An overview of the SABER experiment and preliminary calibration results. Proc. SPIE, 3756, doi:10.1117/12.366382, 277–288.
Shepherd, G. G., et al., 1993. WINDII, the wind imaging interferometer on the upper atmosphere research satellite. *Journal of Geophysical Research*, **98**, 10, 725–10, 750.
Taylor, F. W., et al., 1993. Remote sensing of atmospheric structure and composition by pressure modulation radiometry from space: the ISAMS experiment on UARS. *Journal of Geophysical Research*, **98**, 10, 799–10, 814.
Waters, J. W., et al., 2006. The earth observing system microwave limb sounder (EOS MLS) on the Aura satellite. *IEEE Transactions on Geoscience and Remote Sensing*, **44**, 1075–1092.

Cross-references

GPS, Occultation Systems
Stratospheric Ozone
Trace Gases, Stratosphere, and Mesosphere